

Stress and magnetic properties of epitaxial ferromagnetic layers and ferromagnetic- transition metal oxide bilayers

Dissertation

zur Erlangung des akademischen Grades
doctor rerum naturalium (Dr. rer. nat.)

vorgelegt von Naturwissenschaftlichen Fakultät II der
Martin-Luther-Universität Halle-Wittenberg

ANITA DHAKA

geboren am 01. Jan 1985 in Balwantpura (Indien)



angefertigt am:

Max-Planck-Institut für Mikrostrukturphysik Halle

Gutachter:

1. Prof. Dr. Jürgen Kirschner
2. Prof. Dr. Wolf Widdra
3. Dr. Andreas Berger

Verteidigt am: 7th June 2012

Abstract

The thesis presents combined stress and structural studies of epitaxially grown NiO and CoO layers on Ag(001). Our stress results during formation of NiO on Ag(001) at 300 K indicate an unexpectedly tensile stress for initial 1.5 monolayers (ML), where a (2×1) structure is observed by LEED. Continued deposition leads to a coherent layer-by-layer growth of NiO up to 5 ML. Here, the measured average stress is -5.8 GPa, it quantitatively ascribed to the misfit. Above 5 ML, misfit dislocations appear and stress is relaxed. In case of CoO on Ag(001), the initial 1.5 ML grows almost stress free, the continuous deposition leads to a compressive stress. However, the measured average stress of -2.6 GPa at 4 ML is significantly smaller than the expected lattice misfit stress of -9.8 GPa. The LEED measurements show a (1×1) structure in the whole investigated thickness of up to 10 ML CoO. The effect of the NiO and CoO layers on the coercivity of Fe film deposited on top is studied by *in-situ* MOKE. The coercivity of Fe film is enlarged due to the exchange interaction at the FM-AFM interface, it is found to depend on temperature, and on the thickness of the AFM (NiO and CoO) films. In addition, magnetoelastic stress measurements indicate that the magnetoelastic coupling coefficient B_2 of Fe on NiO is -19.6 MJ/m³, which differs in both magnitude and sign from the bulk value $+7.83$ MJ/m³. The measured B_2 of the same thickness of the Fe film on Ag(001) is $+2$ MJ/m³, which is a factor of 4 smaller from the bulk value. The induced strain in the Fe film on both substrates is comparable. This suggests that the FM-AFM interface plays an important role for the enlarged magnetoelastic coupling of Fe on NiO.

Cantilever stress measurements during deposition of Co on Pt(111) at 300 K indicate that Co induces a tensile stress of $+3.5$ GPa in the thickness range between 2 to 7 ML. Here, LEED indicates a coincidence lattice with a misfit of $+0.8\%$. The measured film stress is quantitatively ascribed to the misfit. The initial growth of Co on Pt(111) at 300 K does not reveal a significant tensile stress change, and at 370 K a compressive stress is observed. We ascribe this to intermixing at the Co-Pt interface. MOKE measurements show that the easy axis of magnetization changes from out-of-plane to in-plane at around 3.5 ML. A Pt cap layer on 5 ML Co/Pt(111) induces a spin reorientation transition (SRT) back to out-of-plane of the film. Co growth at 370 K leads to a shift of the SRT to a larger thickness of 5 ML. Our results suggest that an intermixed Co-Pt interface favors an out-of-plane, whereas a Co-vacuum interface favors an in-plane easy magnetization direction.

Stress during deposition of Ag on Pt(111) at 300 K and at higher temperatures, reveal a compressive stress of -8.9 GPa, which is close to the calculated misfit stress of -7.13 GPa. The average stress of the film decreases with the deposition above 580 K. Satellite spots are visible in LEED pattern at 630 K which ascribed to relaxation of the average stress.

Zusammenfassung

Die Arbeit stellt kombinierte Spannungs- und Strukturuntersuchungen von epitaktischen NiO und CoO-Schichten auf Ag(001) vor. Unsere Ergebnisse zeigen, dass bei der Bildung von NiO auf Ag(001) bei 300 K unerwartete Zugspannungen für die erste 1,5 Monolagen (ML) auftreten, wobei eine (2×1) -Struktur mit LEED beobachtet wird. Weiteres NiO Wachstum führt zu Lages Wachstum bis zu 5 ML entspricht. Die gemessenen mittlere Spannung von -5.8 GPa quantitativ der Gitterfehlpassungspannung. Oberhalb von 5 ML treten Versetzungen auf, und die Verspannungen werden abgebaut. Im Falle von CoO auf Ag(001) wachsen die ersten 1.5 ML nahezu spannungsfrei. Fortgesetztes Wachstum führt zu Druckspannungen. Allerdings sind die gemessenen mittleren Filmspannungen von -2.6 GPa bei 4 ML deutlich geringer als die aufgrund von Gitterfehlanpassung erwarteten Spannungen von -9.8 GPa. LEED-Messungen zeigen eine (1×1) -Struktur im gesamten untersuchten Dickenbereich bis hin zu 10 ML CoO. Der Einfluß der NiO und CoO-Schichten auf die Koerzitivfeldstärke des darüber abgeschiedenen Fe-Films wurde mit *in-situ* MOKE Messungen untersucht. Die Koerzitivität des Fe-Films ist aufgrund der Austausch-Wechselwirkung an der FM-AFM-Grenzschicht erhöht. Die Erholung der Koerzitivität hängt von der Temperatur als auch von der Dicke des AFM Films ab. Magnetoelastische Spannungsmessungen, zeigen, dass der magnetoelastische Kopplungskoeffizient B_2 von Fe auf NiO -19.6 MJ/m³ beträgt, was sich sowohl in der Größenordnung als auch im Vorzeichen vom Volumen Fe Wert von $+7.83$ MJ/m³ unterscheidet. B_2 eines gleichdicken Fe-Films auf Ag(001) beträgt $+2$ MJ/m³. Die induzierten Spannungen innerhalb der Fe-Filme sind auf beiden Substraten vergleichbar. Dies deutet darauf hin, dass die FM-AFM-Grenzfläche eine wichtige Rolle für Betrag und Vorzeichen der magnetoelastischen Kopplung spielt.

Spannungsmessungen während des Wachstums von Co auf Pt(111) bei 300 K zeigen, dass Co-induzierte Zugspannungen von 3.5 GPa in einem Dickenbereich zwischen 2 bis 7 ML auftreten. Hier zeigen die LEED-Untersuchungen das Auftreten eines Koinzidenzgitters mit einer Fehlpassung von 0.8%. Die gemessenen Filmspannungen können quantitativ auf die Gitterfehlpassung zurückgeführt werden. Zu Beginn des Co-Wachstum auf Pt(111) bei 300 K sind keine Zugspannungsänderungen zu erkennen, wobei bei 370 K sogar Druckverspannungen beobachtet werden. Wir schreiben dieses Verhalten der Durchmischung an der Co-Pt-Grenzschicht zu. MOKE Messungen zeigen, dass die leichte Achse der Magnetisierung bei 3.5 ML von einer ursprünglich senkrechten Ausrichtung zur Filmebene in die Filmebene hinein klappt. Eine Pt-Deckschicht auf 5 ML Co/Pt(111) induziert einen Spin-Reorientierungs-Übergang (SRT) zurück zur senkrechten Ausrichtung bezüglich der Filmebene. Co-Wachstum bei 370 K führt zu einer Verschiebung des SRT zu einer höheren Schichtdicke von 5 ML. Unsere Ergebnisse legen nahe, dass eine durchmischte Co-Pt-Grenzfläche eine senkrechte Magnetisierung zur Filmebene und eine Co-Vakuum-Grenzfläche eine Magnetisierungsrichtung innerhalb der Filmebene bevorzugt.

Verspannungen während des Wachstums von Ag auf Pt(111) bei 300 K und bei höheren Temperaturen zeigen eine Druckspannung von -8.9 GPa, die nahe an der berechneten Fehlpassungsspannung von -7.13 GPa liegt. Die gemittelten Spannungen im Ag-Film nehmen beim Wachstum oberhalb von 580 K ab. Satelliten-Spots sind im LEED-Bild bei 630 K sichtbar, und sie deuten auf eine Verringerung der mittleren Spannung hin.

Contents

1	Introduction	3
2	Fundamental concepts	7
2.1	Surface stress	7
2.2	Stress and strain in epitaxial growth	8
2.3	Magneto-elastic coupling in thin films	10
2.4	The magnetic coupling between a ferromagnetic and an antiferromagnetic film	12
3	Experimental setup	15
3.1	Ultrahigh vacuum chamber	15
3.2	Optical beam deflection setup	20
3.3	Magneto-optical Kerr effect setup	23
3.4	In-situ sample preparation	25
4	Results	27
4.1	Stress and structure of metallic oxide monolayers on Ag(001)	27
4.1.1	Preparation of NiO and CoO on Ag(001)	27
4.1.2	Stress and structure of NiO on Ag(001)	28
4.1.3	Stress and structure of CoO on Ag(001)	33
4.2	Stress and magnetic properties of Fe monolayers on NiO and CoO on Ag(001)	35
4.2.1	Stress and structure of Fe monolayers on NiO	36
4.2.2	Magnetism and magnetoelastic coupling of Fe monolayers	36
4.3	Stress and magnetism of metallic monolayers on Pt(111)	44
4.3.1	Stress and structure of Co and Ag monolayers on Pt(111)	44
4.3.2	Magnetism and spin reorientation transition in Co monolayers on Pt(111)	49
5	Discussion	51
5.1	The correlation between stress, strain and structure of NiO and CoO on Ag(001)	51
5.2	Effect of NiO on the coercivity and magnetoelastic coupling of Fe monolayers	58
5.3	Correlation between stress, strain and structure of Co and Ag/Pt(111)	70
5.4	Spin reorientation transition (SRT) of Co monolayers on Pt(111)	73
6	Conclusions and outlook	77

Contents	1
Bibliography	81
Acknowledgement	91
Erklärung-declaration	92
CV	93

Chapter 1

Introduction

The magnetic properties of ferromagnetic (FM) thin films (like Fe, Co and Ni) receive significant attention since they cannot be predicted from the respective properties of bulk materials. In thin films, the deviation of properties from bulk is often ascribed to the reduced coordination at the surface and interface, hybridization with adjacent layers, surface morphology, and growth behavior. Apart from these, in heteroepitaxial growth the film will often adapt its in-plane lattice parameter to the substrate and exhibits compressive or tensile strain, and simultaneously an out-of-plane expansion or contraction of the layer spacing results. The film might show an atomic structure which may not exist in the bulk. For example, Fe [1], Co [2], and Ni [3, 4] grow epitaxially on Cu(001) with a tetragonally distorted fcc structure. This anisotropic structural distortion does play an important role in magnetic anisotropy of ferromagnetic films. These thin films are particularly interesting because of their technological applications in data storage [5], sensor applications and in fundamental research of magnetism [6].

A ferromagnetic film in contact with an antiferromagnetic layer gives rise to new phenomena like a shift of the hysteresis loop (exchange bias) [7] and an enhanced coercivity [8]. The antiferromagnetic layers often pin the magnetization of the ferromagnetic layers across the interface [9]. Although this aspect is very important in applications, the physical origin of the coupling between the ferromagnet and the antiferromagnet at the interface is not yet fully understood. Most of the studies were done on polycrystalline surfaces concerning to the exchange bias [7, 10–12], however, there have been fewer reports on single crystalline films [13–15] in last decade. There is still a lack of understanding about the spin structure at the interface and the exact mechanism which drives the enhancement in the coercivity of the ferromagnetic film. The exact role of defects and roughness at the interface and in the film, for the magnetic properties of these systems is still a matter of investigation [16, 17]. Determination of these aspects is of utmost significance to gain a better understanding about the FM-AFM interface.

The link between lattice strain and magnetization is given by the magnetoelastic (ME) coupling, which is defined as the strain derivative of the magnetic

anisotropy energy [18]. There have been some reports [19–24] on strained Fe film that demonstrate deviation of ME coupling from the bulk value. The role of film strain is decisive for the deviation. In contrast to bulk, the spontaneous magnetization direction of ferromagnetic thin films also changes, and so-called spin reorientation transition (SRT) is observed. It depends on the thickness [25, 26], temperature [27], and stress in the film [28].

The goal of this thesis is to measure stress during deposition of antiferromagnetic oxides (NiO and CoO) on Ag(001). We want to explore the influence of antiferromagnetic oxides on ferromagnetic Fe films, which are grown on top of NiO and on CoO/Ag(001). Two important magnetic properties *e.g.* coercivity and magnetoelastic coupling of the Fe film on the oxide layers are addressed in this thesis. We focus on coercivity of the Fe film on two antiferromagnetic oxides (NiO and CoO) grown on Ag(001). Also, the magnetoelastic coupling of Fe on NiO/Ag(001) is measured. The antiferromagnetic order of oxides drives the large coercivity and induces a drastically different ME coupling coefficient B_2 . The correlation between stress, strain, structure and magnetic anisotropy is discussed, also the spin reorientation transition of Co monolayers on Pt(111). Our results identify a new issue, the deviation of the ME coupling coefficient B_2 of Fe films on NiO/Ag(001) in sign and magnitude driven by an adjacent NiO film. This issue has not been addressed so far. The measured B_2 of Fe on NiO/Ag(001) differs from B_2 of the Fe film on Ag(001) in sign and magnitude, and this points the importance of an antiferromagnetic NiO film for the modified ME coupling.

This thesis is organized as follows. Chapter 2 introduces the basic theoretical concept of stress in epitaxial films, magnetoelastic coupling of ferromagnetic films and focusing on the magnetization of FM/AFM bilayers. The experimental equipments used for this work, especially the cantilever bending technique, and magneto-optical Kerr effect (MOKE) are described in chapter 3. The same chapter specifies the preparation of samples and surface characterization techniques like AES (Auger electron spectroscopy) and LEED (low energy electron diffraction). In chapter 4, I present the experimental results on stress and magnetism of Fe films on NiO and CoO on Ag(001). In this chapter, it is shown that the NiO induced stress on Ag(001) can be determined by linear elasticity theory, whereas CoO reveals significantly reduced stress compare to the misfit stress. Furthermore, stress and spin reorientation transition in Co film on Pt(111) are presented. Chapter 4 closes with a description of misfit stress in Ag film on Pt(111) at room temperature and it addresses also stress during growth at different temperatures.

All experimental results are discussed in chapter 5. The correlation between stress and structure is discussed for NiO on Ag(001), and Fe on top of 20 monolayers of NiO on Ag(001). The coercivity of the Fe film is very large on NiO and on CoO on Ag(001). The magnetoelastic coupling coefficient B_2 of the Fe film on NiO on Ag(001) is strongly affected by Fe-NiO interface exchange coupling. Here, the results are critically assessed in view of literature values.

The discussion of the SRT of the easy axis of magnetization of the Co film on Pt(111) from the out-of-plane to the in-plane with increasing thickness and also with temperature dependent growth closes the chapter. The main conclusions of the results are presented in chapter 6.

Chapter 2

Fundamental concepts

Stress, strain, morphology, and the magnetic behavior of ferromagnetic ultra thin epitaxial films are closely linked properties. The epitaxial misfit between film and substrate may induce strain and consequently stress in the film that may also influence the growth mode. Structure, morphology, and strain determine the magnetic properties of the film. Magnetic anisotropy is influenced directly by structure, morphology, and indirectly by strain via the magnetoelastic coupling [28, 29]. Hence, a basic understanding of all underlying principles is essential.

2.1 Surface stress

The concept of surface stress is a well discussed topic in the context of reconstruction at single crystalline surfaces and in examining the influence of adsorption process on surface stress. Adsorption processes induce modifications of geometric structure and physical properties of the substrate surface [30]. The basic definition of surface stress is the required force per unit length to elastically stretch or contract the surface [30, 31]. At the surface the local atomic environment is different from the interior of the bulk, the coordination of the surface atoms is changed and the electronic charge redistributes to attain the lowest energy. As a result, a mechanical stress develops in the surface layer, and this is known as the surface stress. Unlike the surface free energy, which is always positive, surface stress can be positive (tensile) and negative (compressive). Often, the calculated surface stress for transition metals is positive, *i.e.*, tensile [32]. The surface stress can also be associated with a solid-solid interface, which is referred as interface stress [30, 31, 33]. A tensile surface stress takes place if the bond between surface atoms prefer a shorter bond length than in the bulk. In contrast, if surface atoms tend to repel each other, a compressive surface stress will be induced. Similarly, a thin film rigidly attached to a surface would create a tensile or compressive surface stress as it contracts or expands, respectively. This will be described in the next section. A change of the surface stress at the solid-vacuum and at the solid-solid interface is measured when the substrate is exposed to adsorbates or during deposition of films. A direct mea-

surement of the surface stress is not feasible so far [30]. Surface stress changes are measured by a bending technique. The idea behind is that a change in the surface stress on either surface of a thin crystal substrate leads to a bending. The bending can be analysed from the bulk elastic constants of the substrate to give the surface stress change [30, 34]. This bending can be detected by the deflection of a laser beam [34], a change of a capacitance [35], or by using a scanning probe microscope [36]. Surface stress has been recognized as a decisive factor to determine a variety of phenomena, for example surface reconstruction, interfacial mixing, self-organization, and hybridization at solid surfaces [36–39]. In calculations, the surface stress is determined as strain derivative of surface free energy at 0 K [39–42].

2.2 Stress and strain in epitaxial growth

In epitaxial pseudomorphic growth, the in-plane unit cell of the film adapts the dimensions of the substrate surface unit cell. This leads to a well defined strain in the film. Generally, stress in an epitaxial film arises due to lattice mismatch between the film and the substrate. The lattice mismatch is defined by the difference between the lattice constant of the substrate a_S and the lattice constant of the film material a_F as $\eta = (a_S - a_F)/a_F$. It determines the strain in an epitaxial film, which can be tensile or compressive. The induced strain in the film can play an important role in the properties of the film material, *e.g.*, it can stabilize crystalline phases which are not available in the bulk [1–3]. A lattice strain of several percent is far above the elasticity limits of bulk samples, however, in the monolayer regime large strain in the percent range is often observed [21, 43].

For epitaxial growth, if the lattice constant of the film material in the bulk is larger than the lattice constants of the substrate, the film stress causes a compressive stress (negative stress) in the film. Conversely, if the lattice constant of the film is smaller than that of the substrate, the film causes a tensile stress (positive), as shown in Figure 2.1. Consequently, a sample bending is observed for a thin substrate and this bending technique can be used to determine the stress in the ultra thin film quantitatively with sub-monolayer sensitivity and high accuracy, as will be introduced in chapter 3. The epitaxial misfit stress can be calculated by linear elasticity theory using elastic constants of the film as:

$$\tau = \frac{Y}{1-\nu}\eta$$

where Y and ν are the Young's modulus and Poisson's ratio of the film respectively, $(\frac{Y}{1-\nu})$ describes the biaxial nature of the stress. And, elastic anisotropy is considered for calculation of these properties for the particular crystallographic orientations of interest [28].

As the epitaxial film becomes thicker with continues deposition of the material,

it can grow under uniform elastic strain. The strain energy per unit volume is constant. Beyond a certain thickness the stored strain energy becomes so large that the formation of dislocations, and/or structural defects are energetically favorable to relax the elastic strain. Structural changes like the formation of misfit dislocation networks [44], the change of in-plane atomic positions from pseudomorphic to coincidence structures, and from epitaxial to 3D growth [45–47] have been ascribed to the reduction of the elastic energy density in the growing film.

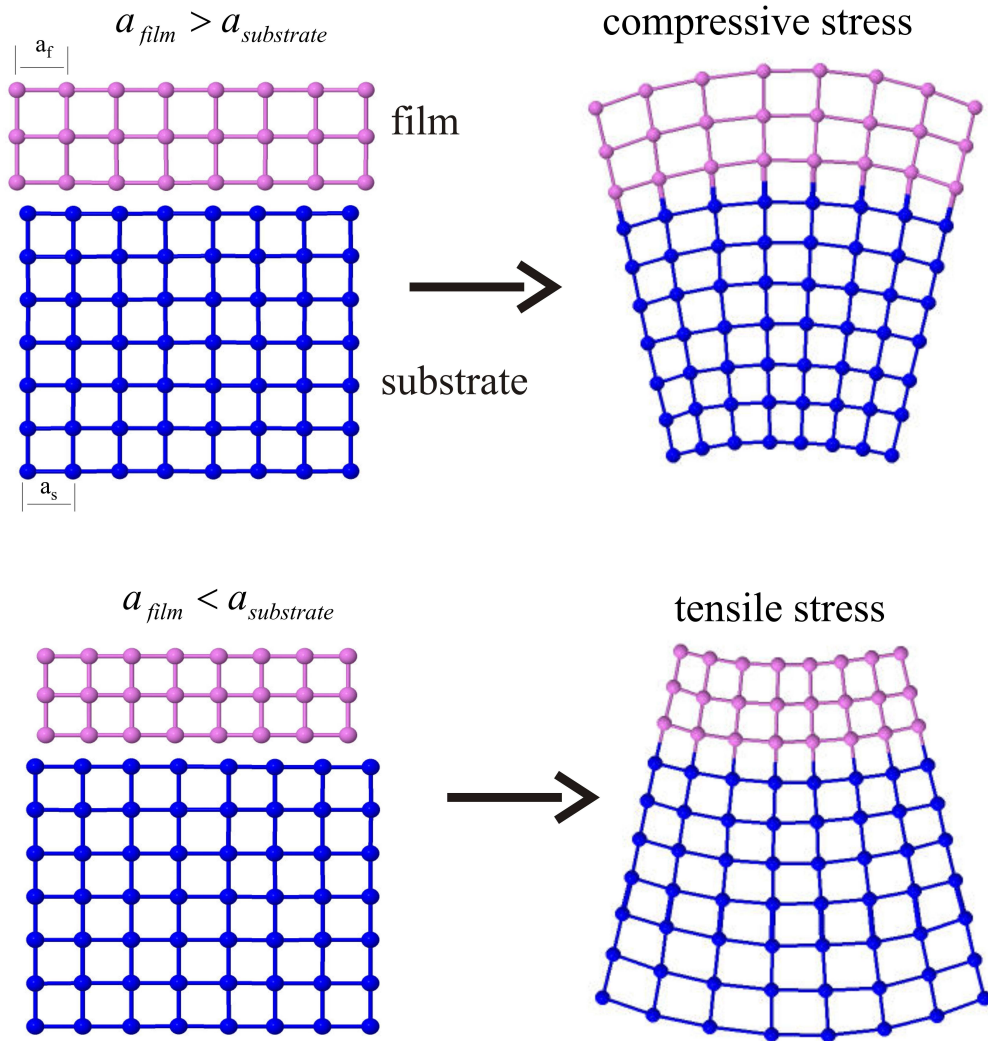


Figure 2.1: Simplified sketch for compressive and tensile stress induced by the film depending on the lattice misfit with respect to the substrate. Both stresses induce a bending of the film-substrate composite. For illustrative purpose I sketched "on-top" bonding sites for the film growth on the substrate, when both belong to a simple cubic system.

Also, at a thickness beyond pseudomorphic growth, stress can provide quan-

titative results on strain, in combination with structure detection techniques such as LEED, SXRD, and possibly STM.

At the very beginning of the growth, a new interface is formed. The respective change of surface and interface stress might be dominant over epitaxial misfit stress as mentioned earlier. For example, stress during growth of NiO on Ag(001) surface is tensile up to 1–2 ML. It turns into compressive stress with increasing thickness as expected from the lattice mismatch. This is presented in Section 4.1. Different growth regimes can be identified from our stress measurements.

2.3 Magneto-elastic coupling in thin films

The magnetoelastic (ME) coupling is defined as the coupling between magnetization and elastic strain in the film [18, 28]. In bulk system, it gives rise to magnetostriction which describes the change of the dimensions of a ferromagnetic sample with the external magnetic field, as depicted in Figure 2.2 (a). In thin films, the atoms are confined laterally, and the film cannot change its length. Only stress is induced upon re-orientation of magnetization that leads to bending of the substrate-film composite, see Figure 2.2. The corresponding free energy density is the magnetoelastic coupling energy. For cubic system it can be described as:

$$f_{me} = B_1(\epsilon_{11}\alpha_1^2 + \epsilon_{22}\alpha_2^2 + \epsilon_{33}\alpha_3^2) + 2B_2(\epsilon_{23}\alpha_2\alpha_3 + \epsilon_{31}\alpha_3\alpha_1 + \epsilon_{12}\alpha_1\alpha_2) + ..(2.1)$$

where α_i and ϵ_{ij} ($i, j = 1, 2, 3$), are the direction cosines of the magnetization with respect to the cubic axes and the strain along the crystallographic directions, respectively. B_1 and B_2 are the first-order ME coupling coefficients. The dots indicate higher-order strain terms [28]. For bulk Fe, the resulting magnetostrictive strain $\delta l/l \sim \lambda$ is of the order of 10^{-5} [48]. And, the magnetoelastic coupling coefficients of bcc bulk Fe are $B_1 = -3.43 \text{ MJ/m}^3$, where a negative sign suggests that Fe expands upon magnetization along a cubic axis [100] and $B_2 = +7.83 \text{ MJ/m}^3$. The relation between the magnetostrictive strains and the magneto-elastic coupling coefficients are used to define the so-called magnetostriction constants $\lambda_{100}, \lambda_{111}$ in terms of B_1 and B_2 , respectively [18, 28]:

$$\lambda_{100} = -\frac{2}{3} \frac{B_1}{(c_{11} - c_{12})} \quad , \quad \lambda_{111} = -\frac{1}{3} \frac{B_2}{c_{44}} \quad (2.2)$$

Where c_{11}, c_{12} and c_{44} denote the elastic constants of the material. The magnetoelastic coupling coefficients B_1 and B_2 can be calculated from the magnetostrictive strain and from the elastic constants c_{ij} of bulk samples. However, the magnetic properties of ferromagnetic epitaxial thin layers on the substrate often deviate from their bulk behavior [21, 24, 28, 49–52]. The coupling coefficients B_i are determined from magnetoelastic stress measurements by exploiting

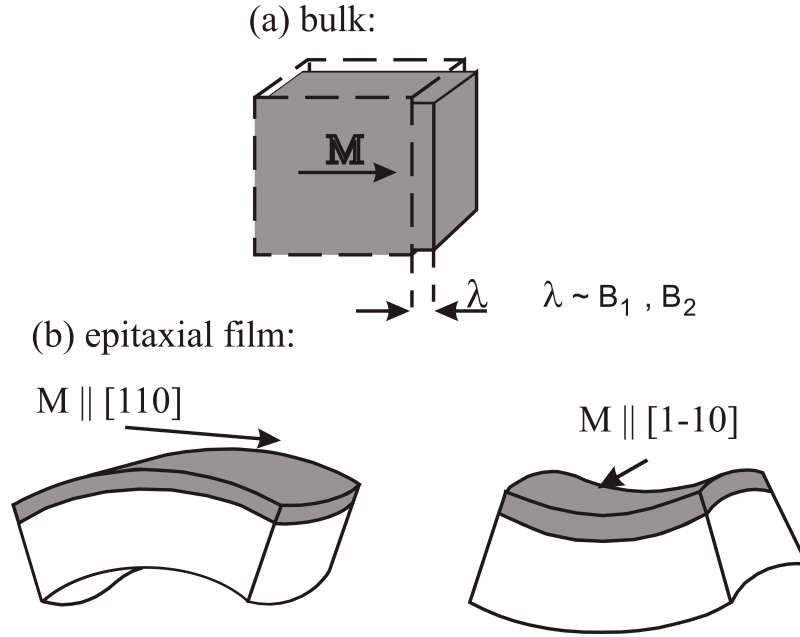


Figure 2.2: (a) The magnetoelastic coupling in a bulk sample, induces a magnetostrictive strain $\delta l/l = \lambda$ in the sample. (b) The magnetoelastic coupling in a magnetic thin films on a substrate induces a magnetostrictive stress that leads to bending in the thin film-substrate compound [55, 56].

the stress-induced bending of a thin film substrate upon reorientation of magnetization, as depicted in Fig. 2.2 (b). A fascinating result of recent experimental and theoretical work is that lattice strain modifies the magnetoelastic coupling, which determines the orientation of the film magnetization. For Fe monolayers on W(100) even a change in sign of the magnetoelastic coupling coefficients has been found as compared to the bulk Fe [28]. Theory indicates that the magnetic anisotropy changes with lattice strain in a non-monotonic manner [22, 53, 54]. Thus, both experiment and theory indicate that the application of bulk magnetoelastic coupling coefficients may not be appropriate to predict the magnetic anisotropy of strained films [28].

The ME stress induced curvature of the film-substrate composite is measured by our cantilever bending beam technique, as explained in chapter 3. The direction of magnetization defines which magnetoelastic coupling coefficients B_i are measured. For the present case, the Fe film is oriented along the length of the thin substrate along the $[110]$ direction, and the width is parallel to the $[1\bar{1}0]$ direction. These directions are 45° off from the cubic axes with the same origin in the plane (001), as shown in Figure 2.3.

When the film is magnetized along a direction $[110]$, The direction cosines: $\alpha_1=1$, $\alpha_2=1$ and $\alpha_3=0$; when magnetized along the $[1\bar{1}0]$ direction, $\alpha_1=1$, $\alpha_2 = -1$ and $\alpha_3=0$. If the crystallographic directions of the film are not oriented to coincide with the cubic crystal axes, a strain tensor transformation should be

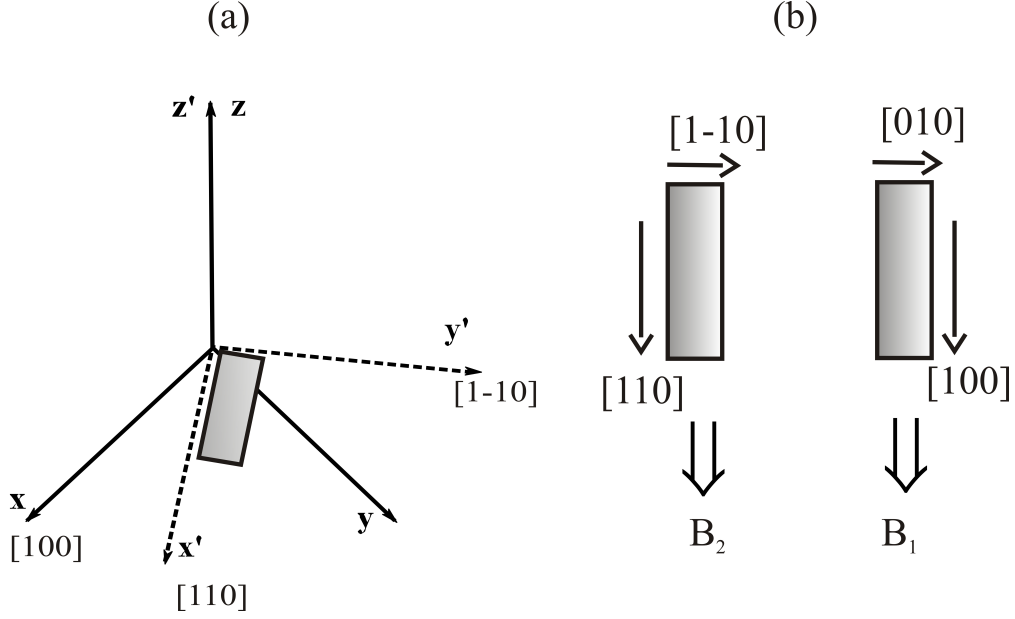


Figure 2.3: Geometrical representation of crystallographic directions of the sample for magnetoelastic coupling measurement in this work. Length and width of the sample parallel to the $[110]$ and $[\bar{1}\bar{1}0]$ directions of the crystal axes in the film, for B_2 measurement. These directions are rotated by 45° from basic directions of the cube.

properly done to obtain the corresponding stress-strain relation. One derives B_2 by taking the difference of the partial differential of Equation 2.1 with respect to strain in these directions, described as follows [28]:

$$\Delta\tau = \tau_1^{M\parallel 110} - \tau_2^{M\parallel \bar{1}\bar{1}0} = \frac{\partial f_{me}(M\parallel 110)}{\partial \epsilon'} - \frac{\partial f_{me}(M\parallel \bar{1}\bar{1}0)}{\partial \epsilon'} = B_2 \quad (2.3)$$

Here, ϵ' denotes the strain and $\Delta\tau$ is stress change. Previous work has shown that deviations of ME coupling constant of thin ferromagnetic film depend on the strain in the film [19–21, 23, 57–59]. From our present experiments, it is found that the ferromagnetic (Fe) film in contact with antiferromagnetic film (NiO) leads to interesting results such as an enhanced coercivity of the Fe film, as presented in chapter 4. Also, the magnetoelastic coupling deviates sharply from the respective value of bulk Fe.

2.4 The magnetic coupling between a ferromagnetic and an antiferromagnetic film

Complex and interesting properties result when ferromagnetic (FM) films are grown on antiferromagnetic (AFM) materials. In this way, they are directly exchange coupled across the interface. The most notable effects are an enhanced coercivity (H_C) and a shift in the hysteresis loop of the ferromagnetic layer,

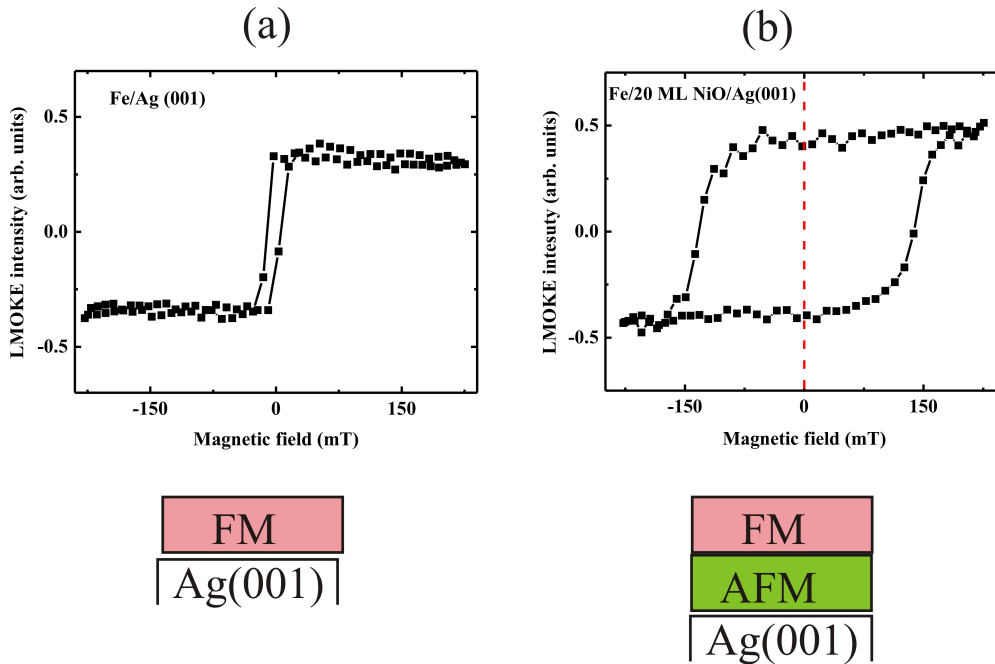


Figure 2.4: Magnetic hysteresis loops for a ferromagnetic (Fe) (left) and a ferromagnet coupled to an antiferromagnet (Fe/NiO bilayers)(right), grown on Ag(001), measured at room temperature. Exchange coupling between the two layers lead to an increase in H_c .

called exchange bias (H_E) [7]. The first model to explain the exchange bias considered the role of an uncompensated interface between the AFM and FM layers [7].

The enhancement in coercivity of the FM film is observed below the Néel temperature T_N . According to the proposed model in Ref. [11], the switching of the FM moments with the applied external magnetic field induces a torque on the magnetic moments of the AFM at the interface, which leads to the formation of partial domain walls in the AFM film parallel to the interface. The spins of the top layer in the AFM get affected, and can be dragged by the spins in the FM during the reversal of the spins. However, deeper layers retain their AFM order. One example of Fe-NiO on Ag(001) is also shown in Figure 2.4. The coercivity of the Fe film in contact with NiO layers is very large. For comparison, the magnetic hysteresis loop of Fe/Ag(001) is shown. The coercivity of the ferromagnetic film increases with the thickness of the antiferromagnetic film and decreases with increasing temperature, as it will be discussed in chapter 5. Note the absence of exchange bias in Fig. 2.4 (b).

Exchange bias may be observed when the FM-AFM bilayer is cooled down in the presence of magnetic field from above T_N , and also the Curie temperature should be larger than T_N [7]. It can be described in terms of an alignment of the AFM spins parallel to the FM spins at the FM-AFM interface occur

during the field cooling procedure. The coupling between the AFM and FM spins at the interface exerts an additional torque on the FM spins due to large stiffness of the AFM order [8, 11], by which the external field has to overcome. As a result, the coercive field in the one field branch of the hysteresis loops increases. Conversely, when the magnetic field is reversed back, the rotation of spins in the FM will be easier than before. Since the interaction with the spins in the AFM will now favor the magnetization reversal, *i.e.*, the AFM will exert a microscopic torque in the same direction as the applied magnetic field. Therefore, the coercive field in this field branch will be reduced. And, the net effect is a shift of the hysteresis loop along the magnetic field axis, H_E . In exchange biased system, the spins in the FM have only one stable configuration (*e.g.*, unidirectional anisotropy). The AFM spin configuration was assumed to remain frozen during the FM spins reversal. The occurrence of H_E depends on many parameters such as thickness of FM and AFM, temperature, interface, etc. [8, 11]. H_E might be zero also, although the film is in AFM order [8].

However, this proposed model is only meaningful for smooth surfaces and interfaces. Here, many parameters such as roughness, intermixing, uncompensated spins, magnetic domains [17, 60, 61] which have been shown to be important in exchange bias, are not taken into account. According to Koon's model [62], perpendicular orientation between the ferro-antiferromagnetic spin directions, similar to the classic spin-flop state in bulk antiferromagnets is required. In contrary to Koon's model for perfectly flat interfaces, spin-flop coupling does not lead to exchange bias, but rather gives rise to a uniaxial anisotropy which causes the large coercivities in FM-AFM bilayers [16, 63].

Chapter 3

Experimental setup

This chapter describes the experimental techniques used for the present work. The first section gives an overview of the ultra-high vacuum (UHV) chamber (Section 3.1) which is equipped with sample characterization techniques such as low energy electron diffraction (LEED) and Auger electron spectroscopy (AES). The second section (Section 3.2) focuses on the optical beam deflection setup that is used to measure surface stress change during film deposition. In section 3.3, I will give a brief description on the magneto-optical kerr effect (MOKE) set up used to measure the magnetic properties of ferromagnetic films. The last section (sect. 3.4) describes the sample preparation.

3.1 Ultrahigh vacuum chamber

The experiments are performed under ultra high vacuum (UHV, base pressure 4×10^{-11} mbar). The schematic of the UHV chamber is shown in Figure 3.1. The chamber can be partitioned in two parts. The lower and the upper part of the chamber can be separated by a gate valve. The upper chamber is equipped with an Auger electron spectrometer (AES), low energy electron diffraction (LEED), a Quadrupole Mass Spectrometer (QMS), an ion gun, and three evaporators to deposit thin metallic films. The lower chamber is equipped with an evaporator and electromagnets that can produce magnetic fields of up to 0.4 T in the longitudinal and polar sample directions, and 0.1 T in the vertical direction. Several leak valves allow to introduce partial pressures of gases reliably.

In the upper part of the chamber, the sample and thin metallic films as well as metallic oxide films are prepared. Also, stress is measured during film growth using an optical beam deflection setup [34], which is explained in the following section. To prepare oxides like NiO, an oxygen gas tank (1 liter@12 bar) is connected to the chamber via a leak valve. The MOKE setup is mounted (externally) to the lower chamber to measure magnetic properties of the sample. Fig. 3.1 shows the UHV compatible arrangements of two electromagnets to the lower chamber [56, 64]. This magnet is rotatable around the vertical axis to apply the magnetic field parallel and normal to the sample surface. In

addition, a water cooled magnet is inserted into the bottom of the chamber to produce a vertical field. This magnet assembly is essential to rotate the sample magnetization in-plane for magneto-elastic measurements, as explained in Sec. 3.3.

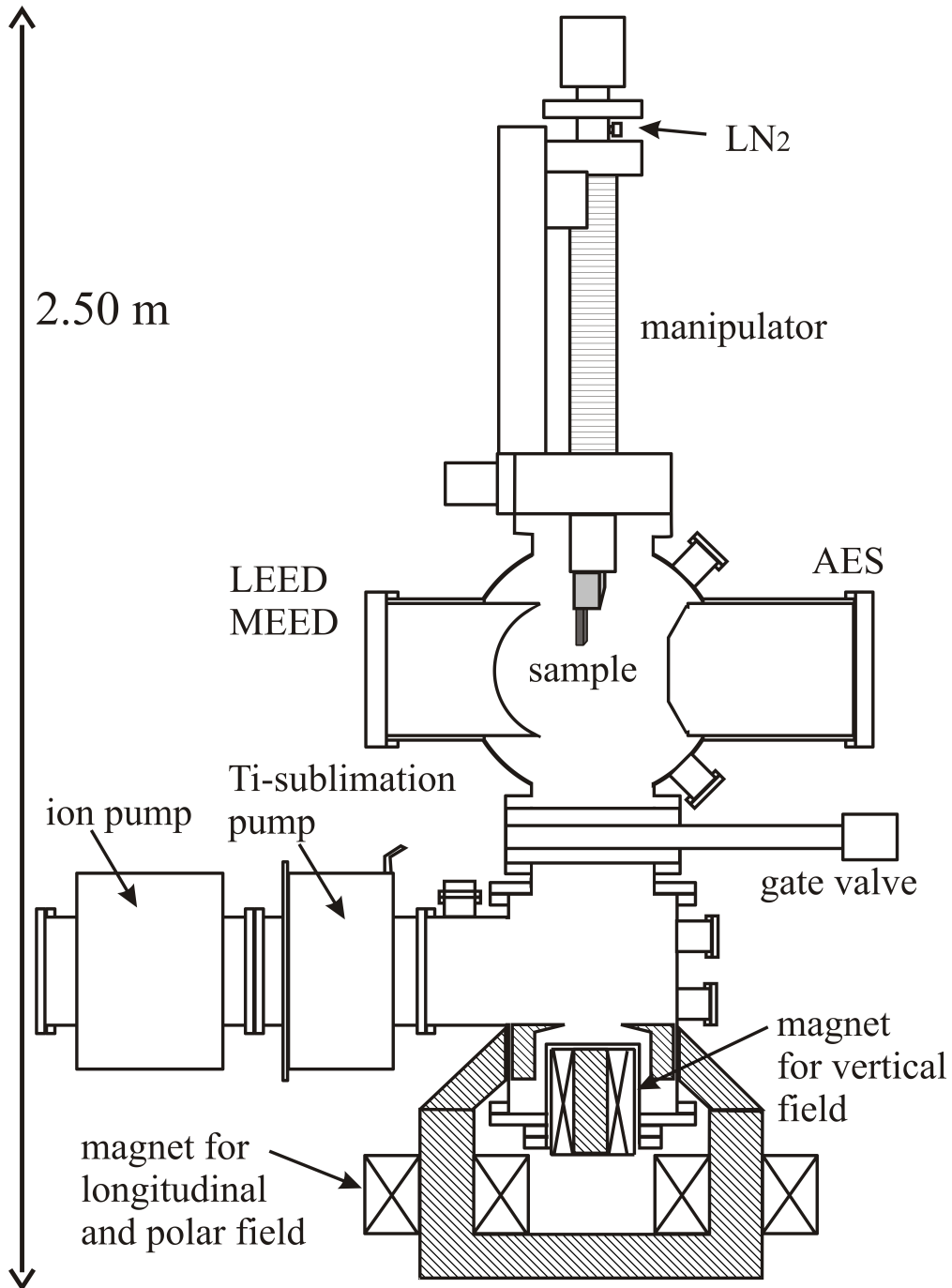


Figure 3.1: Schematic of the UHV chamber.

Our cantilever sample is fixed to the sample holder at the bottom end of the manipulator rod. The manipulator has five degrees of freedom (X , Y , Z , rotation, and tilt), which helps to do fine alignment for stress and LEED measurements. The temperature at the sample can be raised to more than 1500 K by e-beam heating from the back of the sample. In order to ensure uniform heating throughout the sample and to avoid overheating, a W-shield is placed in between the sample and the e-beam heater. While heating, the shield is heated by e-beam bombardment, and then the radiation from the shield heats the sample. The sample can be cooled down with a liquid-nitrogen (LN_2) reservoir attached to the manipulator. The reservoir is connected to the upper end of the sample via Cu-braid. The lowest temperature at the sample can be 150 K. The temperature is measured by a K-type (NiCr-NiAl) thermocouple fixed close to the cantilever sample.

In the upper chamber, the AES electron gun is located opposite of the LEED screen. In this way, the combination of the AES gun and the LEED screen is used to perform medium energy electron diffraction (MEED) intensity measurements to monitor film growth during deposition. A brief description of the various surface characterization techniques used in the system is given below.

Low energy electron diffraction (LEED)

Low Energy Electron Diffraction (LEED) is one of the most powerful technique to study the structure of single crystal surfaces. It has been proposed for the first time in 1927 by Davisson and Germer [65].

Low energy electrons are sensitive for studying the surface structure because the mean free path of low energy electrons in solids is short (5–10 Å) and the electron's de Broglie wavelength (λ) is equivalent to the typical interlayer distance in a crystal, and thus diffraction can be observed [66].

The working principle is that a mono-energetic electron beam (typical energy range of 10–500 eV), incident normal to the surface of the crystal, is elastically back scattered (reflected). The back scattered electrons form a diffraction pattern on a fluorescent screen. Only the elastically-scattered electrons contribute to the diffraction pattern while the lower energy (secondary) electrons are repelled by a retarding grid. A diffraction pattern is observed as distinct spots of enhanced intensity on the screen (one example is shown in Figure 3.2 (a)). The diffraction pattern can be observed visually or recorded by a video camera.

The diffraction condition for 2D crystal surface is

$$a \sin\theta = \sqrt{h^2 + k^2} n \lambda \quad (3.1)$$

where h , k are miller indices, a is the lattice constant of the crystal, n (integer) is the order of diffraction, θ is the emission angle, and $\lambda = \frac{h}{p} = \frac{h}{\sqrt{2mE}}$. An inspection of the position of the diffraction spots on the screen, allows to extract

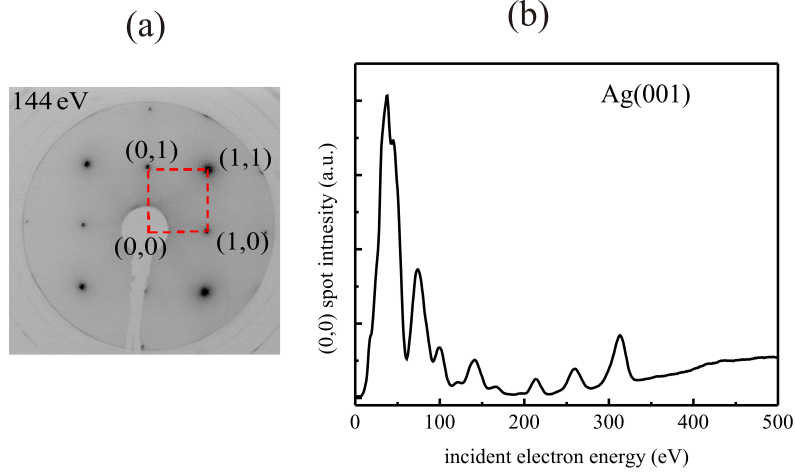


Figure 3.2: LEED image (inverted for better visibility) of a clean Ag(001) surface (a) and energy dependent intensity of (0,0) spot (b). The recording energy and reciprocal unit cell are indicated.

the diffraction angle θ , and from this we can calculate the in-plane atomic spacing $a(\text{\AA})$ as

$$a(\text{\AA}) = \frac{n L 12.26}{l} \sqrt{\frac{h^2 + k^2}{E(\text{eV})}} \quad (3.2)$$

where L is the distance between crystal and the screen (72 mm), and $l(\text{mm})$ is the distance between the one of the primarily diffracted spots and specularly diffracted (0,0) spot.

Thus, the in-plane atomic spacing of Ag(001), for NiO/Ag(001), and also for different thicknesses of NiO on Ag(001) are extracted from the LEED patterns.

Figure 3.2 (a) shows the LEED pattern of the clean Ag(001) surface. The sharp LEED spots and less background intensity indicates the good quality of the sample surface. The analysis gives $a = 2.9 \pm 0.1\text{\AA}$, which is in good agreement with the tabulated value of bulk Ag.

In addition to the LEED patterns, the intensity of the diffracted spots is also measured as a function of energy of the incident electron beam. A commercial package-AIDA2000/specs [68] is used for this purpose. One obtains LEED-I(V) spectra. As an example, Figure 3.2 (b) shows the LEED-I(V) curve obtained for the (0,0) spot of Ag(001), which was visible by rotating the sample (7°) from the normal incidence. The intensity of LEED spots changes with the primary energy. The kinematic analysis of the LEED I(V) spectra provides information on the vertical lattice spacing. The intensity peak occurs only at those energies, at which the Bragg diffraction condition is satisfied. It can be written as

$$2 d \cos \theta = n \lambda \quad (3.3)$$

Table 3.1: In plane atomic distances of the crystals used in this work, are listed here along their crystallographic direction along the length. The values are extracted from LEED by using equation 3.2.

Crystals	direction along the length of the crystal	In-plane atomic distance,	bulk
		extracted from LEED	
		Å	Å
Ag(001)	[110]	2.9 ± 0.1	2.89^a
Ag(001)	[001]	2.9 ± 0.1	2.89^a
Pt(111)	[110]	2.8 ± 0.2	2.77^a

^aref. [67]

which can be rewritten in the form of the primary electron energy

$$E = \left(\frac{n^2 h^2}{8m_e d^2 \cos^2 \theta} \right) + V \quad (3.4)$$

where θ is the angle between incident electron beam and surface normal and V is the inner potential. The correction term V is added because the wavelength of the electrons changes in the crystal. The dependence $E(n^2)$ represents a linear function [69].

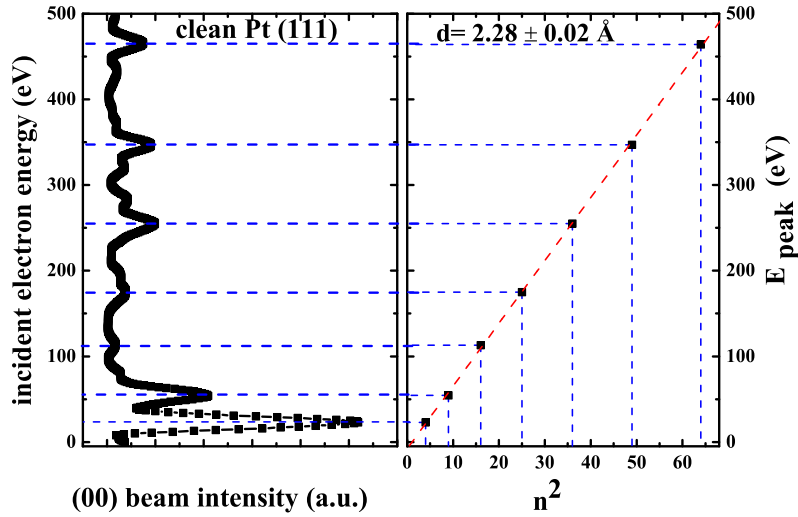


Figure 3.3: LEED $I(V)$ spectra (energy dependent intensity of (0,0) spot) and the linear fit of $E_{peak} \propto n^2$ relation for clean Pt(111) at 300 K.

The interlayer distance d is determined from the slope. Figure 3.3 shows the results of the I–V profile (left one) for the specularly reflected electron beam, incident at an angle of 7° to the normal to the surface, and E vs n^2 plot (right one) for clean Pt(111) at room temperature. The slope of linear fit indicates an average interlayer spacing of Pt(111) of $2.28 \pm 0.02 \text{ \AA}$. This is in quantitative agreement with the interlayer distance of bulk fcc Pt(111) of 2.27 \AA . A more refined dynamical LEED analysis needs to be performed to also identify layer relaxation phenomena at surfaces [4, 70]. More detailed information about LEED-I(V) measurements, as used in the data analysis, will be presented in chapter 4.

Auger Electron Spectroscopy (AES)

Auger Electron Spectroscopy (AES) is a standard technique in surface science. It is used predominately to check the cleanliness of a freshly prepared surface under UHV conditions, and also for studies of film growth and surface chemical composition. I also apply the e-gun of the AES-setup for MEED studies on film growth.

In the present work, an electron gun with an energy of 3 keV and a Cylindrical Mirror Analyzer (CMA) [71] with a working distance of about 18 mm are used. AES spectra are recorded by a Labview program on a PC. The short inelastic mean free path (IMFP) of Auger electrons in solids ensures the surface sensitivity of AES. Examples of AES data are shown in section 3.4.

3.2 Optical beam deflection setup

The optical beam deflection setup [34, 56, 72] is used to monitor the bending of the cantilever sample during film growth or gas adsorption. The setup is also used for magnetoelastic stress measurements during switching of magnetization in two orthogonal directions in the plane of the film [28]. In this work the optical beam deflection technique is applied to measure stress in thin metallic films and oxides during growth on single crystal as a substrate and to measure magnetoelastic stress of deposited ferromagnetic monolayers. The results are discussed in Chapter 4. Measurements by this technique can be performed at different but constant temperatures in the range of 150–1100 K [64, 73, 74].

A photograph of the optical beam deflection setup and the corresponding schematic are presented in Figure 3.4 (a) and (b), respectively. A thin ($\approx 0.1 \text{ mm}$) rectangular substrate is clamped along its width ($\approx 2.5 \text{ mm}$) at the top end and the bottom end is free. It works as a cantilever that will bend when its front and backside experience a stress difference. In the setup, a laser beam ($\lambda = 670 \text{ nm}$) is splitted into two beams by a beam splitter. These two beams hit to the cantilever crystal at two positions, typically 3–4 mm apart in the

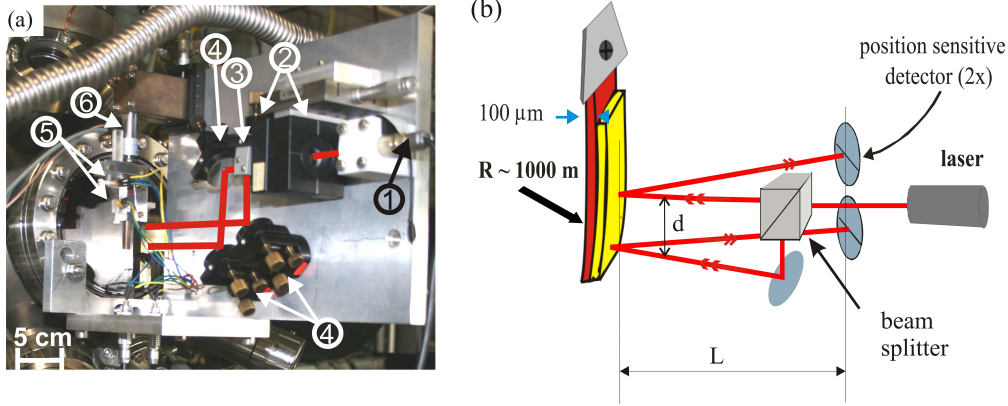


Figure 3.4: (a) An image of the optical beam deflection setup that is mounted on one of the UHV viewports (in front of the sample surface): 1-laser diode, 2-focus lens, 3-beam splitter, 4-mirrors, 5- position sensitive detectors, 6-piezo for calibration. (b) Schematic representation of stress measurement. R : the radius of curvature, L : distance between the substrate and the detector, and d : separation of laser beams at the sample. [75]

lower area. The reflected beams are detected on two position sensitive detectors (split photo diode). The difference of these two position signals gives access to the curvature of the sample. From the geometry of the setup (see Fig 3.4 (b)), the curvature can be expressed as:

$$\kappa = \frac{1}{R} = \frac{\Delta P}{2dL} \quad (3.5)$$

where L is the distance between the sample and the detector (≈ 280 mm) and d is the beam separation at the sample (≈ 3 -4 mm). ΔP is the difference of change in position of the bottom and the top signals. The conversion of the position signal (in volt) from the split photo-detector to a spot deflection (in nm) is accomplished by a calibration by moving the detectors by a known distance ($15 \mu\text{m}$) with a calibrated piezo drive. The resulting change of the position signal (≈ 0.7 V) gives the calibration factor. This calibration is done before and after deposition for every measurement.

The measurement of the curvature change ($\Delta \frac{1}{R}$) of a substrate gives quantitative values for the underlying stress change. A thin (≈ 0.1 mm) rectangular substrate is used. A large length to width ratio ensures a free 2D- bending (length ≈ 13 mm to width ≈ 2.5 mm ratio is greater than 3 [76]) to bend freely in two directions. Under these conditions, the relation between stress change $\Delta \tau = \tau_F \cdot t_F$ and curvature change $\Delta \frac{1}{R}$ is given by the modified Stoney equation [28, 77], which describes free two-dimensional bending due to a biaxial stress state as

$$\Delta \tau = \Delta(\tau_F \cdot t_F) = \frac{Y_s t_s^2}{6(1 - \nu_s)} \Delta \frac{1}{R} \quad (3.6)$$

Table 3.2: Elastic constants: Young's modulus Y , Poisson ratio ν , and biaxial modulus $\frac{Y}{1-\nu}$; and the thickness of Ag and Pt.

	Y (GPa)	ν	$\frac{Y}{1-\nu}$ (GPa)	t_s (μm)
Ag(001) ^a	43.67	0.423	75.68	100
Pt(111) ^b	185	0.45	336.36	115

^aref. [73]

^bref. [32]

where Y_s and ν_s are the Young modulus and the Poisson ratio of the substrate, respectively. The substrate thickness is given by t_s , and τ_F and t_F are the film stress and the film thickness, respectively. The elastic properties of crystals are anisotropic, and therefore proper tensor transformations are performed to get the appropriate values of Y and ν for a particular substrate surface orientation [28, 78]. Table 1 summarizes the data for the crystals used in this work.

A Detailed discussion of stress and elastic anisotropy can be found in Ref. [28, 76]. As a rule of thumb, epitaxial strain of one percent induces stress of one GPa which induces a curvature change of several 1/1000 m.

In magnetoelastic stress measurements, we monitor the change of curvature of the sample, while a reorientation of the film magnetization along two orthogonal directions (along the length to along the width) is induced. The relation between curvature change ($\Delta \frac{1}{R}$) and magnetoelastic stress change is given by [28]:

$$\Delta \tau_{me} = \frac{Y_s t_s^2}{6(1 + \nu_s) t_F} \Delta \frac{1}{R} \quad (3.7)$$

The magnetoelastic coupling coefficients B_i are determined from: the magnetoelastic stress change upon reorientation of the magnetization along the length and the width of the sample.

$$B_i = \tau_{me} \left| \frac{\partial M_{\parallel length}}{\partial \tau_{me}} - \frac{\partial M_{\parallel width}}{\partial \tau_{me}} \right|$$

or

$$B_i = \frac{Y_s t_s^2}{6(1 + \nu_s) t_F} \left(\frac{1}{R_{length}} \left| \frac{\partial M_{\parallel length}}{\partial \tau_{me}} \right| - \frac{1}{R_{width}} \left| \frac{\partial M_{\parallel width}}{\partial \tau_{me}} \right| \right) \quad (3.8)$$

In my experiments, a crystal orientation was chosen such that the epitaxial orientation of Fe was Fe[110]|| sample length. Thus, B_2 was obtained, as explained in Sec. 2.3. A magnetization switching along $\langle 100 \rangle$ directions gives B_1 [28]. The results are presented in chapter 4 and discussed in chapter 5. In this work,

the magneto-elastic coupling coefficients B_2 is measured for Fe/NiO/Ag(001) and also for Fe/Ag(001).

3.3 Magneto-optical Kerr effect setup

The Magneto-optical Kerr effect (MOKE) [79, 80] setup is used to measure magnetic hysteresis loop of ferromagnetic layers *in-situ*. The basic principle of MOKE is that when a polarized light reflected from a magnetic sample, both the plane of polarization and the ellipticity of the reflected light, as well as its intensity change. The reflected light is described by a Kerr rotation and a Kerr ellipticity. Both quantities are expected to be within certain approximations proportional to the total magnetic moment of the sample, provided that the film thickness is significantly smaller than the optical penetration depth of the light [81]. This is fulfilled in MLs regime, but not in several tens of nm thick film. On a microscopic level the origin of MOKE is that the electric field of the propagating light couples with the electron spin via spin-orbital interaction [82].

There are three different modes of operation (Kerr configurations) based on the orientation of the sample magnetization with respect to the scattering geometry, called longitudinal, polar and transverse MOKE. In the longitudinal Kerr effect, the magnetization is in the film plane and in the scattering plane of the light. In the transverse Kerr effect, the magnetization is also in the film plane, but it is perpendicular to the scattering plane. In the polar Kerr effect, the magnetization direction is perpendicular to the plane of the film (along the surface normal). Longitudinal and polar Kerr effect measurements lead to a Kerr rotation and ellipticity. Transversal Kerr measurement induces an intensity change in response to an applied magnetic field [81].

The MOKE setup used in this work is based on a polarization modulation technique. In Figure 3.5 (a), the arrangement of the electromagnets designed for *in-situ* measurements is shown. The horizontal magnet (yellow) that is used for longitudinal and polar MOKE, which is rotatable about the vertical axis, has its coils outside the UHV chamber, but its yoke extended into the chamber. The vertical magnet (cylindrical shaped) is inserted into the bottom of the chamber [56, 83]. The schematic representation of the MOKE setup is shown in Figure 3.5 (c). For the measurement, laser light ($\lambda = 670$ nm) from a laser diode [84] passes through the polarizer and hits the sample. The polarized light reflected off the sample and goes through a $\lambda/4$ wave plate and a photo-elastic modulator (PEM) to another polarizer (which acts as an analyzer) and finally hits the detector. Here, the $\lambda/4$ wave-plate is used to compensate the birefringence from the UHV window (glass) [79] and metallic reflection from the sample. The preamplified output signal from the detector (photo diode)

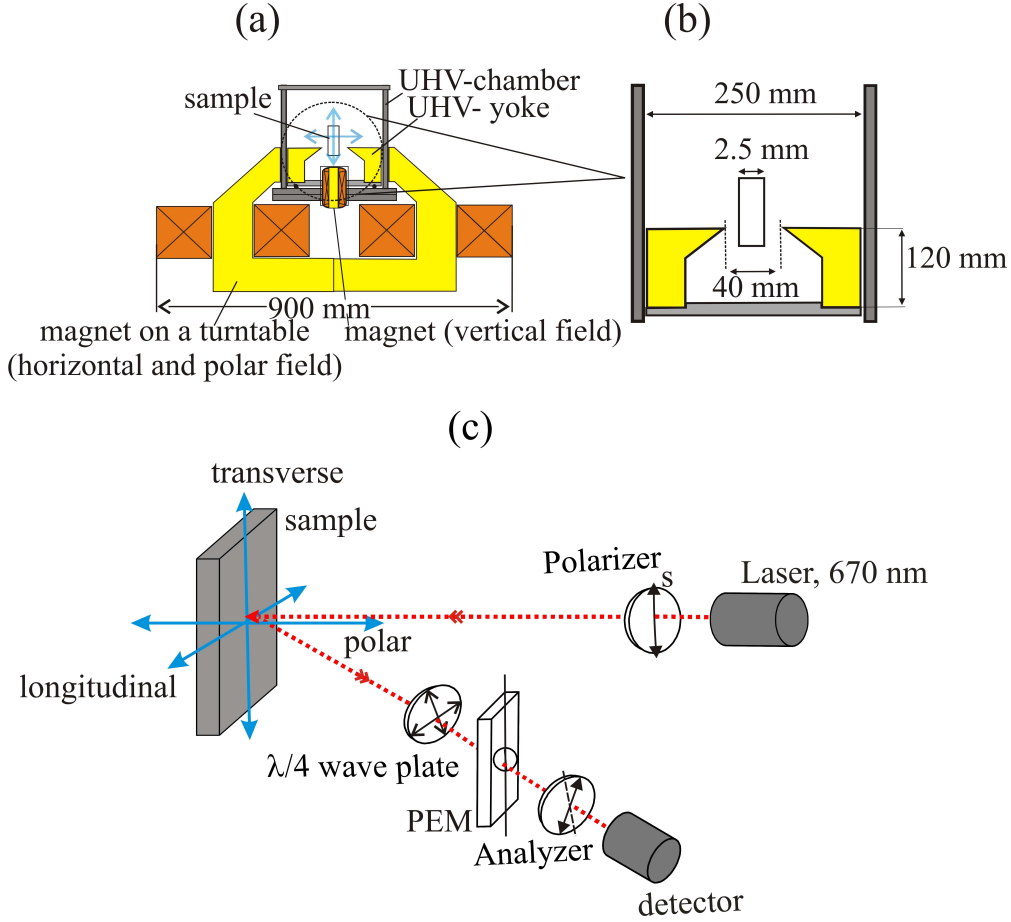


Figure 3.5: Schematic representation of the MOKE setup. (a) Arrangement of the magnets designed for UHV measurements. The horizontal magnet is used for longitudinal and polar MOKE. It is rotatable around the vertical axis, and it has its coils outside the UHV chamber, but its yoke extended into the UHV chamber. The vertical magnet (cylindrical shaped) is inserted from the bottom of the chamber [56, 83]. (b) The magnified view of the sample and yoke with scale. (c) MOKE setup with all three geometries indicated by blue arrows. *s*-polarized laser is used for longitudinal and polar MOKE. For transversal MOKE *sp*- or *ps*- polarized beam is used.

as well as a reference signal from PEM (at twice the fundamental frequency: $2f$) are sent to a lock-in amplifier (LIA). This $2f$ signal is measured by the LIA and its output is normalized to the DC signal. This signal is assumed to be directly proportional to the total magnetic moment of the sample within the limitations stated above.

For longitudinal and polar MOKE measurements, the incident beam is *s*-polarized by a polarizer and the analyzer is set away by 45° from *s*-polarization direction, as sketched in the Figure 3.5 (c). In the transverse MOKE geometry the vector product of the magnetization and the electric field of the incident light is zero; therefore, changes in the polarization state of the light are not observed, only the intensity of the light will be affected. To measure transverse MOKE, the

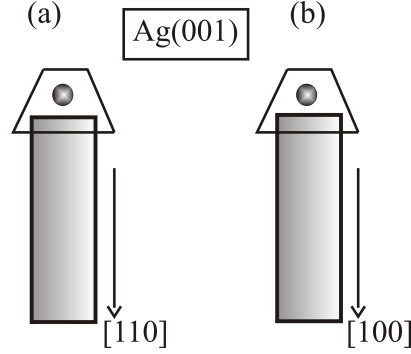


Figure 3.6: Pictorial view of Ag (001) crystal with two different crystallographic directions along the length: (a) has used for all the MOKE measurements of Fe/NiO/Ag(001) and (b) is used for magnetoelastic measurements.

polarizer is set away by 45° from the s -polarization direction (*i.e.* sp - or ps -polarization). The major axis of the PEM and the analyzer are also rotated 45° accordingly, and the $\lambda/4$ wave-plate is removed.

3.4 In-situ sample preparation

Two single crystal substrates of Ag(001) and Pt(111) surface orientations are used in this work. The dimensions are thickness ≈ 0.1 mm, length ≈ 13 mm, and width ≈ 2.5 mm.

We have used two differently cut Ag(001) crystals, as shown in Figure 3.6. To clean the Ag(001) surface, the recipe is adopted from reference [85]. Ag(001) is prepared by sputtering in an Ar partial pressure of 2×10^{-5} mbar at room temperature. Bombardment of Ar ion is performed at 1.5 keV with a typical sample current of $2 \mu\text{A}$. After ion bombardment, the crystal is thermally annealed by heating under UHV conditions at 650 K for 10 minutes. LEED and AES are used to check the crystalline long range order and the chemical composition of the substrate surface, respectively.

The Pt(111) surface is prepared by Ar ion bombardment (2 keV, $I_{\text{sample}} = 3 \mu\text{A}$) at 300 K and 800 K subsequently [86]. Surface contaminations (mainly carbon) are further removed by annealing in oxygen ($P_{\text{O}_2} = 5 \times 10^{-7}$ mbar) at 800 K. After subsequent annealing in vacuum at 1100 K¹ for one minute, a clean Pt(111) is finally obtained, as checked by Auger-electron spectroscopy and a clear (1×1) LEED pattern is observed.

The Auger spectrum and LEED (1×1) pattern of Ag(001) and Pt(111) surfaces are shown in Figure 3.7. Films are prepared onto the freshly prepared crystals.

¹This temperature is measured by pyrometer.

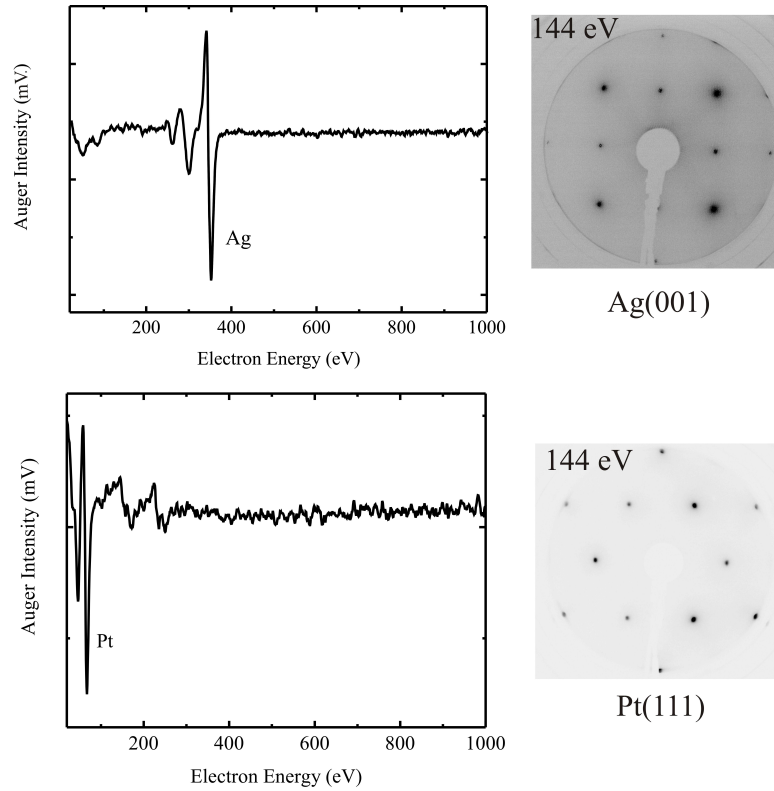


Figure 3.7: Left: Auger spectrum of clean Ag and Pt recorded at a primary energy of 3 keV with a sample current of order $2 \mu\text{A}$. LIA settings were $300 \mu\text{V}$ (sensitivity), the modulation voltage was 1 V, and a time constant of 300 ms in both cases. Right: corresponding LEED images of Ag and Pt.

For deposition of Fe, Co, or Ni, a 4 mm thick rod was used while for Ag deposition on Pt(111) a crucible of Mo (Molybdenum) containing Ag wires was used. The evaporators are water-cooled during film deposition. The partial pressure of the UHV chamber during deposition of metallic film is below 4×10^{-10} mbar.

Chapter 4

Results

This chapter presents the main experimental results of this work. It is divided into four sections. The first section 4.1 focuses on stress and structure of the metallic oxide monolayers NiO and CoO on Ag(001). Section 4.2 deals with stress during the deposition of Fe on NiO and magnetism of this ferromagnetic/anti-ferromagnetic (FM/AFM) layers on Ag(001), where the main focus is Fe on NiO/Ag(001). Finally, stress measurements for Co and Ag monolayers deposition on Pt(111) are performed. Magnetic properties of Co monolayers on Pt(111), which show a thickness dependent spin reorientation transition (SRT), are presented in section 4.3.

4.1 Stress and structure of metallic oxide monolayers on Ag(001)

4.1.1 Preparation of NiO and CoO on Ag(001)

One way to prepare metallic oxide thin films is to deposit the metal in an oxygen partial pressure. Alternatively, the second way is deposit the film first, and then anneal it in an oxygen atmosphere for several minutes. It has been reported that neither Ni [85] nor Co [87] grows epitaxially on Ag(001) due to the large lattice mismatch. Therefore, preparing oxides by the second way is not expected to lead to epitaxial NiO or CoO films, and the first approach is followed here.

For the present work, NiO is formed by deposition of Ni on Ag(001) in an O_2 partial pressure of 2×10^{-7} mbar at room temperature with a growth rate¹ of 0.8 ML per minute. The results presented here by stress and LEED indicate that NiO grows pseudomorphically up to five monolayers. Complementary investigations by surface X-ray diffraction (SXRD) confirm this assessment [88].

¹For NiO, the growth calibration is done by MEED.

CoO is prepared by deposition of Co on Ag(001) substrate in an oxygen atmosphere at a pressure of 2×10^{-7} mbar at 450 K. The film is subsequently annealed in vacuum for 10 minutes at 450 K [87].

4.1.2 Stress and structure of NiO on Ag(001)

The NiO is an oxidic system, with a rocksalt structure and a lattice constant of 4.177 \AA [67]. The bulk crystalline structure is shown in Figure 4.1. The lattice mismatch of NiO with Ag is $\eta = \frac{a_{Ag} - a_{NiO}}{a_{NiO}} = -2.2 \%$ where $a_{Ag} = 4.086 \text{ \AA}$ [67].

The stress change induced by NiO is measured simultaneously with medium energy electron diffraction (MEED) to reveal stress and the growth behavior of the film. We find three different stress regimes and corresponding change in growth behavior of the NiO film. Stress and MEED intensity as a function of deposition time are shown in Figure 4.2. At time zero, oxygen is introduced into the chamber, which induces a small tensile stress change of $+0.7 \text{ N/m}$. With a delay of 250 s the shutter of Ni evaporator is opened. At the onset of Ni deposition a sharp decrease of the MEED intensity is observed, as identified in regime I, where a tensile stress change of $+0.6 \text{ N/m}$ is observed. In this regime, the lack of MEED oscillations and an unexpected tensile stress indicate a peculiar interface formation, where possibly surface stress changes are decisive. Further Ni deposition in regime II leads to pronounced periodic oscillations of the MEED intensity with a period of 75 s, and a compressive stress change of -6.0 N/m is measured. The film stress τ_F as given by the slope of the stress curve is -5.8 GPa . A negative sign indicates compressive stress. The linear region of the stress curve from 1.5 to 5 ML indicates a uniformly strained film. At 640 s, the MEED intensity oscillations decrease in amplitude, and the slope of the stress curve levels off in regime III. After 1750 s the deposition of Ni is stopped, and the oxygen partial pressure turned off.

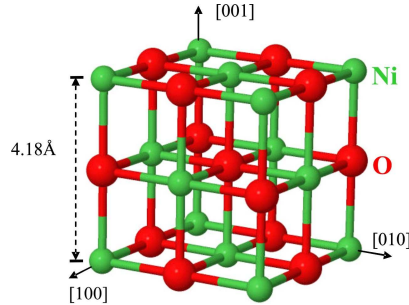


Figure 4.1: Crystal structure of bulk NiO. The lattice constant is taken from ref. [67].

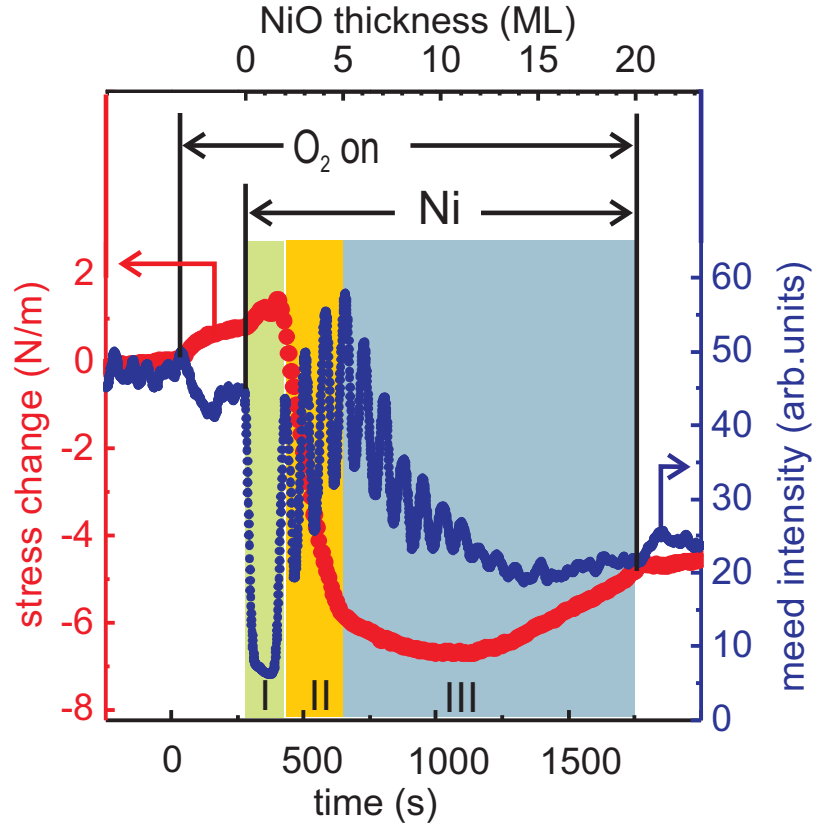


Figure 4.2: Measured stress change (left scale) and MEED intensity (right scale) during Ni deposition on Ag(001) in an oxygen partial pressure of 2×10^{-7} mbar at 300 K. Pronounced MEED oscillations starting from 2 ML are ascribed to layer-by-layer growth of NiO. The compressive stress change from 2–5 ML NiO is due to lattice misfit between NiO and Ag. Three growth regimes are identified from the distinctly different stress and MEED observations. I (0–2 ML NiO): interface formation, II (2–5 ML NiO): pseudomorphic growth, III (5–20 ML NiO): non-pseudomorphic growth.

These three stress regimes can be explained in conjunction with the LEED analysis (see Figure 4.3). In regime I, the observed tensile stress is ascribed to the dominant effect of a surface stress change of Ag(001). The LEED pattern at the submonolayer coverage ($t_F = 0.8$ ML) reveals a two domain (2×1) structure, as shown in Figure 4.3(b).

With increasing coverage we observe compressive stress, where MEED intensity oscillations are periodic and intense. At the end of regime II the stress change is of -6.0 N/m. This stress is ascribed to misfit stress. The periodic oscillations of the MEED intensity signify layer-by-layer growth. The MEED intensity oscillations are periodic in the thickness range of 2 to 11 ML, however, the intensity of oscillations decreases after 5 ML. This might indicate an increasing roughness of the film. Figure 4.3 (c) shows a (1×1) LEED pattern at 4 ML, which is similar to that of the clean Ag(001) surface as shown in Figure 4.3 (a). The measured stress in this regime is in quantitative agreement with the

lattice misfit stress calculated by linear elasticity theory, as will be discussed in chapter 5 (Section 5.1).

At larger film thickness ($t_F > 5$, to 20 ML), the stress change is almost constant and later around 11 ML, it starts to decrease where MEED intensity oscillations die off. The LEED pattern at 10 ML taken from as deposited NiO, shows that diffraction spots have a streaky intensity distribution along $\langle 100 \rangle$ (see Figure 4.3 (d)). With increasing thickness of NiO the streaky spots subsequently transform into broad spots (see Figure 4.3 (e)) of high intensity for the (1×1) structure. This indicates the formation of misfit dislocations in regime III, as will be discussed in Section 5.1.

In order to get a deeper insight into the structure, the LEED patterns are analysed to extract the in-plane atomic distances of the film, as described in Section 3.1. The result is plotted in Figure 4.4 as a function of the thickness

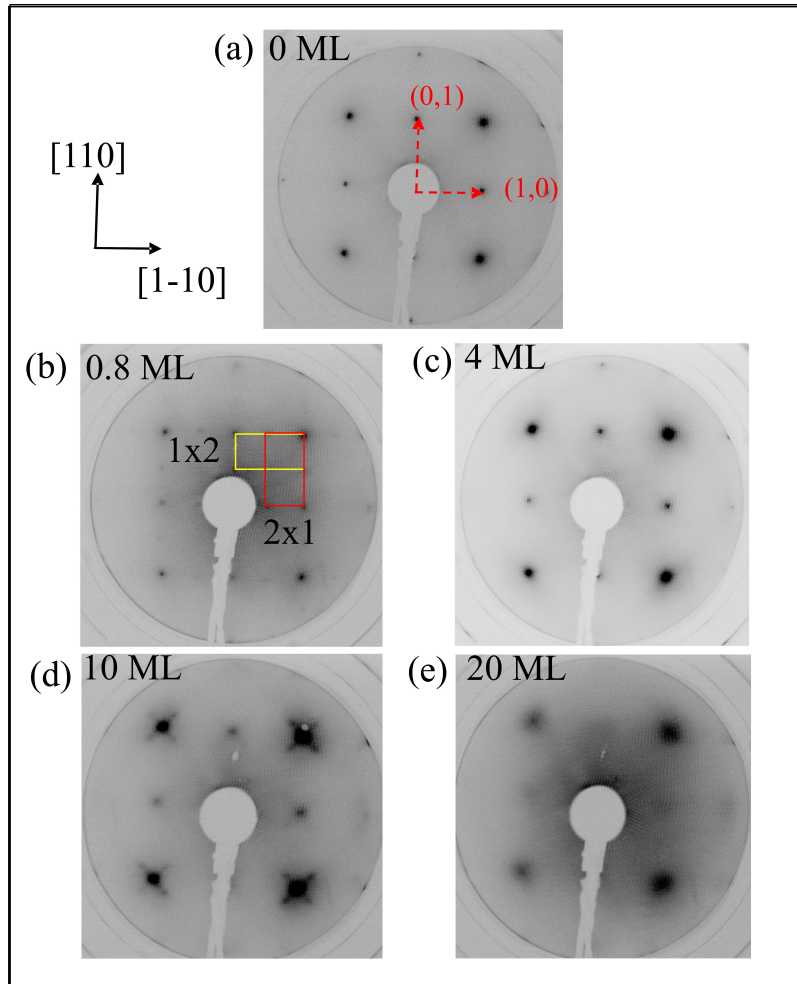


Figure 4.3: LEED patterns at different thicknesses of NiO film on Ag (001) at 300 K; electron energy 144 eV.

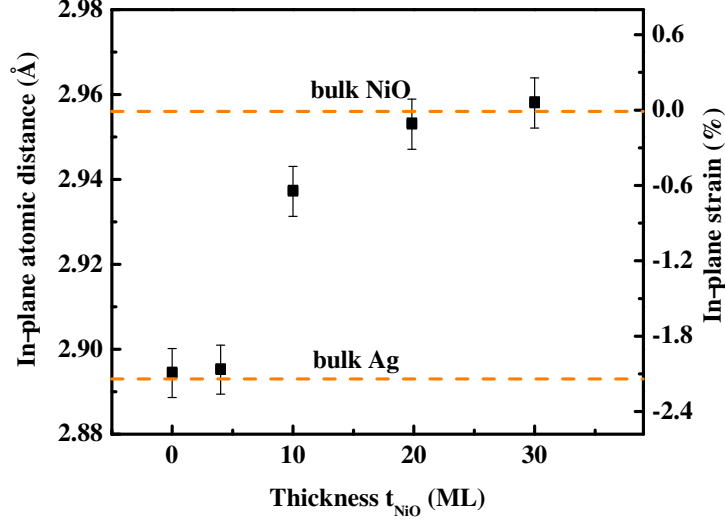


Figure 4.4: In-plane atomic distances as a function of NiO film thickness, as extracted from LEED. The corresponding bulk values for NiO and Ag are indicated by the dashed, horizontal lines. The error bar for the thickness is negligible, as *in-situ* MEED oscillations provide an excellent reference, see Fig. 4.2.

of NiO film. The plot shows that these values are the same as for bulk Ag ($a/\sqrt{2}=2.88$ Å) up to 5 ML within the error margin of ± 0.1 Å. Above 5 ML, the values approach to the bulk value of NiO ($a/\sqrt{2}=2.95$ Å). The plot indicates a complete strain relaxation in the 20 ML NiO film. However, the analysis of the vertical layer spacing in Figure 4.5 questions this strong conclusion. This is discussed in more details in connection with the stress results in Section 5.1.

As described before, LEED I(V) curves can be used to extract the average vertical interlayer spacing within a simple kinematic analysis for the (0,0) spot intensity profile. Figure 4.5 shows the interlayer spacing of NiO layers on Ag(001) as a function of the thickness. The plot reveals that the interlayer spacing for all the thicknesses is ≈ 2.13 Å. However, at submonolayer coverage the value is very similar to that of bulk Ag(001) ($d_{\text{bulk-Ag}(001)}=2.045$ Å). An example of the LEED I(V) and E vs n^2 analysis, see section 3.1, is illustrated in Figure 4. for a 20 ML NiO film on Ag(001). A substantial outward relaxation, as compared to the respective bulk value of NiO is observed. It has been observed from our stress measurement that the NiO film is compressed in the plane. Thus, an out-of-plane layer spacing is quantitatively expanded² [28]. The in-plane registry of the NiO atoms with the substrate is sustained only

²For pseudomorphic growth, it is assumed that the atoms are free to move along the normal of the film plane to minimize the elastic energy by striking for a vanishing stress $\tau_z = \frac{\partial f_{el}}{\partial \epsilon_{33}} = 0$, as discussed in chapter 5.

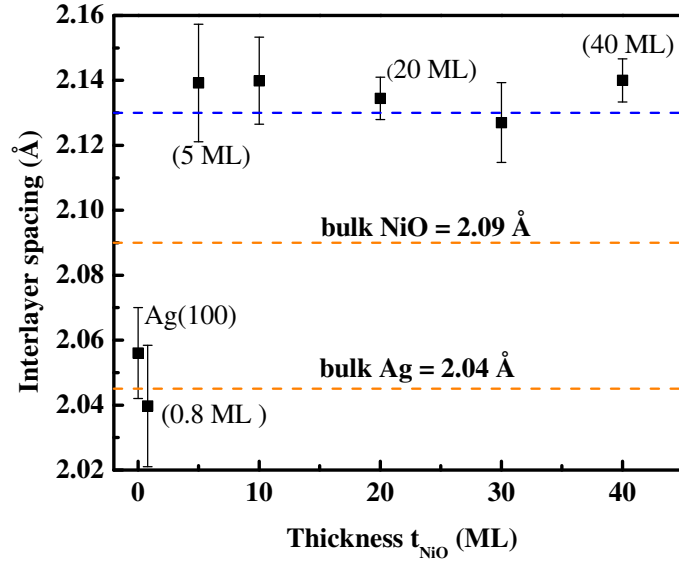


Figure 4.5: Interlayer distance as a function of NiO film thickness obtained from LEED-I (V) of the (00) spot intensity. Calculated lattice spacing of elastically strained fcc-NiO (2.13 Å) is indicated by the horizontal blue dashed line. The corresponding bulk values for NiO and Ag are indicated by the dashed, horizontal lines.

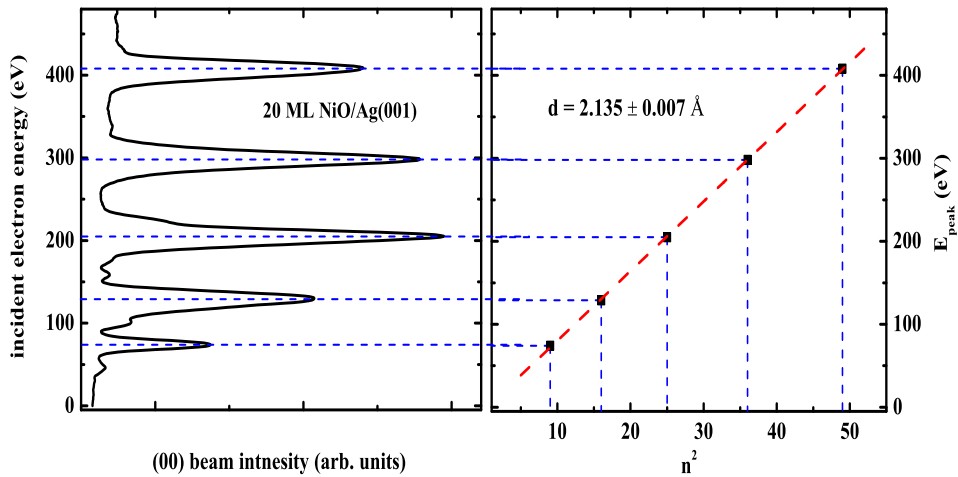


Figure 4.6: LEED I(V) of 20 ML NiO/Ag(001) (left) and corresponding E vs n^2 (right) plot.

up to 5 ML based on stress and LEED results. However, the interlayer spacing above 5 ML film is showing an expansion. This result comes as a surprise since one would expect that after pseudomorphic growth the interlayer spacing of NiO should approach towards its equilibrium value of 2.09 Å. But such a trend is not observed. These LEED results are particularly interesting as they suggest a residual vertical strain in NiO, where stress results indicate in-plane stress relaxation. This aspect is further discussed in chapter 5. These results are discussed in view of a recent SXRD analysis [88].

4.1.3 Stress and structure of CoO on Ag(001)

CoO is an oxidic system, with a rocksalt structure and a lattice constant of 4.26 Å [67]. The lattice mismatch with Ag is $\eta = \frac{a_{Ag} - a_{CoO}}{a_{CoO}} = -3.99\%$. CoO is formed by deposition of Co on Ag(001) at 450 K in an O_2 partial pressure of 2×10^{-7} mbar. Stress is measured during formation of CoO on Ag(001) with a growth rate of 67 seconds per ML. Here, the thickness of CoO is calibrated by a quartz crystal microbalance. Corresponding measurements have been also performed for NiO, where MEED gives an independent calibration. From this we conclude that the quartz crystal microbalance results could be reliable to calibrate in the absence of MEED intensity oscillations.

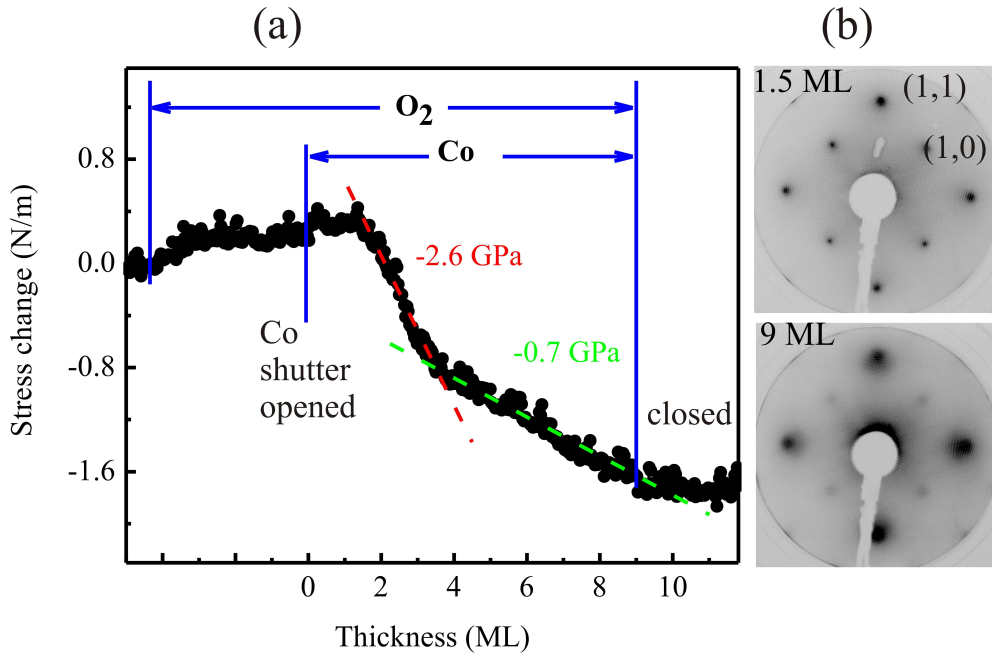


Figure 4.7: (a) Measured stress change during Co deposition on Ag (001) in an oxygen partial pressure of 2×10^{-7} mbar at 450 K. The compressive stress change is observed until the end of deposition of CoO at 9 ML. The dashed lines indicate the slopes of the stress curve. (b) The LEED images are taken after mild annealing of 10 minutes after the deposition at 450 K; electron energy 120 eV.

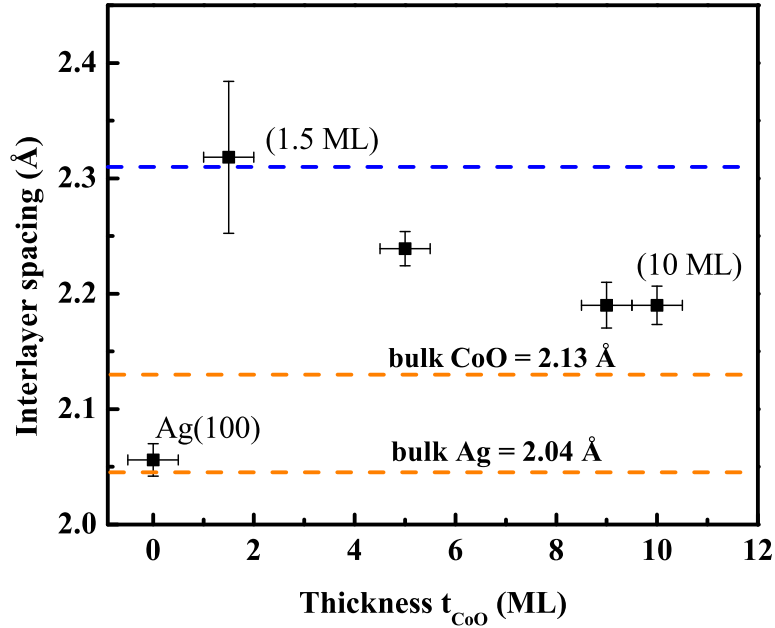


Figure 4.8: Interlayer spacing as a function of CoO film thickness on Ag(001). The corresponding bulk values for CoO and Ag have been indicated by the dashed, horizontal dashed lines. Calculated lattice spacing of elastically strained fcc-CoO (2.31 Å) is indicated by the horizontal blue dashed line.

Figure 4.7(a) shows the measured stress curve during the growth of CoO on Ag(001) as a function of film thickness. The oxygen valve is opened prior to the starting of Co deposition, and it is kept open until the end of deposition. As the shutter of the Co evaporator is opened, we find an almost stress free growth until around 1.5 ML of CoO. This stress free growth is ascribed to the formation of the CoO-Ag interface. Continued growth of CoO leads to a compressive stress with a constant slope of -2.6 GPa up to around 4 ML. The observed stress value is much lower than the expected misfit stress of -9.8 GPa. A kink appears around 4 ML, the stress is further relaxed and the slope of the curve significantly decreases to -0.7 GPa.

A compressive stress change is observed from 1.5 ML to the end of deposition around 9 ML of CoO with two distinct slopes. There is no striking structural change revealed in our qualitative LEED analysis. The LEED patterns for 1.5 and 9 ML are shown in Figure 4.7(b). These show (1×1) patterns similar to the Ag(001) substrate, except for an enhanced broadness of the spots for thicker films. LEED I(V) curves are also analysed to elucidate the interlayer spacing of the CoO film. Figure 4.8 shows the interlayer spacing of CoO on Ag(001) at different film thicknesses. The measured data suggest that for lower thickness the interlayer spacing is close to the calculated elastically strained value (calculated from in-plane strain, as outlined in chapter 5.). An example of the LEED I(V) and E vs n^2 analysis for 1.5 ML CoO/Ag(001) is illustrated

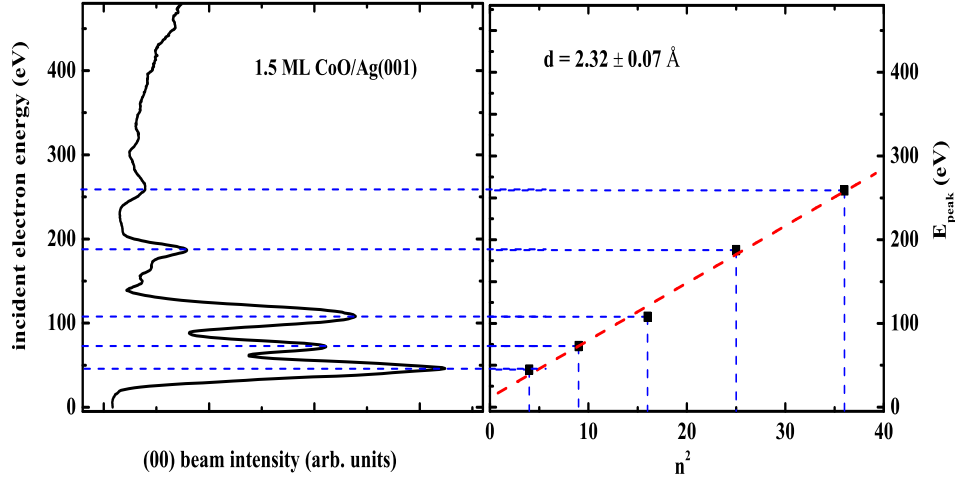


Figure 4.9: LEED I(V) of 1.5 ML CoO/Ag(001) (left), and the corresponding E vs n^2 plot (right).

in Figure 4.9. That gives interlayer distance of 2.32 \AA . While for larger thickness (see Figure 4.8, the last two data points) the values are close to the bulk ($d_{\text{bulk-CoO}}=2.13 \text{ \AA}$). The stress results of CoO on Ag(001) do not seem to show any coherent connection with the LEED measurements. A detailed discussion of this issue is provided in section 5.1.

4.2 Stress and magnetic properties of Fe monolayers on NiO and CoO on Ag(001)

To study the impact of an oxide interlayers on the magnetism of Fe monolayers, we deposit Fe layers on NiO and CoO at 300 K. Stress is measured during growth of Fe on 20 ML NiO and on 10 ML NiO on Ag(001). Magnetization hysteresis loop measurements, are performed at room temperature and at variable temperatures after deposition of Fe. The magnetoelastic (ME) coupling coefficient B_2 is measured for Fe/10 ML NiO/Ag(001) and for Fe/Ag(001) by ME stress measurements. The most striking result of this investigation is that B_2 of 6 ML Fe/10 ML NiO/Ag(001) is almost an order of magnitude larger and opposite in sign as compared to 6 ML Fe/Ag(001). The effect of CoO layers on the coercivity of Fe film is investigated.

4.2.1 Stress and structure of Fe monolayers on NiO

Film stress is measured during deposition of Fe on NiO on Ag(001) at room temperature. Here, the NiO film has been prepared as explained in the preceding section. The partial pressure during deposition of Fe was below 4×10^{-10} mbar. The lattice mismatch between bcc Fe ($a_{Fe} = 2.866 \text{ \AA}$ [67]) and fcc NiO is $\eta = \frac{a_{NiO}/\sqrt{2} - a_{Fe}}{a_{Fe}} = +3.04 \%$. Our data suggest that Fe grows epitaxially on NiO with a bcc structure.

The measured stress during deposition of Fe on NiO/Ag(001) at 300 K as a function of Fe thickness is shown in Figure 4.10 (a). The Fe growth rate is calibrated by a quartz crystal microbalance. A tensile stress (positive signal) is observed which increases linearly in magnitude with Fe thickness until the end of deposition at around 7 ML. The tensile stress indicates the tendency of the film to contract in-plane, which agrees with the expectation of an epitaxial misfit. The stress curve shows a constant slope of +5.7 GPa up to 5 ML, it is slightly reduced to +4.4 GPa for thicker films. The stress below 5 ML can be quantitatively ascribed to the epitaxial misfit, as will be discussed in chapter 5. The LEED patterns after and before deposition of the Fe film on 20 ML NiO/Ag(001) are shown in Figure 4.10 (b). These show a (1×1) structure, the spots are a little blurred and less intense after deposition of Fe, which implies a rougher surface. The reciprocal unit cell is indicated on each LEED picture, it does not change its size upon Fe growth.

4.2.2 Magnetism and magnetoelastic coupling of Fe monolayers

Magnetic hysteresis loops of Fe monolayers deposited on NiO and on annealed CoO monolayers on Ag(001) are measured by MOKE. MOKE is performed in all three geometries: longitudinal and transversal geometries are used to detect two in-plane and polar for out-of-plane magnetization responses. The Fe film shows in-plane magnetic hysteresis loops on both substrates. Before deposition of Fe, MOKE measurements of the oxide films are performed, and a constant MOKE signal with the applied magnetic field in all orientations is observed. This indicates that the magnetic hysteresis loop needs to be ascribed to the Fe film on oxides, but not to the oxide film alone. This qualitatively confirms that an oxide has formed, with no Ni or Co atomic residuals.

I observe hysteresis MOKE curves for 6 ML Fe film on 20 ML NiO/Ag(001). They reveal an in-plane magnetization, no polar (or out-of-plane) loop is observed. Therefore, I show here only longitudinal MOKE. In the longitudinal mode, the external magnetic field is applied along NiO $[1\bar{1}0]$, which is parallel to Fe $[010]$, the easy magnetization axis of bcc Fe. Figure 4.11 shows the in-plane hysteresis loops of 6 ML Fe/20 ML NiO/Ag(001) measured at different temper-

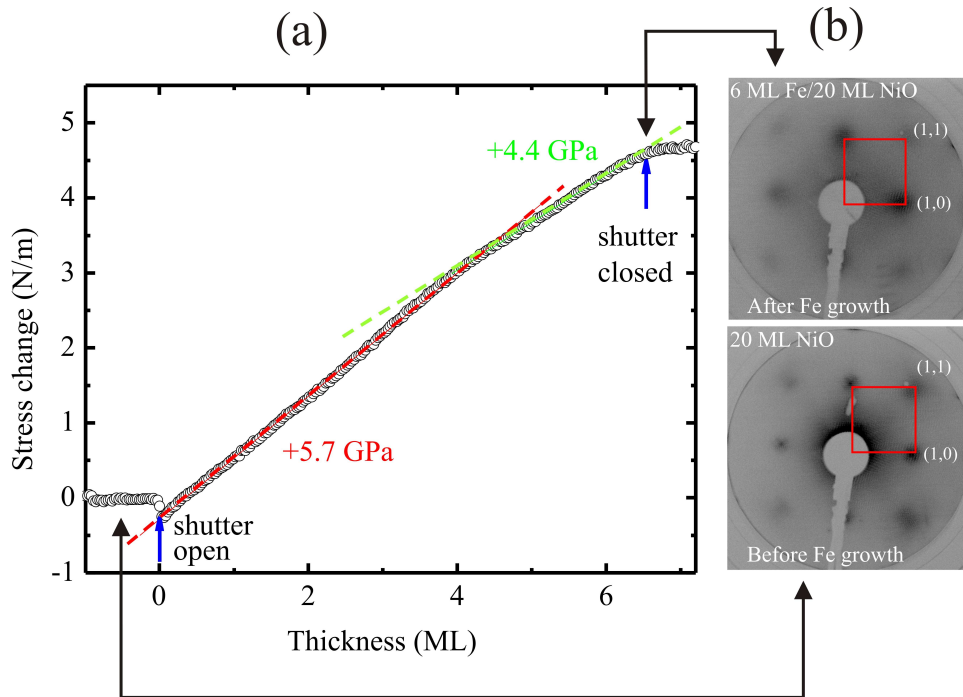


Figure 4.10: (a) Measured stress change during deposition of Fe onto 20 ML NiO/Ag(001). The stress curve indicates a stress of +5.7 GPa in the first 4 ML of Fe deposition. The dashed lines indicates the slope of the stress curve. (b) LEED images before and after Fe growth; electron energy 120 eV.

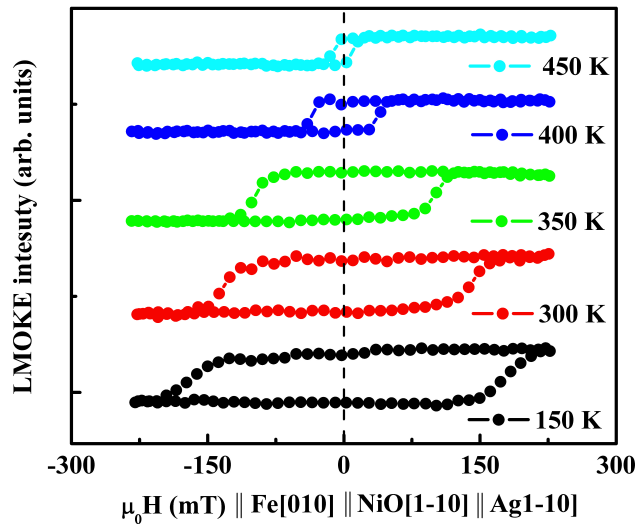


Figure 4.11: Longitudinal MOKE of 6 ML Fe/20 ML NiO/Ag(001) at different temperatures. The curves are all with the same vertical scale, but have been shifted vertically for clarity.

atures. The coercive field (H_c) of the Fe film at room temperature is around 141 mT, which is remarkably large. The large value of coercivity at 300 K is ascribed to the coupling of Fe to NiO, as will be discussed in further detail in chapter 5. The coercivity decreases with increasing temperature. At 450 K it is significantly reduced to 15 mT. At the same time, the magnitude of the loops decreases with increasing temperature. This is an indication of the Curie temperature of 6 ML Fe film, as discussed in chapter 5. The film does not show any intermixing or alloying even after annealing up to 480 K, as checked by Auger electron spectroscopy and MOKE. The curves are reversible with temperature. The room temperature hysteresis loop of the sample is reproducible after the annealing up to 480 K and cooling down back to 300 K. However, annealing of the sample above 500 K leads drastic changes in Auger electron spectrum as well as in the magnetic hysteresis, and the reversibility is gone.

The measured hysteresis loop is symmetric around the zero field axis that means no exchange bias is observed for this sample. Also, field cooling from above T_N to 300 K, in presence of magnetic field of 200 mT did not change this result, which is further discussed in chapter 5.

The increase of the coercivity is investigated also as a function of the thickness of NiO at 300 K, as shown in Figure 4.12(a). The plot shows that the coercive field of 6 ML Fe starts to increase around a NiO thickness of 8 ML. It reaches a maximum around 141 mT at 20 ML NiO. In Figure 4.12(b), the coercive field of 6 ML Fe/20 ML NiO/Ag(001) is plotted as a function of temperature. The value of the coercive field is extracted from the hysteresis loops shown in Figure 4.11. The plot shows that H_c decreases as the temperature increases. This is ascribed to the Néel temperature of NiO. Physically it means that the interface coupling between Fe and NiO decreases gradually with the temperature, and around or above 480 K the NiO film becomes paramagnetic. T_N of bulk NiO is 523 K [89]. Therefore, at 480 K the H_c is similar to the H_c of 6 ML Fe/Ag(001). A detailed analysis is discussed in Section 5.2.

Figure 4.13 shows longitudinal MOKE hysteresis loops of 6 ML Fe/20 ML CoO/Ag(001) measured at different temperatures. The CoO film is grown on differently cut Ag(001) crystal, see Fig. 3.6 (b). At 300 K the hysteresis loop of the sample is similar to that of the 6 ML Fe/Ag(001). It appears that CoO has no influence on the Fe film at 300 K. The coercivity increases with decreasing temperature. At 230 K the coercivity of the 6 ML Fe film on 20 ML CoO/Ag(001) is enormously large ($H_c = 225$ mT). The onset of coercivity enhancement indicates the transition of the CoO film from a paramagnetic to an antiferromagnetic state with lowering the temperature below 300 K, as will be discussed in chapter 5. For bulk CoO T_N is 291 K [89].

The coercivity (H_c) of the sample at different temperatures are plotted in Figure 4.14. In the figure, H_c of 6 ML Fe/10 ML CoO/Ag(001) is also plotted. The plot shows the same trend of an increase of H_c with decreasing temperature for both samples. The extrapolation of the data points with a linear regression

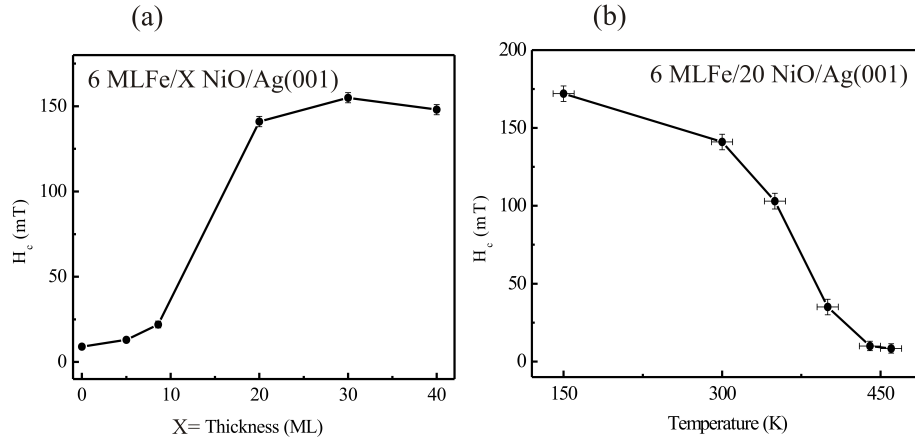


Figure 4.12: H_c of 6 ML Fe on NiO/Ag(001) as a function of NiO film thickness (a) and temperature (b).

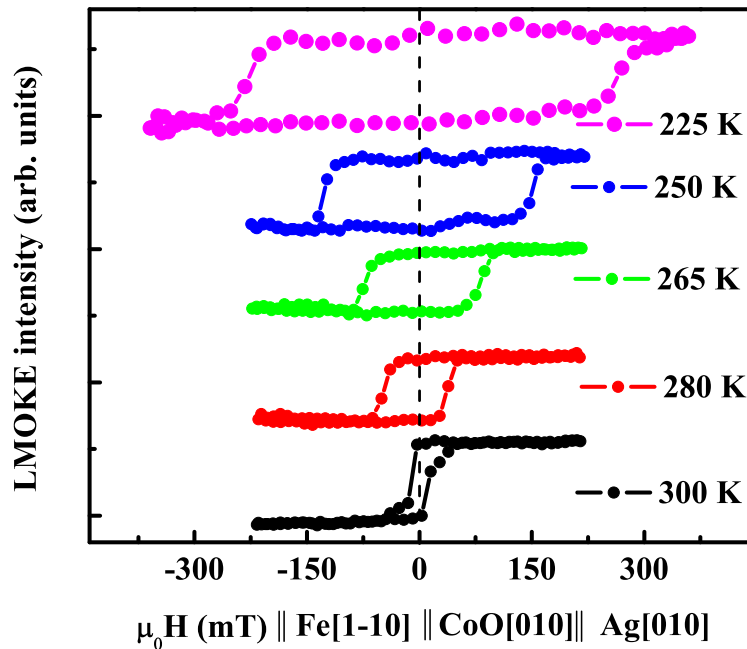


Figure 4.13: Longitudinal MOKE of 6 ML Fe/20 ML CoO/Ag(001) at different temperatures. The curves are all with the same vertical scale, but have been shifted vertically for clarity.

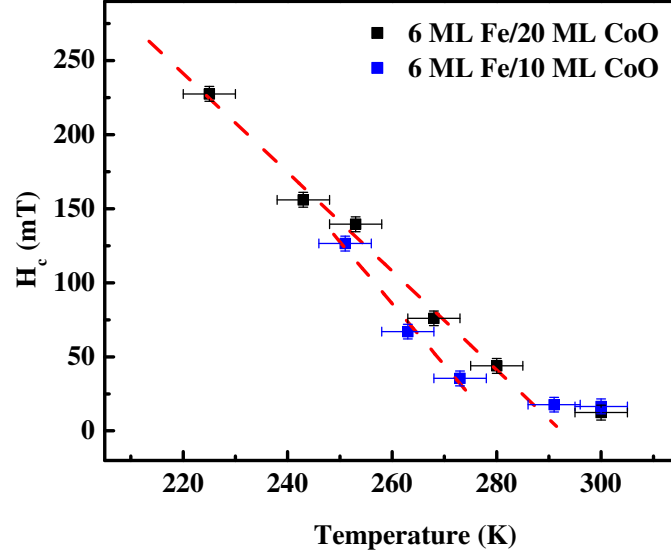


Figure 4.14: Coercive field (H_c) as a function of temperature for 6 ML Fe/ 20 ML CoO and 6 ML Fe/10 ML CoO on Ag(001).

suggests a Néel temperature of the corresponding CoO film. In case of 20 ML CoO, T_N is estimated as 288 K, very close to the bulk value of 291 K [89], whereas for 10 ML it is around 276 K. A detailed discussion of this aspect follows in chapter 5.

Magnetoelastic coupling of Fe on 10 ML NiO/Ag(001)

The magnetoelastic stress measurements are performed on a differently cut Ag(001), where the long and short edges of the crystal are parallel to Ag[100] and Ag[010], respectively, see Fig. 3.6 (b). The initial crystal was damaged by the repeated heating process. Thus, the horizontal and vertical directions in the crystal frame are rotated by 45° with respect to fcc NiO. As the Fe film does not show a pronounced in-plane anisotropy, saturation along the in-plane directions can be achieved, as indicated by the MOKE curves. Experiments on a differently oriented crystal are foreseen and will be performed. The magnetoelastic coupling coefficient of Fe films on 10 ML NiO/Ag(001) is obtained by performing magnetoelastic (ME) stress measurements upon a reorientation of the film magnetization along two orthogonal directions within the film plane [28, 90] (*e.g.* from $M[110]$ to $M[\bar{1}\bar{1}0]$), as explained in Section 3.2. The Fe film grows epitaxially on Ag (001), with a unit cell of bcc Fe which is 45° rotated. Epitaxial orientation for the system: Fe(001)-[110] \parallel NiO [100] \parallel Ag(001)-[100] and Fe(001)-[$\bar{1}\bar{1}0$] \parallel NiO [010] \parallel Ag(001)-[010]. The Fe film shows an in-plane easy axis of magnetization. This was manifested in our experimental results, as shown above.

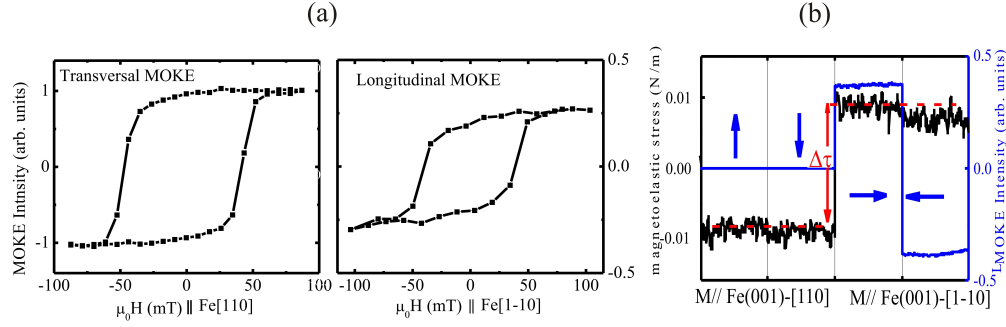


Figure 4.15: (a) Transversal and longitudinal magnetic hysteresis loops of 6 ML Fe/10 ML NiO/Ag(001), coercive field $H_c=40$ mT at 300 K. (b) Magnetoelastic stress change (black curve) for 6 ML Fe/10 ML NiO/Ag(001) upon in-plane magnetization reorientation, as monitored by longitudinal MOKE intensity (blue curve). The magnetoelastic stress change ($\Delta\tau$) of -0.017 ± 0.0014 N/m results in $B_2 = -19.6 \pm 1.6$ MJ/m³. All measurements are performed at 300 K.

Figure 4.15 (a) shows magnetic hysteresis loops of 6 ML Fe grown on 10 ML NiO/Ag(001) measured in the transversal and longitudinal MOKE geometries. The MOKE loops exhibit a significantly enhanced coercive field also with reference to the results presented above. MOKE indicates that the Fe film can be magnetized to saturation in these two perpendicular directions. The ME stress change of the system is shown in Figure 4.15 (b). A magnetoelastic stress change of $\Delta\tau = -0.017 \pm 0.0014$ N/m is measured upon a re-orientation of the magnetization directions. It corresponds to $B_2 = -19.6 \pm 1.6$ MJ/m³, which is opposite in sign to the bulk value, and is a factor of 2.5 larger in magnitude. To see the effect of NiO on Fe for B_2 , it is measured for various thicknesses of NiO for a constant thickness of Fe. The values of B_2 are plotted in Figure 4.16 (a) as a function of the NiO film thickness. To demonstrate the dependence of B_2 on the film strain, the in-plane film strain ($\epsilon_{//}$) obtained from stress measurement is set as x-axis in Figure 4.16 (b). To appreciate the magnetic properties of Fe/NiO/Ag(001), we also present the corresponding measurements for Fe/Ag(001).

MOKE and magnetoelastic coupling of Fe/Ag(001)

For comparison, the ME stress measurements are also performed for 6 ML Fe on Ag(001). MOKE and ME stress change are shown in Figure 4.17 (a) and (b), respectively. The measured ME stress change upon a re-orientation of magnetization directions of 6 ML Fe/Ag(001) is $\Delta\tau = +0.002 \pm 0.0006$ N/m which corresponds to $B_2 = +2 \pm 0.6$ MJ/m³. This value is factor four smaller than the respective bulk value of $B_2^{bulk} = +7.83$ MJ/m³ [28].

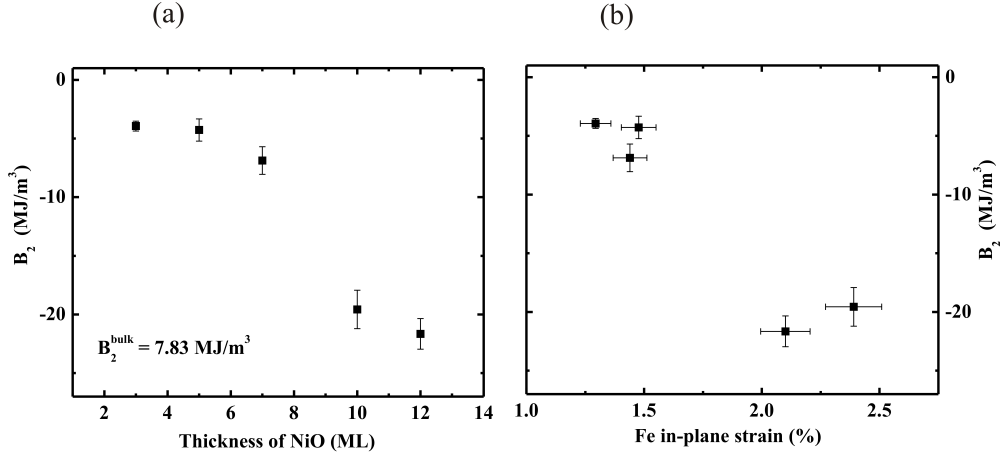


Figure 4.16: (a) B_2 for 6 ML Fe deposited on top of NiO/Ag(001) is demonstrated as a function of thickness of NiO. (b) Strain dependence of B_2 . For comparison: B_2 for 6 ML Fe/Ag(001) = +2 MJ/m³, bulk Fe +7.8 MJ/m³.

B_2 of 6 ML Fe/10 ML NiO/Ag(001) is almost an order of magnitude larger and opposite in sign as compared to the 6 ML Fe/Ag(001). It has been known from previous studies [21, 28, 91] that B_i of thin magnetic films deviates from their respective bulk values. Film strain is reported as a decisive factor for the deviation [21, 23, 26].

The comparison of measured ME coupling coefficients of these two systems reveal for the first time that B_2 of Fe can be changed dramatically by the insertion of an oxide layer. B_2 of Fe(001) monolayers on Ag(001) is explored at different thicknesses of Fe, the data points are plotted in Figure 4.18 (a). The film strain for different thicknesses are obtained from stress measurement as discussed in chapter 5. B_2 as a function of in-plane strain is shown in Figure 4.18 (b). The values of B_2 for all the investigated thicknesses of the Fe film on Ag(001) are significantly different from the bulk value of +7.83 MJ/m³.

In order to explore a possible interface effect on B_2 of Fe film, we have measured B_2 for Fe on oxygen exposed Ag(001). Some of the data points are plotted in Figure 4.18. The Figure indicates that B_2 of the Fe film does not change due to oxygen in between Fe and Ag(001). Both plots of B_2 do not show any clear thickness nor strain dependence. This issue has not been explored in previous studies, and it is discussed in detail in chapter 5. Clearly, the experimental data base needs to be enhanced and further measurements are called for to address this issue more rigorously.

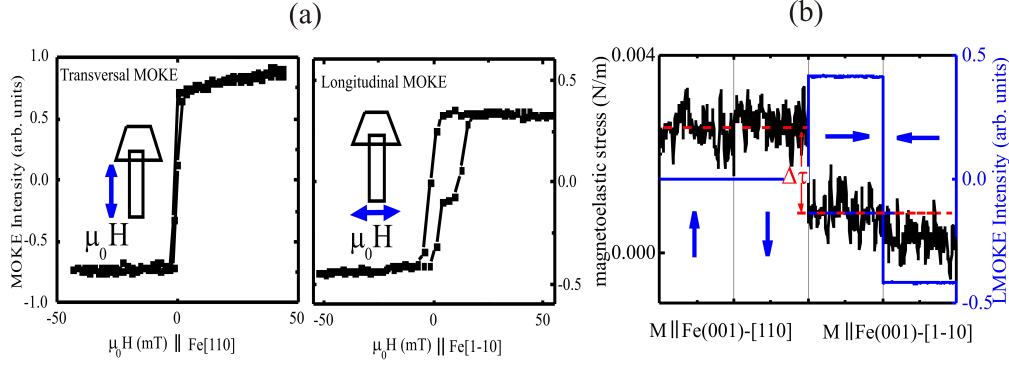


Figure 4.17: (a) Transversal and longitudinal MOKE of 6 ML Fe/Ag (001), along the orthogonal directions in the plane. The origin of the asymmetric longitudinal MOKE loop is not clear yet. (b) Simultaneously, measured ME stress change (black) on the left scale and longitudinal MOKE intensity (blue) on the right scale. The magnetization is first aligned along the length of the crystal ([110] of bcc-Fe(001)), pointing up and down and then we switch the field direction along the width of the crystal, pointing to the right and the left ([1 $\bar{1}$ 0] of bcc-Fe(001)), shown with blue arrows. The magnetoelastic stress change ($\Delta\tau$) of $+0.002 \pm 0.0006$ N/m results in $B_2 = +2 \pm 0.6$ MJ/m³.

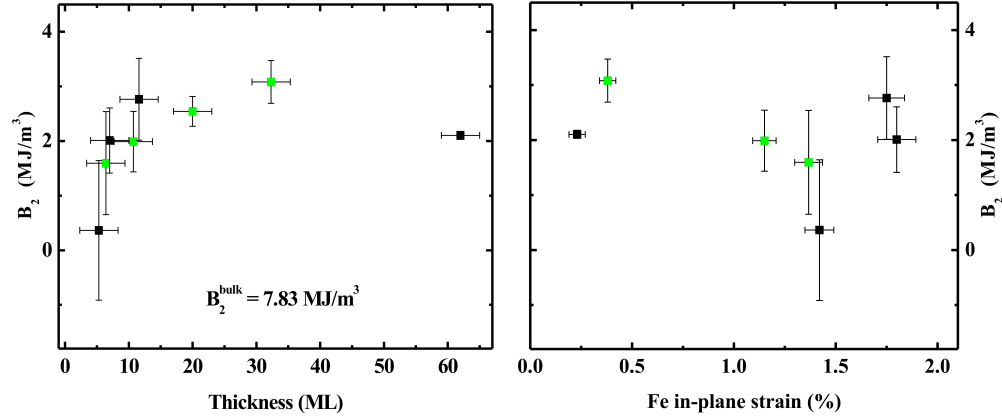


Figure 4.18: B_2 of different Fe film thickness on Ag(001) plotted vs film thickness (a) and in-plane strain (b). The film strain is obtained from the stress measurement performed during growth of the Fe film. The data points for Fe(001) film on oxygen exposed Ag(001) are shown in the green. The data points do not show any clear dependence on the thickness nor on the in-plane strain of the Fe film. The $B_2 = +2 \pm 0.6$ MJ/m³ of 6 ML Fe/Ag(001) is less than the bulk Fe, $B_2^{bulk} = +7.83$ MJ/m³.

4.3 Stress and magnetism of metallic monolayers on Pt(111)

Here I report stress and LEED measurements on Co/Pt(111) and Ag/Pt(111). Section 4.3.2 presents results from MOKE on the spin reorientation transition of Co monolayers on Pt(111).

4.3.1 Stress and structure of Co and Ag monolayers on Pt(111)

Stress induced by Co on Pt(111)

The stress change ($\Delta\tau = \Delta(\tau_{FF})$) during Co film deposition is measured by the optical beam deflection technique, as explained in section 3.2. The lattice mismatch between Co and Pt is $\eta = \frac{a_{Pt} - a_{Co}}{a_{Co}} = +10.4\%$ with $a_{fcc Co} = 3.55 \text{ \AA}$, $a_{fcc Pt} = 3.92 \text{ \AA}$ [67]. Figure 4.19 (A) presents the stress change during deposition of the Co film on Pt(111) at 300 K as a function of Co film thickness. Thickness is calibrated by a quartz crystal microbalance. A tensile stress change is observed. The curve shows a non-monotonic variation from 0–2 ML (indicated as blue rectangular shaded area, see figure 4.19 (A)), above 2 ML there is constant slope of +3.5 GPa. This slope is ascribed to a constantly strained film in the thickness range of 2–5 ML of the Co film [92], as discussed in Section 5.3.

Figure 4.19 (B) shows LEED images of clean Pt(111) and of Co monolayers on Pt(111) taken at 300 K. It shows a (1×1) pattern for 0.8 ML. In the thickness range 2–5 ML, Moiré patterns are visible. In these patterns, each integer spot is surrounded by extra spots (a magnified view is displayed on top of the respective LEED pictures, see figure 4.19 (B): (c) and (d)). A quantitative analysis of the diffraction images reveals an average Co film strain of +0.8 %, significantly lower than the misfit strain of +10.4 %. This finding is discussed in Section 5.3.

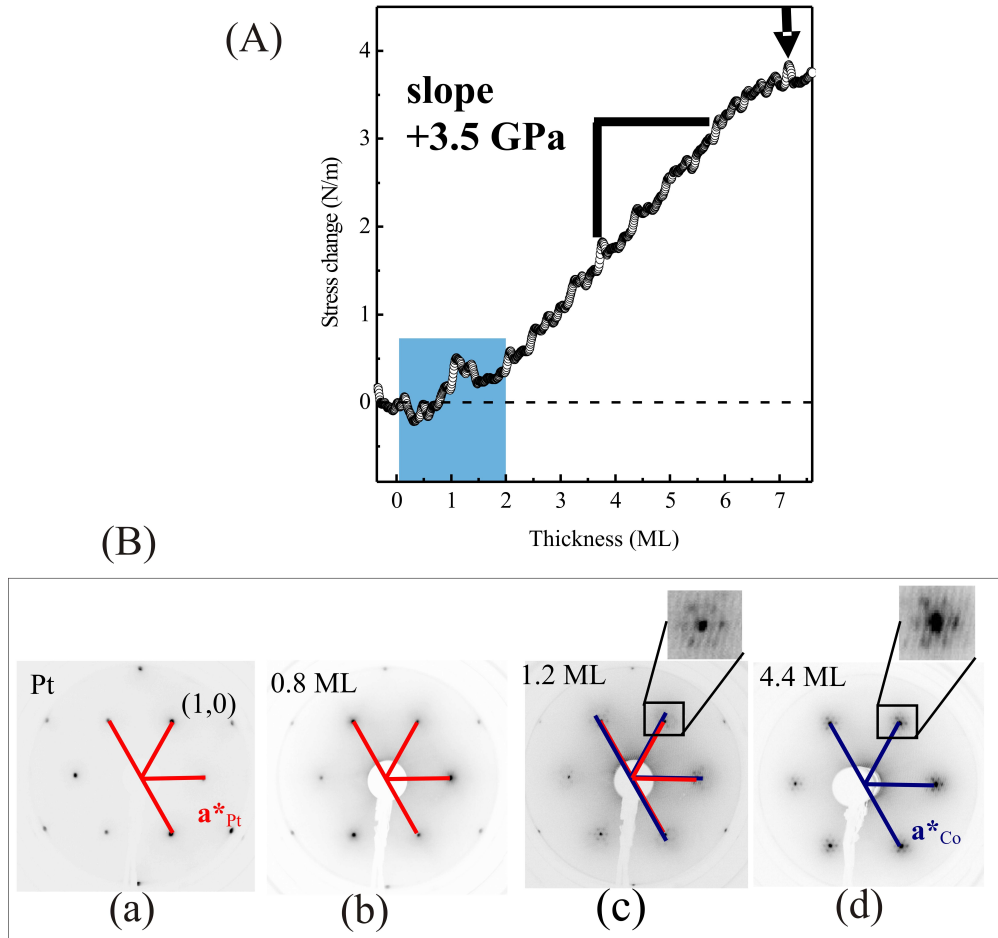


Figure 4.19: (A) Stress change during deposition of Co on Pt(111) at 300 K. Note that for a thickness below 2 ML a non-monotonic variation of stress with thickness is observed (blue regime). In thicker films, a constant film stress of +3.5 GPa is observed. (B) LEED patterns at different coverages of Co at 300 K on Pt(111). Moiré pattern develops above 1 ML. Enlarged image of an integer spot (marked as a square) is shown on top of the corresponding LEED pattern. LEED patterns; electron energy 144 eV.

To explore the possible reasons for the initial non-monotonous stress regime (blue regime in figure 4.19 (A)), the Co film stress measurements were performed at different temperatures, as shown in Figure 4.20. We observe that the stress change for the initial 2 ML Co depends dramatically on temperature. The stress curves suggest that the Co-Pt interface is quite sensitive to a temperature change. However, no structural change is observed from a quantitative visual inspection of LEED. Above 2 ML the slope of the stress curve is similar within the measured temperature range. It corresponds to +3.5 GPa, which is significantly smaller than the misfit stress of +40 GPa. This indicates a strain relief of the Co film structure. This view is confirmed by the observed Moiré pattern (see Figure 4.19 (c) and (d)), as discussed in Section 5.3.

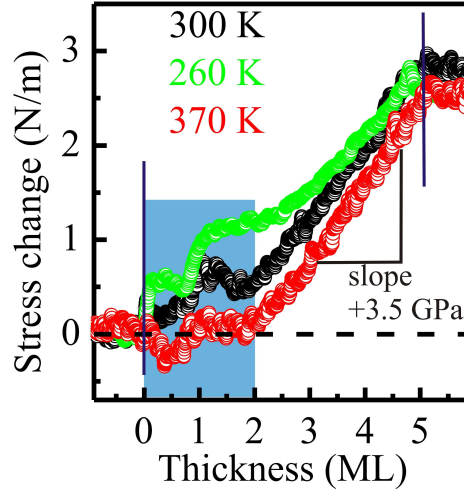


Figure 4.20: Stress measurements during deposition of 5 monolayers (ML) Co onto Pt(111) at 300 K (black curve), 260 K (green curve), and 370 K (red curve). Note that for a thickness below 2 ML a non-monotonic variation of stress with thickness is observed (blue regime), this regime is strongly depend on the deposition temperature. In thicker films, a constant film stress of +3.5 GPa is observed.

Stress induced by Ag on Pt(111)

The lattice mismatch between Ag and Pt is $\eta = \frac{a_{Pt} - a_{Ag}}{a_{Ag}} = -4.06\%$ with $a_{Ag} = 4.085 \text{ \AA}$ [67]. The thickness of the Ag is calibrated by Auger electron spectroscopy (AES). The normalized³ Auger peak intensities for Ag and Pt are plotted in Figure 4.21 as a function of Ag deposition time. The plot exhibits a variation of slope. There is a clear change of slope at a Ag coverage time around 2.2 minutes. This is ascribed to the completion of 1 ML Ag on Pt(111). This calibration serves as a reference. The stress curve during the growth of epitaxial Ag on Pt(111) at 300 K is shown in Figure 4.22. It shows a compressive stress change of -5.5 N/m at 3 ML, and then curve levels off with increasing coverage. The negative slope of the curve indicates a compressive stress of -8.9 GPa . This value is close to the calculated misfit stress. This indicates epitaxial misfit determines stress in epitaxial growth of this system rather well. This result contradicts the previous reported result from Ibach's group [93], even after their correction [94]. This discrepancy with respect to earlier work by others is discussed in Section 5.3.

To elucidate the role of possible intermixing between Ag and Pt, stress measurements at higher temperatures (HT) were also performed. One of the stress curves taken at 580 K is shown in Figure 4.22, together with a room temperature measurement. The curve shows that the stress relaxes at an earlier

³Normalization is done by taking ratio of Ag or Pt peak with a sum of Ag and Pt peak intensity.

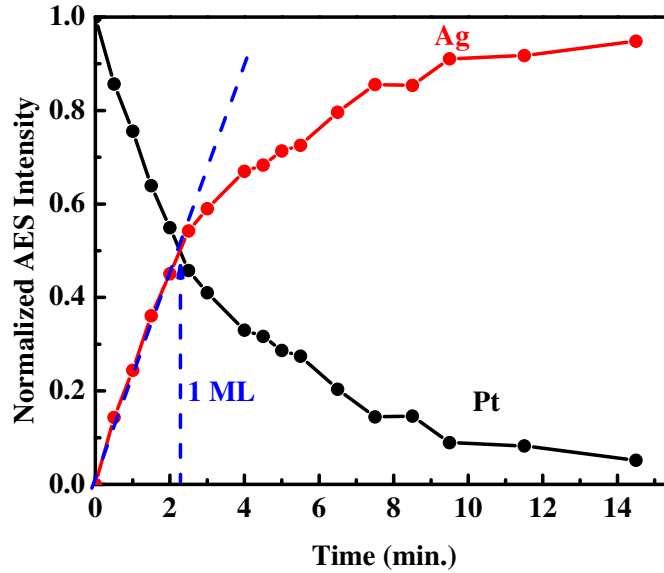


Figure 4.21: Normalized Auger peak intensity of Ag (red) and Pt (black) as a function of Ag deposition time. The blue dashed line is a guide to the eye, indicating linear increase in the intensity of Ag. The vertical, dashed line denotes the completion time for a monolayer of Ag (2.2 min. 1 ML).

coverage of Ag at 580 K as compared to the deposition at 300 K. The total stress change is reduced at HT. For example, at 3 ML of Ag the total stress change is -3.1 N/m, which is almost factor two smaller than the growth at 300 K. However, the initial linear decrease of stress is comparable at both temperatures. The corresponding LEED patterns were taken after the complete deposition of Ag, as indicated by the vertical blue lines in their respective curves. The LEED patterns show a (1×1) structure (see Figure 4.22). The average stress at 3 ML decreases with increasing the temperature at and above 580 K. At 630 K, LEED shows that the $(0,0)$ spot is surrounded by extra spots, as shown in Figure 4.23. The details are discussed in Section 5.3.

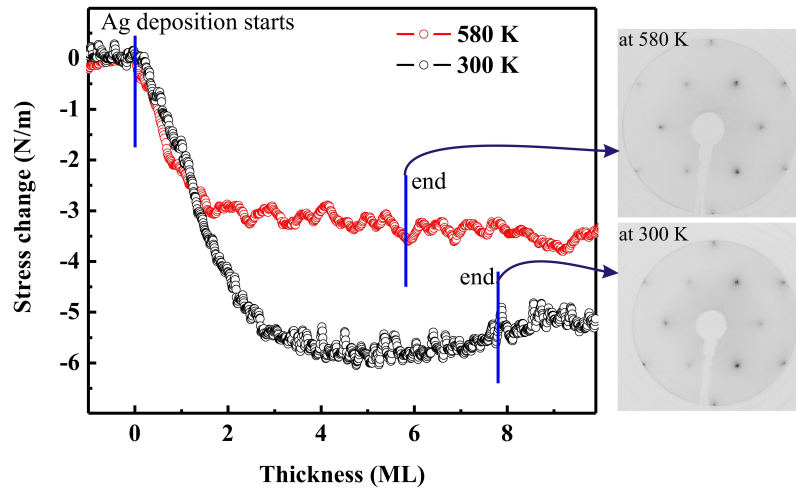


Figure 4.22: Stress change during deposition of Ag on Pt(111) at two different temperatures, 300 K (black) and 580 K (red). Blue lines indicate the end of Ag deposition. LEED pictures are taken at 144 eV.

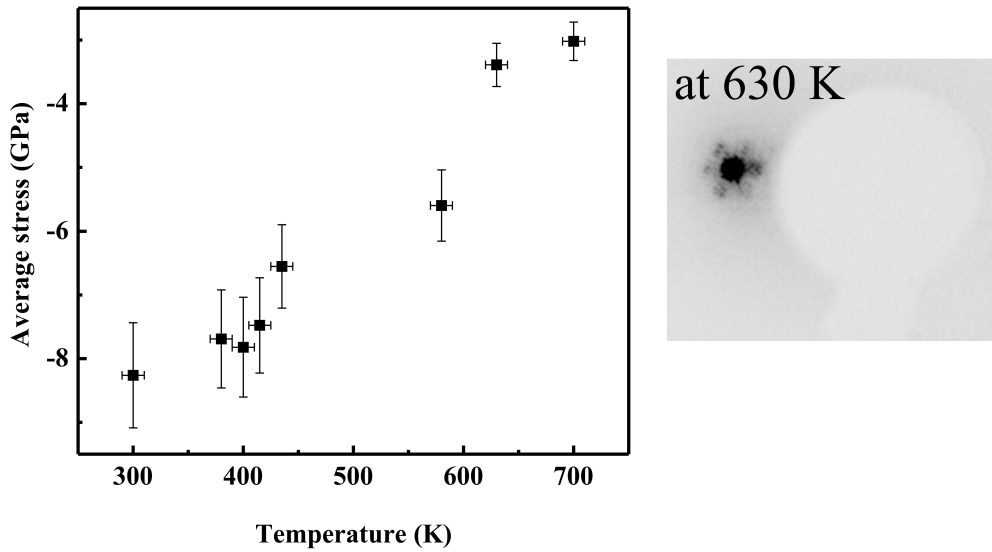


Figure 4.23: Average stress at 3 ML Ag on Pt(111) for deposition at different temperatures. The LEED image is taken after Ag deposition at 630 K on Pt(111), at 40 eV. The incident electron beam deviates from the surface normal by a small angle of 7° . The LEED image shows satellite spots around the (0,0) spot.

4.3.2 Magnetism and spin reorientation transition in Co monolayers on Pt(111)

Our results indicate that the Co film grows epitaxially on Pt(111) at 300 K. To elucidate the magnetism of Co on Pt(111), we perform MOKE measurements. For small Co coverage below 3.5 ML an easy axis of magnetization is observed in the out-of plane direction. Above 3.5 ML, an in-plane hysteresis loop is measured. The transition of an easy axis of magnetization of the Co film from out-of-plane to in-plane direction is observed around 3.5 ML.

Figure 4.24 shows MOKE hysteresis loops measured at different thicknesses of Co on Pt(111). At 5 ML Co, the polar MOKE shows flipped loops upon slight rotation of the magnet by $\pm 2^\circ$. This indicates small component of a longitudinal field. This gives rise to an apparent polar MOKE signal. The square hysteresis loop shows up for longitudinal MOKE. This indicates that the easy magnetization axis is in the plane of the film at 5 ML of Co. The Kerr intensity (twice of the remanence of the hysteresis loop) as a function of Co coverage is shown in Figure 4.25 (measured at 300 K). It shows that the polar Kerr intensity increases with thickness up to 3 ML, however, no in-plane Kerr (longitudinal MOKE) signal is observed. At 4 ML, the longitudinal Kerr signal appears and increases with a further increase of Co thickness, but no polar MOKE is detected. This indicates that the easy axis of magnetization changes from out-of-plane to in-plane. Thus, a spin reorientation transition⁴ (SRT) occurs around 3.5 ML of Co films on Pt(111), prepared at 300 K.

Our MOKE measurements reveal that the critical thickness for a SRT of Co monolayers on Pt(111) strongly depends on the Co film growth temperature. For Co deposition at 300 K, the SRT occurs at 3.5 ML, whereas at 370 K deposition it shifts to 5 ML. This issue in correlation with the stress analysis is discussed in Section 5.4.

⁴The rotation of the easy axis of magnetization is called spin-reorientation transition

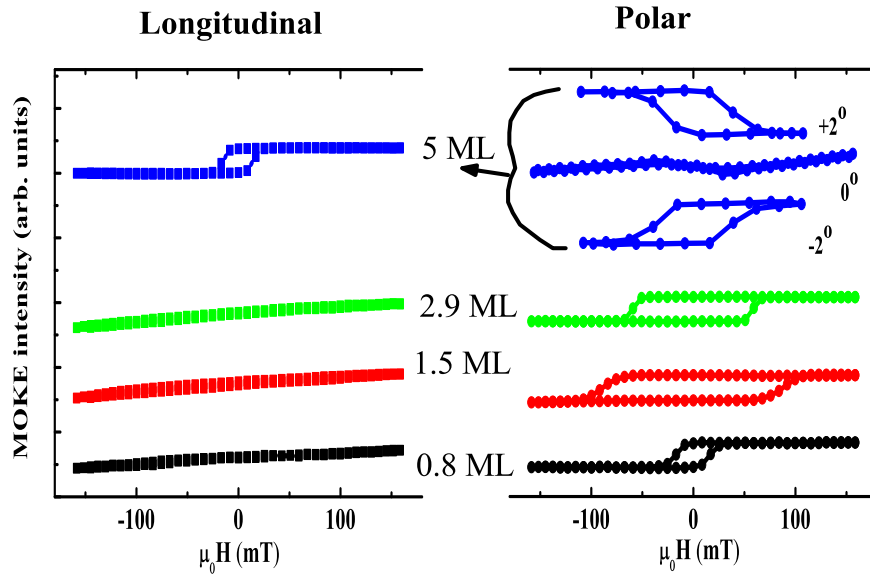


Figure 4.24: The longitudinal (left) and polar (right) Kerr hysteresis loops of Co deposited on Pt(111). All measurements were performed at 300 K.

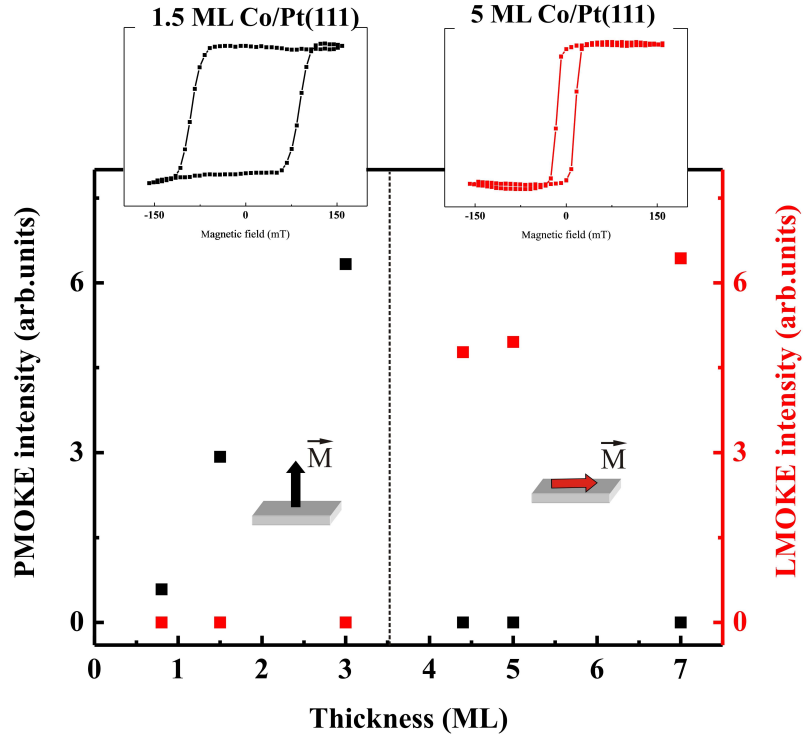


Figure 4.25: Polar (left scale) and longitudinal (right scale) MOKE intensities are plotted as a function of Co film thickness. At the thickness of 3.5 ML Co the spin reorientation transition (SRT) from out-of-plane to in-plane occurs.

Chapter 5

Discussion

This chapter presents a detailed discussion of all the experimental results presented in the preceding chapter. First, the correlation between stress, strain and structure of metallic oxides monolayers (NiO and CoO) on Ag(001) is discussed. An important result is that stress in NiO film can be described by continuum elasticity theory, whereas CoO shows a complex stress behavior. Section 5.2 discusses the effect of NiO and CoO spacer layers on the magnetism of Fe monolayers deposited on the oxide monolayers. Both NiO and CoO enhance the coercivity by a factor of 15, and NiO increases the magnetoelastic coupling of Fe.

Section 5.3 discusses stress induced by metallic films (Co and Ag) on Pt(111). In the last section of this chapter, we discuss how the spin reorientation transition (SRT) from out-of-plane to in-plane with increasing Co film thickness on Pt(111) can be tuned by modifying the growth temperature and adlayer coverage of the Co film.

5.1 The correlation between stress, strain and structure of NiO and CoO on Ag(001)

In epitaxial growth of a pseudomorphic film on a substrate, the lattice mismatch $\eta = \frac{a_{sub.} - a_{film}}{a_{film}}$ determines the strain in the film. It induces a biaxial film stress of $\tau_F = \frac{Y_F}{(1-\nu_F)}\eta$, where Y_F and ν_F are the Young modulus and Poisson ratio of the film, respectively. Values of these parameters are provided in Table 5.1.

NiO on Ag(001)

From our combined stress and MEED measurements during the deposition of NiO on Ag(001) at 300 K, we find three different stress as well as distinct growth regimes (see Fig. 5.1). This indicates a complex interface formation followed by a layer-by-layer growth of NiO. Our results suggest that the NiO film grows pseudomorphically on Ag(001) in the thickness range from 1.5 to

Table 5.1: Lattice constant a from Ref. [67], epitaxial misfit $\eta = \frac{a_{sub.} - a_{film}}{a_{film}}$ compared to Ag, elastic compliance constants s_{ij} , Young's modulus $Y_{(001)} = 1/s_{11}$, and Poisson ratio $\nu = -s_{12}/s_{11}$ of the substrate Ag and deposited film elements are tabulated for the cubic (001) orientation.

	a Å	η	s_{11} (TPa) ⁻¹	s_{12} (TPa) ⁻¹	Y (GPa)	ν
fcc Ag ^a	4.085		22.9	-9.80	43.7	0.423
fcc NiO ^b	4.177	-0.022	5.57	-1.73	180.5	0.312
fcc CoO ^c	4.26	-0.040	6.32	-2.26	158.2	0.358
bcc Fe ^d	2.866	+0.008	7.64	-2.81	130.9	0.368

^aref. [73]

^bWe have taken the average of elastic compliance constants of NiO from the published values in ref. [95]

^cref. [96]

^dref. [32]

5 ML. This finding from stress measurement is corroborated by our LEED and surface x-ray diffraction (SXR) work [88].

To facilitate the discussion of the result, I copy Fig. 4.2 of the stress and MEED results for the growth of NiO on Ag(001) here for convenience. We find a tensile stress change of +0.6 N/m in regime I. It is of opposite sign as compared to the expectation based on lattice misfit. The lattice mismatch between NiO and Ag is $\eta = -2.2\%$, and a compressive stress change of -1.21 N/m per monolayer (ML) is calculated. The absence of MEED intensity oscillations and the unexpected tensile stress in this regime indicate the formation of a peculiar NiO-Ag interface. In the submonolayer coverage, a (2×1) LEED pattern is observed, continued growth of Ni in an O₂ partial pressure (2×10^{-7} mbar) at room temperature leads to a (1×1) pattern. In order to clarify the structure at the interface NiO-Ag and that of the film, surface x-ray diffraction (SXR) experiments have been performed in the institute. These results are analysed in view of our stress results and theory on the bonding between NiO and Ag [88]. The SXR results reveal that a fraction of a monolayer coverage of NiO of roughly 30% is embedded in the Ag (001) surface. The corresponding fraction of Ag atoms is expelled [88]. This scenario has been suggested by STM studies in the past [87, 97–99], and our results corroborate these findings. Thus, misfit arguments fail to describe the stress change in this regime. Here, adsorbate induced surface stress changes are more decisive than misfit stress [100, 101]. It should be noted that the exposure of the clean Ag surface to oxygen, prior to formation of NiO induces a tensile surface stress change of +0.7 N/m (time 0 to 250 s in Fig. 5.1). Hence, it is reasonable to ascribe the tensile stress change during the deposition of the first 1.5 ML NiO to the O-Ag interaction since oxygen sits directly on top of the Ag atom, according to our SXR analysis. SXR gives a structural model where oxygen adsorbs on top of Ag-atoms, while

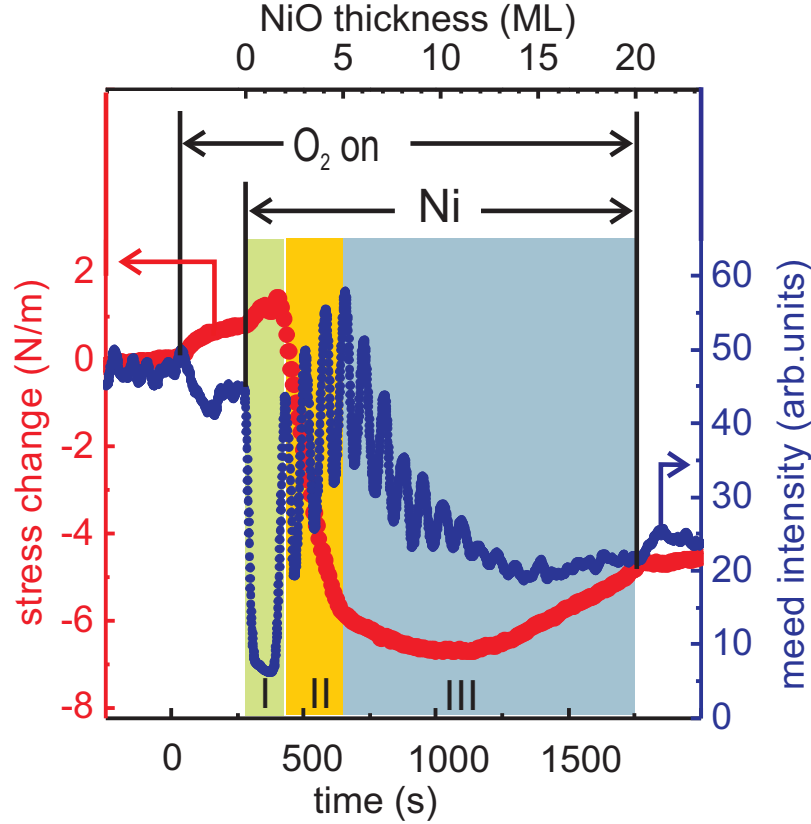


Figure 5.1: Measured stress change (left scale) and MEED intensity (right scale) during Ni deposition on Ag(001) in an oxygen partial pressure of 2×10^{-7} mbar at 300 K. Pronounced MEED oscillations starting from 2 ML are ascribed to layer-by-layer growth of NiO. The compressive stress change from 2–5 ML NiO is due to lattice misfit between NiO and Ag. Three growth regimes are identified from the distinctly different stress and MEED observations. I (0–2 ML NiO): interface formation, II (2–5 ML NiO): pseudomorphic growth, III (5–20 ML NiO): non-pseudomorphic growth).

Ni-atoms reside in hollow sites (see the structure model from SXRD in Fig. 5.2). The embedding of NiO happens in the first monolayer, and further deposition does not change the concentration of the embedded NiO. After embedding of 20–35% NiO in the first monolayer, the second layer grows directly on the Ag(001) surface. This model is confirmed by first-principles calculations based on density functional theory [88].

In regime II, the almost constant slope of the stress curve leads to a compressive stress change of -6.0 N/m at 5 ML (see Fig. 5.1). This measured stress is in quantitative agreement with the calculated stress of -6.1 N/m from continuum elasticity. Stress and pronounced MEED oscillations with a periodicity of 1 ML in this regime are attributed to the coherent layer-by-layer growth of strained NiO. Here, the structure is well described by an epitaxially strained NiO film, as LEED shows (1×1) patterns (see Fig. 4.3 (c)). Also, the extracted in-plane atomic distance from LEED images matches to that of Ag(001), indicating

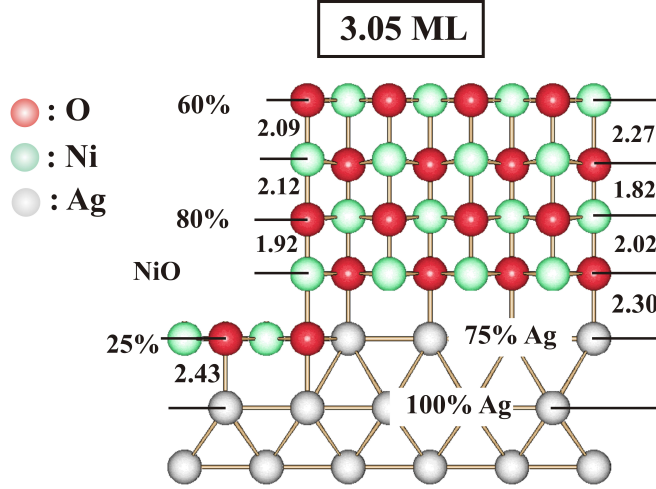


Figure 5.2: Structure model by SXR for 3.05 ML NiO/Ag(001) as taken from Ref. [88]. Red, green, and grey spheres represent O, Ni, and Ag atoms, respectively. Layer stoichiometry and inter-layer spacings in Å are given. The rumpling of NiO layers gives rise to different Ni-O interlayer distances (Ni-O and O-Ni) as written on the left and right. The fractional coverage of a ML is indicated in percent (%) on the left.

pseudomorphic growth. Our SXR analysis revealed that after embedding in the very first monolayer, the next layers grow epitaxially. The structure model for 3 ML NiO/Ag(001) is shown in Figure 5.2, taken from ref. [88]. We find that the bond length d_{O-Ag} at the interface depends on the number of added layers. For 2 and 3 ML NiO the average d_{O-Ag} is 2.403 Å, which is in good agreement with previously reported values for comparable film thickness by EXAFS ($d=2.37\pm 0.05$ Å) [102, 103] and LEED ($d=2.43\pm 0.05$ Å) [97].

According to continuum elasticity theory, the out-of-plane strain ϵ_{\perp} is calculated for pseudomorphic growth of a uniformly strained cubic (001) film from the in-plane strain [28] ϵ_{\parallel} by

$$\epsilon_{\perp} = \frac{-2\nu}{(1-\nu)}\epsilon_{\parallel} \quad (5.1)$$

From this, the out-of-plane strain for fcc-NiO is expected to be +1.92 % (here, '+' sign indicates expansion) and thus the perpendicular interlayer spacing for in-plane elastically strained film is calculated as 2.13 Å. This is in good agreement with the results obtained from the LEED-I(V) measurements for 5 ML NiO, as shown in Figure 4.5. Also, the average interlayer distance for the 3 ML NiO from SXR is close to this value. We conclude that pseudomorphic growth ends at 5 ML NiO. LEED, MEED and SXR support this conclusion from the stress measurement [88].

In regime III, the stress curve levels off and a decay in the intensity of the MEED oscillations is observed. Here, LEED shows streaky patterns, the intensity is

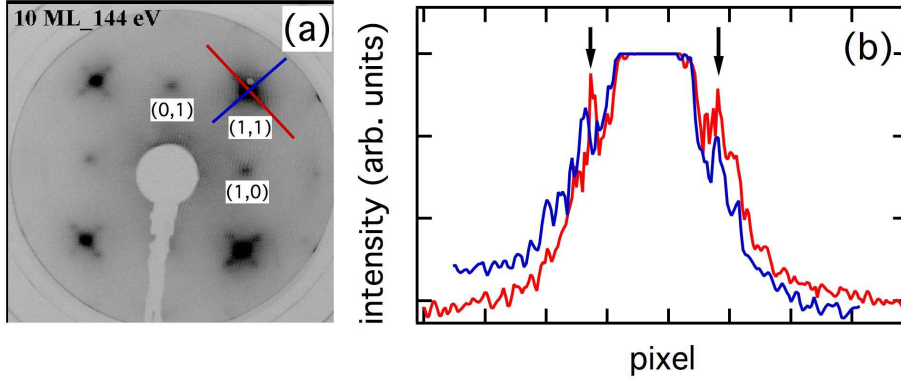


Figure 5.3: (a) LEED image of 10 ML NiO/Ag(001) and (b) the line profile of the (1,1) spot along [100] (red) and along [010] (blue) directions. The satellite peaks are indicated by arrows.

distributed along [100] and [010] directions. The line profile of diffracted (1,1) spot at 10 ML NiO along [100] and [010] directions is shown in Figure 5.3. Satellite spots are barely distinguishable, the satellite peaks are indicated by arrows. These kind of patterns have been reported previously for NiO and MgO films on Ag(001) [47] and for MgO film on Fe(001) [104]. From a quantitative analysis of the position of diffracted spots, we can estimate the average in-plane lattice constant of the film. The result is $a = 2.93 \pm 0.02 \text{ \AA}$, which is close to the bulk value ($a_{\text{bulk-NiO}}/\sqrt{2} = 2.96 \text{ \AA}$), and thus it confirms a strain relaxation above 5 ML.

The MEED oscillations completely disappear around 11 ML. At the same thickness stress starts to relax towards a positive stress change. The change of slope of the stress curve and the decay of the MEED intensity oscillations in this regime are ascribed to the formation of structural mosaic pattern [47]. As the thickness increases the diffraction spots become broader, and the stress relaxes towards tensile stress. This indicates a rougher film morphology and a reduced average film strain.

The LEED analysis of the diffraction patterns shows that the in-plane atomic distance of the surface is increasing after 5 ML and it approaches to that of bulk NiO at 20 ML (see Fig. 4.4). The average stress ($\bar{\tau} = \Delta\tau/t_F$) from the stress curve gives the average lateral strain ϵ_{\parallel} in the film. It is calculated from

$$\epsilon_{\parallel} = \frac{1 - \nu_F}{Y_F} \bar{\tau} \quad (5.2)$$

Figure 5.4 shows a comparison between the calculated strain from LEED and the strain from the measured stress curve. Here, the average film strain for fcc-NiO layers from the measured stress curve is calculated using equation 5.2. The plot shows that both curves qualitatively follow a similar trend. At 5 ML,

both strain from the stress curve and strain from LEED analysis give the same value within the error bar. This indicates that the LEED results are consistent with the stress results. The average stress from stress measurement reflects the average strain of the film. The extraction of this strain from equation 5.2 is based on certain assumptions: (i) it is reasonable for layer by layer growth of epitaxial order, and (ii) the interface stress is not taken into account [29]. As dislocations or defects or roughness are formed in the film beyond pseudomorphic growth, less stress is transferred into the substrate due to stress relaxation. Here, an important point is that the average strain from stress measurements reveal considerable strain even in 20 ML NiO. To address the interface stress one needs to analyse the slope of the stress curve as a function of thickness. Interface stress effects are evident as deviation from the misfit-induced stress curve at a smaller thickness from 0–2 ML of NiO in Fig. 5.1.

The out-of-plane interlayer spacing is linked to the in-plane strain for pseudomorphic growth, see equation 5.1, and the largest deviation from the bulk like NiO layer spacing is expected for pseudomorphic growth. The results of the out-of-plane strain analysed by LEED I(V) is presented in Fig. 4.5. After the end of pseudomorphic growth (above 5 ML), one would expect that the out-of plane interlayer spacing should relax towards the equilibrium spacing of $a_{NiO,bulk}/2 = 2.09 \text{ \AA}$. However, this is not observed in the LEED I(V) analysis. This can be ascribed to the loss of coherent epitaxial order in the film. We have found misfit dislocations above 5 ML, which leads to a reduced strain in the film. Therefore, the application of eq. 5.1 in a regime of non pseudomorphic growth is less reliable. The interlayer spacing beyond pseudomorphic growth, $t_F > 5 \text{ ML NiO}$, has not been investigated by SXRD.

CoO on Ag(001)

In case of CoO on Ag(001), the stress measurements show a complex dependence on the film thickness (see Fig. 4.7 (a)). The stress curve during formation of CoO at 450 K indicates an almost stress free growth for the initial 1.5 ML. It is followed by a compressive stress change with two distinct slopes until the end of deposition. LEED shows a (1×1) structure over the whole thickness range of CoO film, as shown in Fig. 4.7 (b). The growth of CoO at 300 K leads to the formation of a precursor, which contains islands of different CoO arrangements (like O/Co and CoO). This has been suggested in previous STM studies [87,105]. The LEED patterns show very broad spots and weak intensities indicative of poor long range crystalline order. This is why the CoO deposition is performed at elevated temperature. Higher growth temperatures are expected to improve the growth conditions to acquire a film of better long range epitaxial order.

Unlike the stress measurement during oxygen exposure at 300 K prior to NiO formation, which induces a tensile surface stress of $+0.7 \text{ N/m}$, the oxygen exposure at 450 K does not lead to any significant stress change (see Fig. 4.7). It may indicate that oxygen atoms do not adsorb at this oxygen partial pressure ($2 \times 10^{-7} \text{ mbar}$) and temperature. This view is supported by a phase

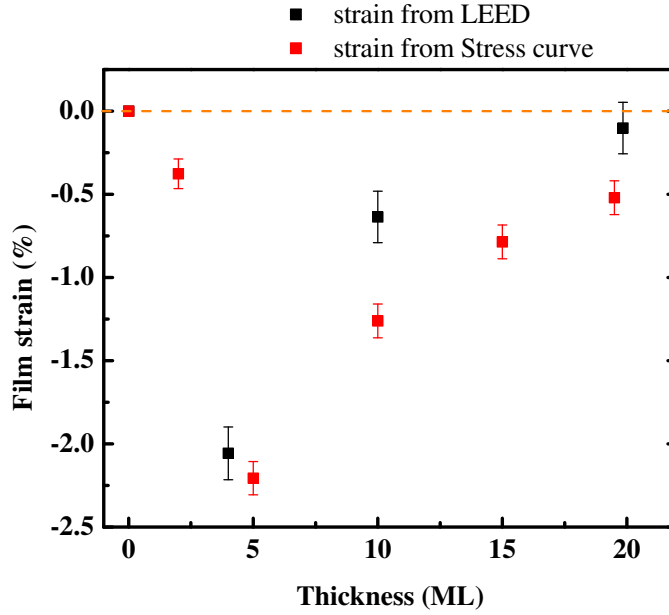


Figure 5.4: In-plane strain as a function of NiO film thickness on Ag(001), red data points (strain from the measured stress curve) and black data points (extracted from the LEED images).

diagram reported by Stierle *et al.* [106] and Costina *et al.* [107]. A much larger partial pressure of oxygen $\approx 10^{-2}$ mbar and more is required for the onset of the O-induced surface restructuring of Ag(001) or for Ag_2O formation. In the thickness range of 0–2 ML of CoO, the measured stress change is order of +0.3 N/m. However, it is surprisingly different from the calculated misfit stress of -2.1 N/m per ML. We attribute this observed small tensile stress at low coverages of CoO to double layer CoO islands with Ag patches on the surface, as has been reported in STM studies [87, 108]. These results indicate that simple stress-strain relations are not applicable here, due to inhomogeneous surface morphology and composition. It can be speculated that CoO is embedded in Ag(001) as it was observed for NiO on Ag(001). Under these conditions the adsorbate induced surface stress is an important stress contribution, which leads significant deviation from epitaxial misfit stress [30, 109].

A regime of compressive stress with a slope of -2.6 GPa up to around 4 ML is observed. This linear drop of the stress curve may indicate a constantly strained film in the thickness range of 1.5 to 4 ML. Further Co deposition in an O_2 partial pressure at 450 K leads to a smaller slope of -0.7 GPa at 9 ML. As mentioned before the lattice mismatch between Ag and CoO is $\eta = -3.99\%$, larger than the misfit of -2.2% for NiO/Ag(001). This leads to a compressive stress of -9.8 GPa, which is almost a factor of 4 larger than the measured stress. It is clear from the results that the measured stress does not correspond

to the misfit stress. This result suggests that here other contributions to the stress and possibly stress relaxation in CoO islands are dominant. This reveals that the CoO film does not grow pseudomorphically strained and possibly not in a layer-by-layer mode on Ag(001) initially. This leads to deviation from the calculated misfit stress.

From the thickness dependent LEED I(V) analysis at 1.5 ML, the interlayer distance is $d = 2.32 \pm 0.07 \text{ \AA}$ (see Fig. 4.8). This value is in good agreement with the previously reported interlayer distance for the first monolayer of CoO such as $2.4 \pm 0.1 \text{ \AA}$ [110]. This value is close to the calculated value within the error bar for an in-plane strained film ($d = 2.31 \text{ \AA}$). Vertical layer relaxation is observed above 1.5 ML, and at 10 ML the layer spacing is close to the equilibrium state ($a_{\text{CoO,bulk}}/2 = 2.13 \text{ \AA}$). However, at 10 ML ($2.19 \pm 0.02 \text{ \AA}$), it is still larger (+2.3 %) as compared to the bulk of CoO (2.13 \AA). The relaxation in thicker film results from relaxed in-plane strain as found from our stress measurement. There is still some residual strain in the 9 ML CoO film. It is remarkable that a perpendicular expansion at 1.5 ML of CoO film is visible from LEED I(V) analysis, although no misfit stress is observed. As mentioned before, it is difficult to predict the out-of-plane strain relaxation when film morphology and strain deviate from pseudomorphic layer-by-layer growth.

5.2 Effect of NiO on the coercivity and magnetoelastic coupling of Fe monolayers

In this section, I discuss the results on the magnetic properties of Fe monolayers deposited on 20 ML NiO/Ag(001) and 10 ML NiO/Ag(001). I focus on the effect of the NiO spacer on a 6 ML Fe film in view of the induced large coercive field (H_c) and magnetoelastic coupling coefficient B_2 . The results are compared with those for 6 ML Fe/Ag(001). This section sheds some light on the effect of CoO on the coercive field of Fe films. I present a critical assessment of B_2 of the 6 ML Fe film on NiO/Ag(001) in view of previous B_2 measurements on other substrates.

Effect of NiO on the coercivity of 6 ML Fe

The lattice mismatch between bcc Fe ($a_{\text{Fe}} = 2.866 \text{ \AA}$ [67]) and bulk fcc NiO is $\eta = \frac{a_{\text{NiO}}/\sqrt{2} - a_{\text{Fe}}}{a_{\text{Fe}}} = +3.04 \%$. Here, we assume an epitaxial orientation of Fe on NiO as outlined in Fig. 5.5, and the crystallographic orientation of Ag(001) is as sketched in Fig. 3.6 (a). The calculated biaxial film stress from linear elasticity corresponding to this strain is tensile with a magnitude of $\tau_F = +6.3 \text{ GPa}$. The stress curve obtained during the deposition of 6 ML Fe on 20 ML NiO/Ag(001) presents a positive slope of +5.7 GPa up to 5 ML, which is in remarkably good agreement with the calculated value. After 5 ML a slightly reduced slope is observed, as shown in Fig. 4.10(a). The agreement of measured stress with the

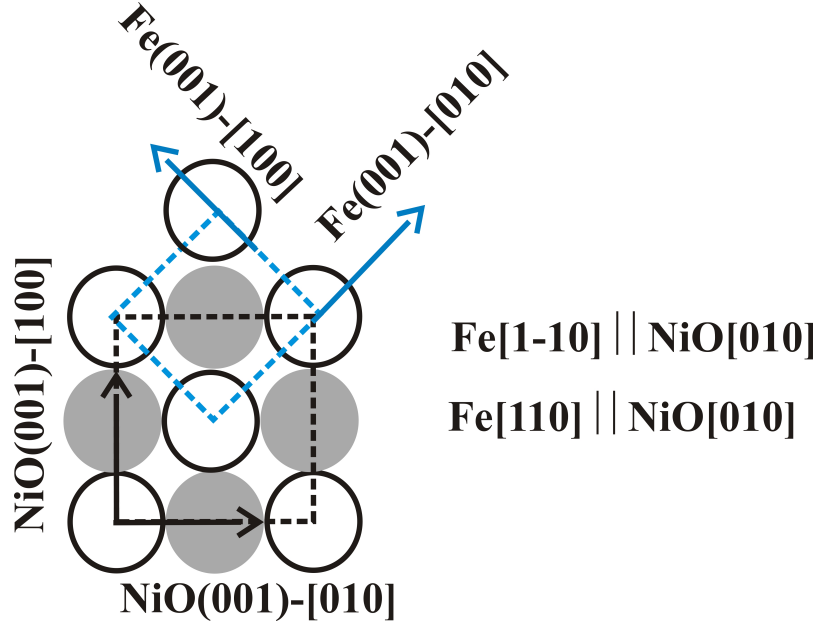


Figure 5.5: The sketch of the epitaxial bcc Fe lattice on NiO (001) when Fe sits on Ni site, the blue dashed line indicates unit cell of the bcc Fe. The grey circle represents oxygen atoms of NiO.

misfit stress indicates epitaxial growth of pseudomorphically strained bcc-Fe on 20 ML NiO/Ag(001) up to 5 ML, further deposition leads to a slightly relaxed stress in the Fe film. LEED of 6 ML Fe/20 ML NiO/Ag(001) shows a (1×1) pattern (see Fig. 4.10(b)).

The epitaxially grown 6 ML Fe film on top of 20 ML NiO/Ag(001) [15, 111] is under a residual strain of +2.4 %, as this thickness is slightly above the end of pseudomorphic growth at 5 ML. The epitaxial model for bcc Fe on NiO/Ag(001) is sketched in Figure 5.5. The easy axis of magnetization of the Fe film is in the plane, along Fe $\langle 100 \rangle$. It has been presented in the previous chapter that the coercive field of 6 ML Fe deposited on 20 NiO/Ag(001) at 300 K is large (141 mT), and it does vary with temperature (see Fig. 4.11). Also, the dependence of H_c on the thickness of NiO is characterized, and the start of enhancement is observed at around 8 ML of NiO at 300 K.

The coercivity of 6 ML Fe grown on 20 ML NiO/Ag(001) at 300 K is ≈ 141 mT, it decreases with increasing temperature. This value is almost factor 15 larger than that of the 6 ML Fe deposited directly on Ag(001), see Fig. 2.4. At 480 K, H_c is ≈ 9 mT, is exactly the value for 6 ML Fe on Ag(001) at 300 K, see Fig. 5.8.

From the T-dependence of H_c we conclude that the large coercivity of 6 ML Fe in contact with 20 ML NiO at 300 K is related to the antiferromagnetic (AFM) order of the NiO film. The spins of the AFM layers at the interface directly couple to Fe and make the magnetic reversal of Fe more difficult.

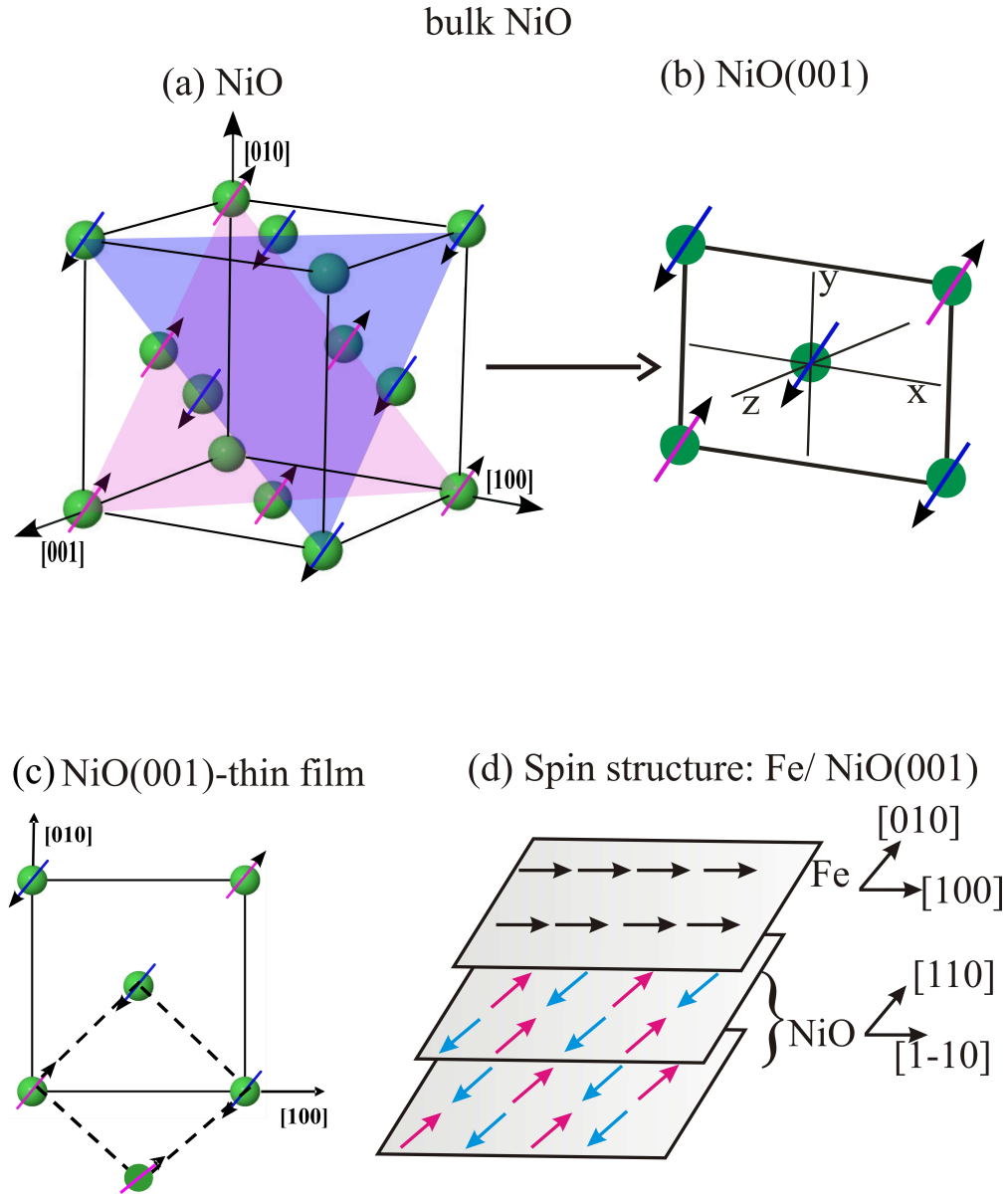


Figure 5.6: Sketch of spin structure: of bulk NiO: spin direction (arrow) $\langle 11\bar{2} \rangle$ \parallel $[112]$ (a). The shaded areas indicate (111) planes with their respective spin directions. (b) bulk NiO(001) surface. (c) NiO (001) thin film: spin direction $[110]$ or $[\bar{1}\bar{1}0]$ [15]. The dashed square represents the unit cell of the (001) plane. For clarity only the Ni atoms are shown. (d) in-plane perpendicular coupling of Fe with Ni spins in NiO film on Ag(001) [15]. Here, the color of the arrows is for distinction. Note: in the (001) plane: $\text{Fe}[100] \parallel \text{NiO}[110] \parallel \text{Ag}[110]$.

The simplest model for this phenomena has been presented in ref. [11]. The spins at the antiferromagnetic NiO(001) surface are coupled to the ferromagnetic Fe spins by the exchange interaction, which favors an in-plane alignment of the spins. A larger magnetic field is required to rotate the spins of the AFM

film into the surface together with the Fe spins. Consequently, an enhancement of the coercivity occurs, as has been seen in longitudinal MOKE along $\langle 100 \rangle$ direction of the Fe film (see Fig. 4.11).

The topmost layer of the AFM film, which is in contact with FM layer is dragged by the FM spins, while the successive layers of the AFM film follow the antiparallel alignment due to superexchange interaction of the AFM film. However, in thin films the spin orientation is different from the bulk [113], due to strain induced by the substrate [113, 114], the reduced symmetry, and the different atomic environment. Recently, it has been reported that at 30 ML NiO the spins are aligned in the plane along $[110]$ or $[\bar{1}\bar{1}0]$ direction [15, 115].

The simplified sketch of the spin structure for bulk NiO and for NiO(001) thin film is shown in Figure 5.6 (a, b, c). During the Fe deposition, the surface spin orientations of NiO(001) are expected to be strongly affected by the spin exchange interaction at the interface. It has been reported in the literature that Fe spins are coupled 90° with Ni spins in NiO in the plane of the film [15, 115]. A sketch for in-plane perpendicular coupling between Fe spins with the Ni spins at the Fe-NiO interface is presented in Figure 5.6 (d).

It is observed that the remanent Kerr intensity of the Fe film on 20 ML NiO/Ag(001) measured along the $[010]$ direction of Fe, decreases with increasing temperature, as shown in Figure 5.7. A remanent Kerr intensity of the Fe film on Ag(001) is shown for comparison. The reported Curie temperature for thicker than 5 ML Fe/Ag(001) is equal to 1000 ± 100 K [116], and this is comparable to the value of bulk bcc Fe. I conclude that the T-driven variation of the remanent Kerr intensity is comparable for Fe/NiO/Ag(001) and Fe/Ag(001), only the absolute magnitude of the signal is larger by 5-10%. This can be ascribed to thickness calibration errors and the possible effect of the NiO intermediate layer on the magneto-optic response of Fe/NiO/Ag as compared to Fe/Ag.

To further explore the link between coercivity and AFM order of NiO, the coercivity of the Fe film is measured as a function of NiO film thickness. The increase of H_c starts from the particular thickness of 8 ML NiO at 300 K. This may be attributed to the establishment of the antiferromagnetic (AFM) order of the 8 ML NiO film. It is known that the transition temperature of the AFM order strongly depends on the film thickness [117]. The Néel temperature increases with film thickness, and for 5 and 10 ML NiO it has been reported to be around 298 K and 430 K, respectively [118]. From this we interpolated that an 8 ML NiO has T_N well above 300 K, hence, the AFM-FM coupling can induce the increase in H_c at this thickness. Below 8 ML the NiO film is in the paramagnetic state at 300 K, and therefore no enhancement in H_c is observed. Just above this thickness the NiO begins to order antiferromagnetically at 300 K. At low NiO thickness, the stiffness of the AFM order of the NiO layer is not sufficient to resist the torque experienced by the coupling to the ferromagnetic Fe spins, and therefore the NiO spins, possibly those located at the interface, are

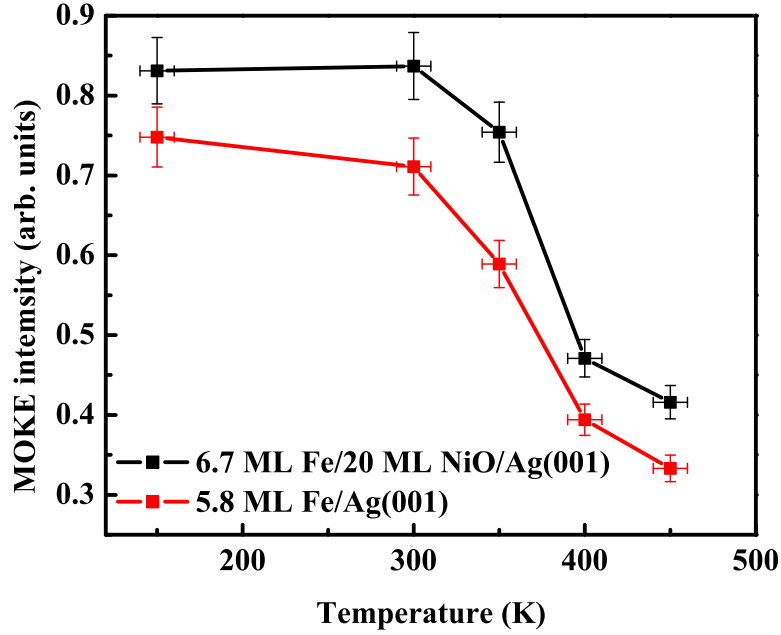


Figure 5.7: Remanent Kerr intensity of 6.7 ML Fe/20 ML NiO/Ag(001) (black) as a function of temperature. For comparison, the remanent Kerr intensity of 5.8 ML Fe/Ag(001) (red) is also shown.

dragged together with the reversing Fe spins. As the NiO thickness increases, the coupling of the interface spins to the AFM film produces a more rigid spin structure in NiO, and an increased H_c is observed. At and above 20 ML NiO this effect is fully developed, and the increase in coercivity saturates.

It is noticeable that the increase in H_c starts in the level off regime of stress curve of NiO film on Ag(001), where the average film strain is reduced (see Fig. 5.1, regime III). Another factor in the understanding of an enhanced coercivity of Fe film in addition to the temperature effect on T_N as explained above, is the magnetoelastic coupling. A film beyond its pseudomorphic thickness is expected to exhibit local imperfection and defects, which induce a variation of strain. This expectation is reasonable here, as the NiO film is beyond the pseudomorphic thickness, and structural imperfections are expected. These will also induce corresponding strain variation in the Fe film. Such a strain variation can induce change in the magnetic anisotropy through magnetoelastic coupling. This will lead to an enhanced coercivity due to domain wall pinning [119]. These issues prompted us to measure the magnetoelastic (ME) coupling coefficient of the Fe film at different thicknesses of NiO. The surprising finding of an enhanced ME coupling B_2 is discussed later in this section.

The temperature dependence of H_c might be ascribed to a softening of the spin ordering in the NiO film. This weakening of the spin order may lead to the decrease of impact of the coupling between NiO (AFM) to Fe (FM) layers

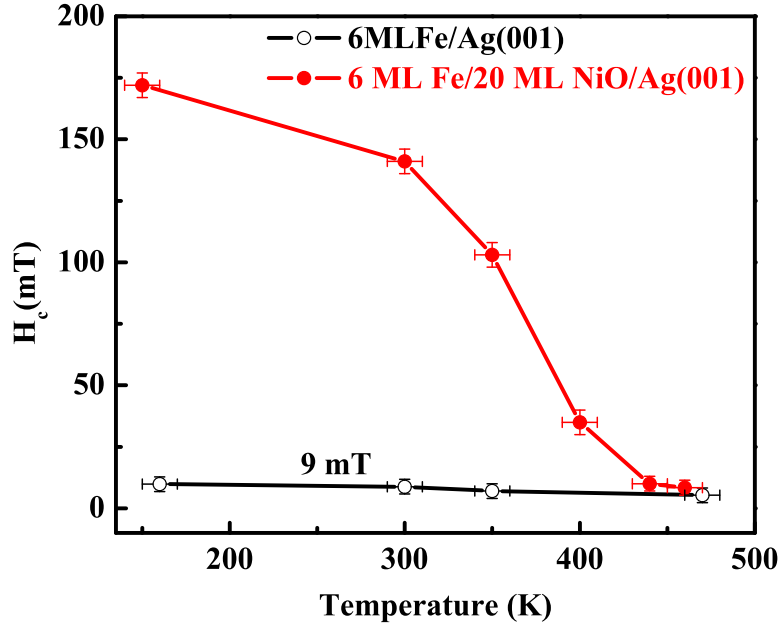


Figure 5.8: Coercive field of 6 ML Fe deposited on top of 20 ML NiO/Ag(001), and for comparison the coercive field of 6 ML Fe/Ag(001), as a function of temperature.

on coercivity, as shown in Fig. 5.8 (red data points). This result supports the view that the coercivity enhancement is indeed largely due to the AFM order of the NiO layers. It should be noted that the system is thermally stable in view of stoichiometry up to 480 K as checked by AES, and also confirmed by reproducibility and reversibility of the MOKE hysteresis loops. From this measurement, it is observed that at $480 \text{ K} \pm 10 \text{ K}$ the NiO film does not show any obvious effect on the coercivity of Fe film. For comparison, the coercivity of 6 ML Fe/Ag(001) is plotted in Figure 5.8 (black data points). This indicates that at this temperature both systems show similar H_c . This suggests that the film has lost its long-range antiferromagnetic spin order, and 480 K marks the Néel temperature of 20 ML NiO on Ag(001). Thus, the H_c vs T plot can be used to estimate the Néel temperature of the AFM film. This method has been used previously to determine the ordering temperatures in FeMn/Co bilayers on Cu(001) [120] and Ni/FeMn [121]. This observed T_N is in quantitative agreement with previously reported 470 K for 20 ML NiO/MgO(001) [118].

From our measurements, we attribute this coercivity enhancement and its temperature dependence to the AFM order of the NiO film. To which extent the effect of pinning of defects [122], domain nucleation and roughness of the surface may induce an increase in switching field [119, 123], contributing to the enhanced H_c , requires further investigations.

Our results on $H_c(T)$ suggest that the increase in coercivity is indeed due to an AFM order of the NiO film. In the literature, it has been discussed that

the AFM layer in contact with a FM layer will produce exchange bias (a shift of the hysteresis loop either left or right depending on the direction of the applied field) [8, 10, 11, 124]. Note that the hysteresis loops acquired from the sample (6 ML Fe/20 ML NiO/Ag(001)) do not show any shift even after field cooling in a field of up to 200 mT. The reasons for not observing exchange bias could be due to the following points. Firstly, at this thickness (20 ML) of NiO the anisotropy energy of the film may not be strong enough. The increase in anisotropy of the NiO film with thickness is the origin of the increase in coercive field with NiO thickness through coupling with the Fe overlayer. From our MOKE measurements we found that the coercivity of the Fe film on 20 ML of NiO reached its maximum, indicating that anisotropy of the NiO film is almost saturated. Therefore, the possibility of this effect can be ruled out for our system. Secondly, the interface does not have the required frozen spins, as has been suggested for Fe/CoO [14]. Frozen spins are necessary to pin the FM spins. Thirdly, the number of uncompensated interfacial spins is insufficient [10, 125]. This aspect seems important here as NiO(001) is known to exhibit a fully compensated surface [115]. It is usually assumed that the compensated spins should be frozen to generate an exchange bias [125–128]. These last two points are probably the effects which come into play to prevent exchange bias for our system.

Role of CoO on the coercivity of Fe monolayers

Similar to 6 ML Fe/20 ML NiO/Ag(001), Fe on 20 ML CoO/Ag(001) exhibits in-plane hysteresis loops with extremely large switching fields below 300 K. This contrasts with the results above, where already at 300 K a large H_c is observed for NiO intermediate layers. In view of the discussion above I ascribe this to the reduced T_N of CoO, as compared to NiO (see Table 5.2). The temperature dependent H_c of Fe at two different thicknesses of CoO shows a linear increase of H_c with decreasing temperature (see Fig. 4.14). From this measurement, the extracted T_N is 276 K and 288 K with an error bar of ± 5 K corresponding to 10 and 20 ML of CoO, respectively. T_N for 20 ML CoO is very close to T_N of bulk CoO. However, T_N of 10 ML CoO is slightly lower than the previously reported 290 K [129], for sputtered CoO/Fe bilayers ($T_{AFM}=289$ K) [12]. The enhancement in H_c of the 6 ML Fe on both 10 and 20 ML CoO is very similar below T_N , when the anti-ferromagnetic order is established. This might indicate almost the same strength of AFM order at both CoO films, irrespective of the thickness. It also suggests that the 10 ML CoO has already attained the maximum stiffness of the spin structure, and consequently the coercivity enhancement is saturated already for this thickness. From this we may infer that the exchange coupling of the 10 ML CoO film to the adjacent Fe film is stronger than that of the 10 ML NiO film, although T_N is lower for CoO.

Table 5.2: Néel temperature (T_N) of NiO and CoO films grown on Ag(001), extracted from H_c vs T plot. Bulk T_N is taken from ref. [89].

		T_N (K)
NiO	bulk	523
	20 ML	480±10
CoO	bulk	291
	20 ML	288±5
	10 ML	276±5

An interesting point is that for CoO/Ag(001), the coercivity of 6 ML Fe exhibits a linear temperature dependence, whereas on NiO film on Ag(001) it is not linear. This might indicate that the temperature dependence of the exchange coupling between FM and AFM coupling is different in both systems.

Overall, from our NiO thickness and temperature dependent MOKE measurements we conclude that the increase of H_c is mainly driven by the AFM order of NiO and CoO films. The measured T_N for NiO and CoO films is summarized in Table 5.2.

From the literature it has been known that both NiO [15, 115] and CoO [129] films have in-plane alignment of the spins, which is different from bulk. However, from our stress measurements it is observed that both films induce compressive stress on Ag(001), in case of CoO it is much smaller. One might speculate that the compressive stress or strain drives this deviation of the spin structure from the bulk orientation. As a result, H_c of 6 ML Fe film on NiO starts to increase where stress of NiO film levels off. Stress measurements of CoO show a significantly reduced stress as compared to the calculated misfit. CoO leads to a saturated H_c increase already at 10 ML. Whereas in case of NiO/Ag(001) the saturation occurs at 20 ML. It has been pointed out in the literature [114] that the CoO films grown on different substrates show different magnetic properties due to different strain in the film. Strain induced local crystal fields together with the spin-orbit interaction determine the magnetic anisotropy, as well as the spin and orbital contributions to the magnetic moments. Previous work [114] found for the CoO/Ag(001) system that the induced compressive strain results in an in-plane direction of the spin moments. Whereas, for CoO/MnO(001), tensile strain results the out-of-plane direction of orbital and spin moment. It has also been suggested in the literature that the coercivity and the anisotropy field of the $NiO/Ni_{80.2}Fe_{19.8}$ bilayers are significantly affected by stress [130].

Comparison of magnetism and magnetoelastic coupling of Fe/NiO on Ag(001) with Fe/Ag(001)

The results presented in section 4.2.2 showed an unexpectedly large magne-

toelastic coupling (ME) coefficient B_2 for 6 ML Fe on 10 ML NiO/Ag(001) of $B_2 = -19.6 \pm 1.6 \text{ MJ/m}^3$ (see Fig. 4.15(b)). For comparison, I also measured B_2 of 6 ML Fe directly grown on Ag(001), and found $B_2 = +2 \pm 0.6 \text{ MJ/m}^3$. From our combined stress and magnetoelastic stress measurements, it is found that B_2 of the Fe film on these two substrates is drastically different, although the in-plane stress and consequently the strain of the Fe film are comparable.

As discussed above the Fe film shows an easy axis along $\langle 100 \rangle$. For the appreciation of the ME stress results it is important that these measurements were performed on a crystal with its long edge along $[110]$, and its width along $[1\bar{1}0]$. (see Fig. 3.6 (b)), as explained in section 4.2.2. The Fe film is magnetized along Fe- $[110]$, which is assumed to be an intermediate easy axis [18]. Our results from MOKE measurements reveal that the Fe film can be easily saturated in low magnetic fields along $[110]$ and $[1\bar{1}0]$. It is worth to note that the measured H_c of 6 ML Fe/10 ML NiO/Ag(001) along these two orthogonal directions is similar to the H_c measured along in-plane $\langle 100 \rangle$ directions of the Fe film, as discussed above. This indicates that the in-plane magnetic anisotropy is not pronounced in this case. In case of Fe/Ag(001), the transversal MOKE loop shows a rectangular behavior with a very small switching field, whereas the longitudinal MOKE shows a step in ascending branch of the hysteresis loop (see Fig. 4.17(a)). The origin of this asymmetric hysteresis loop is not clear yet, but its observation still allows to extract the minimum field, which is needed to achieve saturation along the sample width. A field of 40 mT is applied for the ME stress measurements.

The ME coupling coefficient B_2 of the 6 ML Fe film on 10 ML NiO/Ag(001) is -19.6 MJ/m^3 , which is opposite in sign and different in magnitude from the bulk value of $+7.83 \text{ MJ/m}^3$ [28]. From our MOKE measurements we find that the 10 ML NiO still leads to an increased coercivity, as discussed above. Note that we cannot perform ME stress measurements on 20 ML NiO, as here the enhanced coercivity is beyond the maximum attainable field in the vertical direction (0.1 T). T_N of 10 ML NiO/MgO(001) is 430 K [118]. Thus, our measurements at 300 K are in the AFM phase of NiO. The measured B_2 of 6 ML Fe on Ag(001) is $+2.0 \text{ MJ/m}^3$, which is almost a factor 4 smaller than the bulk value.

The deviation of ME coupling coefficients of thin films from their bulk has been reported before [21, 23, 28, 57–59, 131, 132]. The ME coefficient B_2 of 6 ML Fe/Ag(001) does not reveal any clear film thickness nor strain dependence in view of the error bar (see Fig. 4.18). The value of B_2 is much smaller than the bulk value of $+7.83 \text{ MJ/m}^3$ in the investigated thickness range, which we will discuss further in view of the literature. A similar behavior of a small B_2 of Fe monolayers has been observed on Ir(001) before [21, 26]. One might be tempted to assume that the interface is crucial for the deviation of B_2 from the bulk. The nature of different interface was further investigated by performing ME stress measurements on the Fe film which was deposited on oxygen exposed Ag(001). Our results reveal that oxygen adsorption on Ag(001) does not influ-

ence B_2 , nor the MOKE of the Fe film. Note that the observed stress during Fe deposition on O/Ag(001) is similar to that of an Fe film grown directly on Ag(001). This suggests that Fe film morphology and stress are similar for these two substrates, and B_2 remains unaffected. This result indicates that in the case of Fe/NiO/Ag(001), the interface coupling between Fe and NiO is critical for the enhanced B_2 value.

To understand the significant difference between B_2 of the Fe film on 10 ML NiO/Ag(001) as compared to Fe/Ag(001) with comparable stress, B_2 is measured as a function of NiO thickness. The visual analysis of the plot B_2 as a function of NiO thickness and in-plane strain, see Fig. 5.9 (a) and (b), reveals that B_2 of the 6 ML Fe film is smaller in magnitude at low thickness and larger at larger thickness (on a negative scale). A similar trend is observed for the strain dependence of B_2 .

It appears tempting to correlate the enhanced B_2 with the AFM order of NiO. To elucidate this hypothesis T-dependent ME stress measurements are called for. However, due to the extreme small effects, long data acquisition time of order of hours are used to extract B_2 of 6 ML Fe. Thermal drift is detrimental in this respect. Therefore, the measurements are preferably performed at 300 K. However, a thickness variation of NiO can imitate some extent to this. The 300 K would correspond to T_N of a 6 ML NiO film as according to our thickness and temperature dependent coercive field plot, and thicker films are expected to be AFM ordered. This process is used for our ME measurements, as discussed above. This approach suggests a link of the large B_2 with the AFM order of NiO.

To explore the possible impact of staking sequence AFM/FM/Ag or FM/AFM on Ag, we prepared a reverse interface by first depositing 6 ML Fe on Ag(001) and then 10 ML NiO on top of it. The magnitude of B_2 for the inversed bilayers is significantly reduced as compared to the case of the Fe on the top of NiO, but it remains negative. As indicated in Figure 5.9, in the plot the red data points correspond to ME coupling constant for the reversed bilayers (10 ML NiO/6 ML Fe/Ag (001)). The B_2 of 10 ML NiO/6 ML Fe/Ag(001) is -7.76 MJ/m^3 , which is equivalent to 6 ML Fe/7 ML NiO/Ag(001) (see Figure 5.9). However, these two systems are not comparable in terms of the growth behavior and consequently interface quality. The growth mode and the resulting film morphology are expected to differ for the two stackings. The larger diffraction spots and the reduced contrast of the LEED pattern for the NiO film on 6 ML Fe/Ag(001) shows that the overlayer NiO does not order as well on Fe as it does on Ag(001). Epitaxial growth is favored for Fe on NiO, but not vice versa [133, 134]. As has been confirmed by our LEED measurements, 10 ML NiO/6 ML Fe/Ag(001) shows very blurred spots as compared to 6 ML Fe/10 ML NiO/Ag(001). This points to a rougher film morphology. The same thickness of Fe in these reversed interface systems induce a slightly different stress, and B_2 is also different (B_2 vs Fe film strain, Fig. 5.9 (b)). It appears that the ME coupling coefficient B_2 is strain dependent rather than thickness

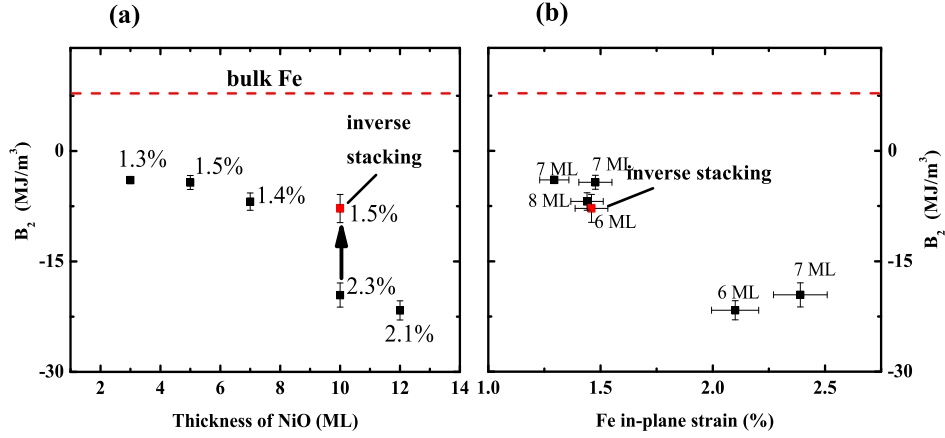


Figure 5.9: Thickness and strain dependence of the ME constant B_2 for 6 ML Fe deposited on top of 10 ML NiO/Ag(001). The red data point represents 10 ML NiO/6 ML Fe/Ag(001). Here, the arrow indicates a change in magnitude of B_2 for the reversed interface. The corresponding in-plane strain and the Fe film thickness are labeled for each data point. For comparison: B_2 for 6 ML Fe/Ag(001) = $+2 \text{ MJ/m}^3$, bulk Fe $+7.8 \text{ MJ/m}^3$.

in this particular frame of reference.

We conclude that the deviation of B_2 of 6 ML Fe/10 ML NiO/Ag(001) from that of 6 ML Fe/Ag(001) is due to the spin structure of NiO, which might get affected when the magnetic field is applied, and the exchange coupling at the interface. To clarify the issue of interface coupling, the ME measurements are performed with Ag inter-spacer layer between the NiO and Fe films to weaken the FM/AFM coupling. First results indicate that as we put 0.5 ML of Ag, the B_2 of the 15 ML Fe/0.5 ML/10 ML NiO/Ag(001) becomes positive and the magnitude is close to the 6 ML Fe on Ag(001). This might suggest that the FM-AFM interface coupling is decisive for the large and negative B_2 of the Fe film. Clearly more work on this is called for, to identify the physical origin of this first observation of an enhanced ME coupling of an FM film on an AFM surface.

Critical assessment of the magnetoelastic coupling B_2 on NiO layers in view of previous B_2 measurements on other substrates

The deviation of magnetoelastic coupling of thin ferromagnetic films from their respective bulk values has been reported before from experiment and theory [21, 22, 53, 132]. The first experimental evidence for the deviation of magnetoelastic coupling in the surface layer of a ferromagnetic sample from the respective bulk values was presented by Sun and O'Handley [132] in 1991. This effect was referred to the surface contribution B^s . Later on, for thin films, the measured first-order magnetoelastic coupling coefficients B_1 , and B_2 for a fcc Co thin film on Cu(111) have been expressed as the surface and interface effects added as a

correction term to the bulk magnetoelastic coupling coefficients and formulated as $B_i^{eff} = B_i^{bulk} + B_i^S/t$ [135,136]. It was believed that ME coupling coefficients varies inversely with the thickness of the ferromagnetic films. However, later this interpretation was proven invalid by the same author, and by the others [21,57,131]. Strain in ultrathin film was considered as an important contribution to B^{eff} . Its contribution is formulated as $B_i^{eff} = B_i^{bulk} + D_i\epsilon_{||}$ [131]. Most of the recent results [19, 20, 57–59] followed this model successfully, for example B_1 of Fe, Co and Ni and also B_2 of Ni/Ir(001) [21], however, the same model was unable to describe B_2 of Fe and Co/Ir(001) [21].

From our measurement, B_2 of Fe/10 ML NiO/Ag(001) differs in both sign and magnitude from the bulk value. In the case of Fe/Ag(001) only the magnitude is smaller. In these two systems, the strain of the Fe film is comparable, only the interface is different. In order to explore the interface effect, we have performed the measurements by depositing the Fe films on the oxygen covered Ag surface. We find that the oxygen adsorption on Ag (001) does not influence the B_2 of Fe film (some of the data points are plotted in Fig 4.18). This corroborates our assessment that the antiferromagnetic order of NiO is the essential aspect here.

To explore this issue more, the ME measurements are performed with Ag inter-spacer layer between the NiO and Fe films to weaken the FM/AFM coupling, recently. The results indicate that as we put 0.5 ML of Ag, the B_2 of the 15 ML Fe/0.5 ML/10 ML NiO/Ag(001) becomes positive and the magnitude is close to the 6 ML Fe on Ag(001). This might suggest that the FM-AFM interface coupling makes the large and negative B_2 of the Fe film. First data are obtained and this needs to be investigated further.

Furthermore, one mechanism that can cause a deviation of the magnetoelastic coupling from the bulk is the influence of the film morphology. Kim and Silva reported an increase of the magnetostriction in sputtered permalloy films from zero to negative values of order -2×10^{-6} for a film thinner than 7 nm [137]. It was claimed that the deviation from the bulk behavior is correlated with the measured increase of the surface roughness, although additional influence of residual stress was not excluded. A clear microscopic understanding about the role of roughness on magnetoelasticity has not been established yet for our system, and this complicates the analysis further.

So far there is no conclusive approach which can adequately describe the effect of the AFM-FM interface on the ME coupling coefficient B_2 . This is the first measurement for B_2 of Fe on a presumably AFM ordered NiO film. Previously proposed mechanisms which drive a deviation of B_i from its bulk value such as strain, thickness, roughness do not seem to apply here. The possible explanations are discussed above. In particular, the AFM order of NiO and the Fe-NiO interface is suspected to play an important role for the deviation of B_2 from its bulk value. These new results raise one important question about how

ME coupling is affected by the surface and the interface of FM/AFM layers and call for a new mechanism which influences the magnetoelastic properties of FM/AFM compounds.

5.3 Correlation between stress, strain and structure of Co and Ag/Pt(111)

In this section stress induced by metallic monolayers (Co and Ag) on Pt(111) is discussed, and the results are correlated with lattice strain and magnetism of Co/Pt(111).

Stress induced by Co deposition on Pt(111) at 300 K shows a non-monotonic change for a thickness below 2 ML, whereas at higher thickness a constant slope of the curve is observed up to the end of deposition at 7 ML. The slope of the curve corresponds to a film stress of +3.5 GPa. Low energy electron diffraction (LEED) in this thickness range identifies an epitaxially ordered film with a characteristic of additional diffraction spots which identify as a so-called Moiré pattern. This pattern is a result of a different average in-plane spacing of the Co layer with respect to the Pt(111) substrate. It has been observed previously by STM [138, 139].

The lattice mismatch between Co and Pt is +10.4 % (the lattice constants are listed in Table 5.3). As a result, a tensile stress of +40 GPa is calculated for pseudomorphic growth of Co on Pt(111). However, the observed stress is almost a factor of ten smaller. We conclude that here structural relaxations occur already in the first layer. A most interesting aspect is the growth of the first layer of Co on Pt(111). In many cases a pseudomorphic growth in the first layer [21, 142] has been observed. However, our stress measurements for Co on Pt(111) do not indicate pseudomorphic growth in the first layer. We find a stress very different from the lattice misfit. This may be ascribed to intermixing between Co and Pt.

Table 5.3: Lattice constants a from Ref. [67], epitaxial misfit $\eta = \frac{a_{sub.} - a_{film}}{a_{film}}$ compared to Pt, elastic compliance constants s_{ij} from [96] and [140], Young's modulus $Y_{111} = \frac{4}{2s_{11} + 2s_{12} + s_{44}}$, and Poisson ratio $\nu_{111} = -Y_{111} \frac{(2s_{11} + 10s_{12} - s_{44})}{12}$ [141] of the substrate Pt and deposited film elements for cubic (111) orientation.

Elements	a Å	η	s_{11}	s_{12} (TPa) ⁻¹	s_{44}	Y (GPa)	ν
fcc Pt	3.92		7.35	-3.08	13.1	185	0.45
fcc Co	3.55	10.4 %	8.81	-3.51	7.83	217	0.46
fcc Ag	4.086	-4.2 %	22.9	-9.8	22.1	82.9	0.52

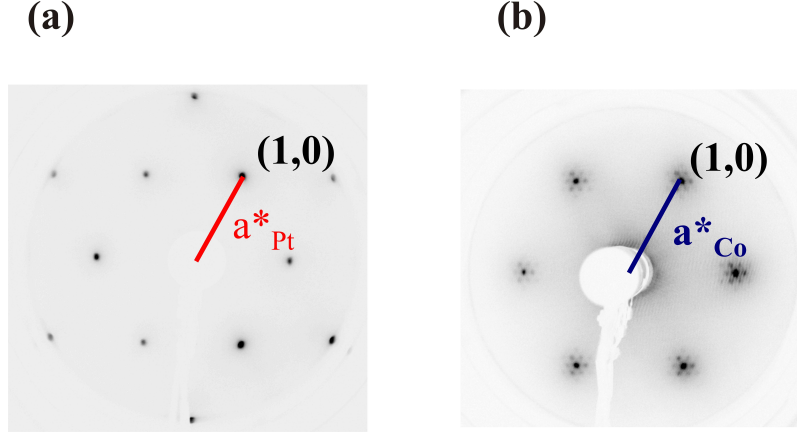


Figure 5.10: (a) Low energy electron diffraction (LEED) image of the clean Pt(111) substrate and (b) of 4 ML Co on Pt(111) at E=144 eV. There are satellites around each integer spot. This indicates a modulation of the Co film structure, where atomic positions of Co are slightly shifted horizontally and vertically around an average Co film structure. a_{Pt}^* and a_{Co}^* are related to the average in-plane structure of the Pt(111) and the Co/Pt(111) systems, respectively.

To further test this speculation, stress is measured during growth of the Co film at different temperatures, as shown in Fig 4.20. We find that the initial stress change of the first 2 MLs gets smaller with increasing temperature. At 370 K it shows even a negative stress change. A strong deviation from a strain-related positive slope of the stress curve to even a negative slope at higher temperature is observed. Our observation of a small Co-induced stress at low thickness questions the assumption of a pseudomorphic growth of the Co film in the first layer. Instead, evidence of a more complex growth mode at the Co-Pt interface is observed, where the incorporation of Co into the Pt surface should be considered [143–145]. A resulting intermixing at the surface leads to a stress change, which cannot be described by lattice mismatch arguments alone. Rather, a subtle interplay between Co-induced surface stress change of the Pt surface and the strain induced by the incorporation of Co into the Pt surface dominates the stress behavior, and it is observed in our measurement.

An intermixed Co-Pt interface has important implications for the magnetic properties of the Co film on Pt(111), and this will be discussed in the next section.

A quantitative analysis of the diffraction patterns reveals a different length of the reciprocal lattice vectors a_{Pt}^* and a_{Co}^* , which corresponds to an average Co film strain of +0.8 %. This strain is calculated by $\epsilon = \frac{a_{Co, film} - a_{Co, bulk}}{a_{Co, bulk}} = \frac{2.53 - 2.51}{2.51} = +0.8 \pm 0.2 \%$, where $a_{Co, film}$ is extracted from LEED image, as demonstrated in Figure 5.10. The strain in the thickness range from 1.2 to 7 ML is significantly lower than the misfit strain of +10.4 %. We apply continuum elasticity to calculate a film stress of +3.3 GPa from the extracted lattice strain. This value is in good agreement with the experimental result of +3.5 GPa.

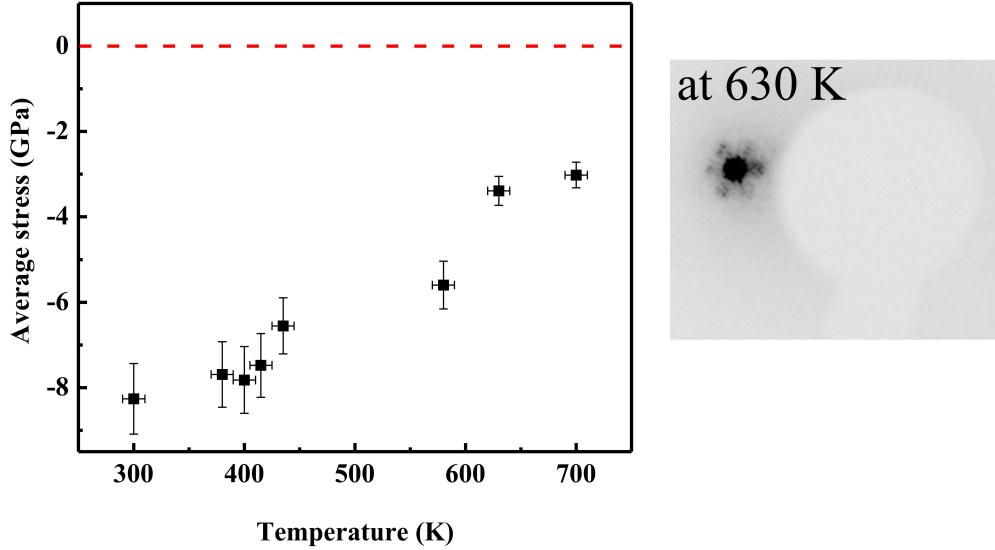


Figure 5.11: Average stress at 3 ML ($\tau_{avg} = \frac{\tau_3}{3 \text{ ML}}$) Ag on Pt(111) deposited at different temperatures. LEED image is taken after Ag deposition at 630 K on Pt(111), at 40 eV the incident electron beam deviate from surface normal with a small angle of 7 degrees. The LEED image shows satellite spots around the (0,0) spot.

The measured stress matches well with the expected stress of 3.3 GPa, and the measured stress is quantitatively ascribed to the average film strain of the Moiré structure.

In case of Ag on Pt(111), the measured stress for deposition at 300 K is compressive, see Fig. 4.22, and it can be described by continuum elasticity up to around 3 ML. The measured stress of -8.9 GPa is close to the calculated stress of -7.13 GPa from lattice mismatch of $\eta = -4.2\%$ between Ag and Pt. This result is in contradiction with the previously reported stress of Ag on Pt(111) [93]. This previous work reported a giant stress in the Ag film. It was speculated that a charge transfer from Ag to Pt, due to the lower electronegativity of Ag compared to Pt, might play an important role. Later an erratum was published [94], but the corrected stress was still much larger than the misfit induced stress. This aspect was addressed also in a theory work [146]. Our results rather indicate the role of epitaxial misfit stress for the initial 3 ML Ag on Pt(111).

Stress measurements during deposition at higher temperatures reveal earlier relaxation of stress and the reduction of the average stress. At 580 K the stress relaxation sets in around 1.5 ML and below this thickness, the stress curve is comparable with the RT stress signal (see Fig. 4.22). This could be due to increased mobility of Ag atoms at HT, leading to a more effective strain relaxation beyond pseudomorphic growth. Previously, a two dimensional alloying of the first layer of Ag with the Pt(111), at around 620 K has been

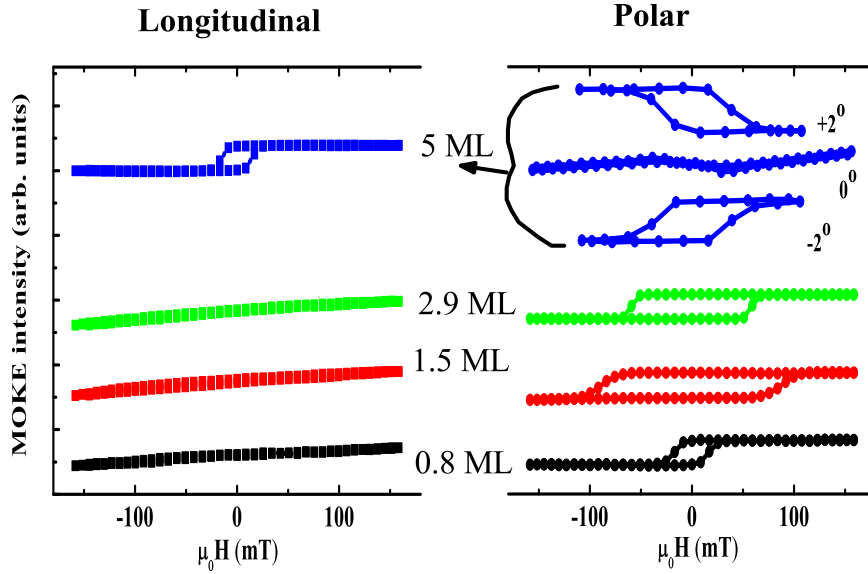


Figure 5.12: The longitudinal (left one) and polar (polar one) Kerr hysteresis loops of Co deposited on Pt(111). All measurements were performed at room temperature.

proposed from STM studies [147].

The average stress at 3 ML, which marks the end of pseudomorphic growth at 300 K, is reduced significantly with increasing temperature, as shown in Figure 5.11. It is almost constant within the error bar, up to around 580 K, but above this temperature the stress is reduced significantly. Around 630 K the satellite spots appear around each integer spot (LEED of (0,0) spot is shown in Fig. 5.11). This indicates misfit dislocation in the film, where stress reduction is visible. Here, the appearance of the satellite spots is the indication of misfit dislocation in the topmost layer [148], which lead to a further reduction of stress.

5.4 Spin reorientation transition (SRT) of Co monolayers on Pt(111)

In this section, the influence of the growth temperature and the effect of a capping layer (Pt) on the spin reorientation transition (SRT) in Co film are discussed. We elucidate the correlation between stress, strain, interface properties and magnetism of Co films on Pt(111).

A re-orientation of the easy axis of magnetization from the out-of-plane to the in-plane directions, a so-called spin reorientation transition (SRT), is observed around 3.5 ML Co on Pt(111) at 300 K. The thickness depended MOKE hys-

teresis loops are shown in Figure 5.12. Our in situ studies of the magnetism of Co monolayers on Pt(111) reveal that the critical thickness for the SRT varies sharply with the Co growth temperature. The Co film deposition at 300 K leads to this transition at 3.5 ML, whereas it is shifted to 5 ML for deposition at 370 K.

Figure 5.13 shows the remanent MOKE intensities of Co/Pt(111) for different Co film thickness. The remanent intensity is extracted from hysteresis loops shown in Figure 5.12. The transition of the easy axis of the magnetization from perpendicular to parallel to the film plane happens between 3 and 4 ML. Similar results have been described in the literature [149], which reported the SRT at 3.5 ML Co. In some papers it is reported that for the film grown at 300 K the SRT occurs in between 4 and 6 ML Co/Pt(111) [150]. This discrepancy between published values of the SRT has not been resolved yet. Our results on T-dependent growth shed some light on possible mechanisms, where interfacial intermixing could be one decisive aspect. It has been reported that Co/Pt(111) can have a strong perpendicular magnetic anisotropy, [151, 152]. The authors have extracted a magnetic anisotropy of 9 meV per atom for Co nanoparticles deposited in Pt(111), which is enormously large compared to any other magnetic material. This was attributed to strong spin-orbit coupling induced by the

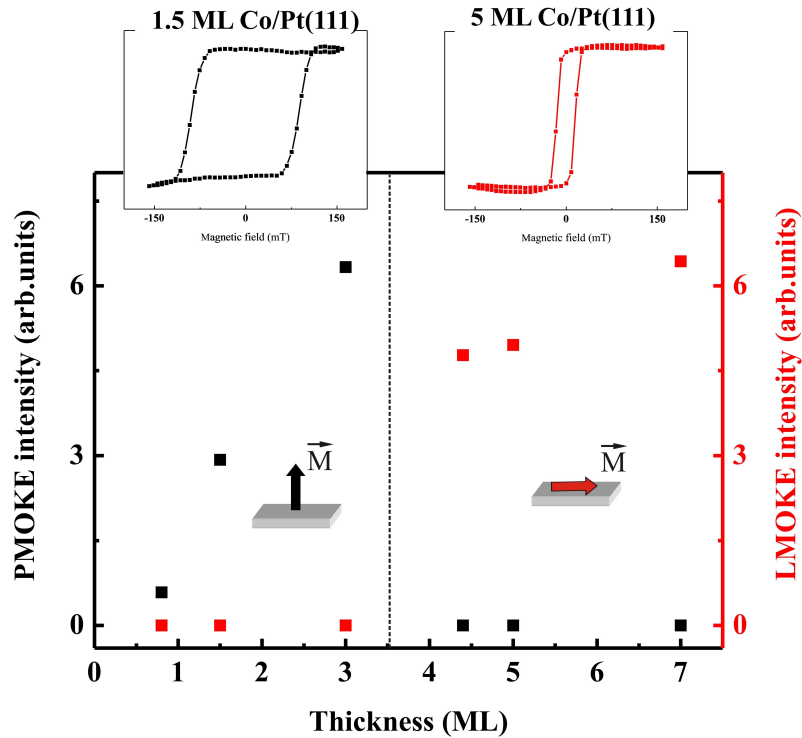


Figure 5.13: Polar (left scale) and Longitudinal (right scale) MOKE Intensities are plotted as a function of Co film thickness. At the thickness of 3.5 ML Co the spin reorientation transition (SRT) from out-of-plane to in-plane occurs.

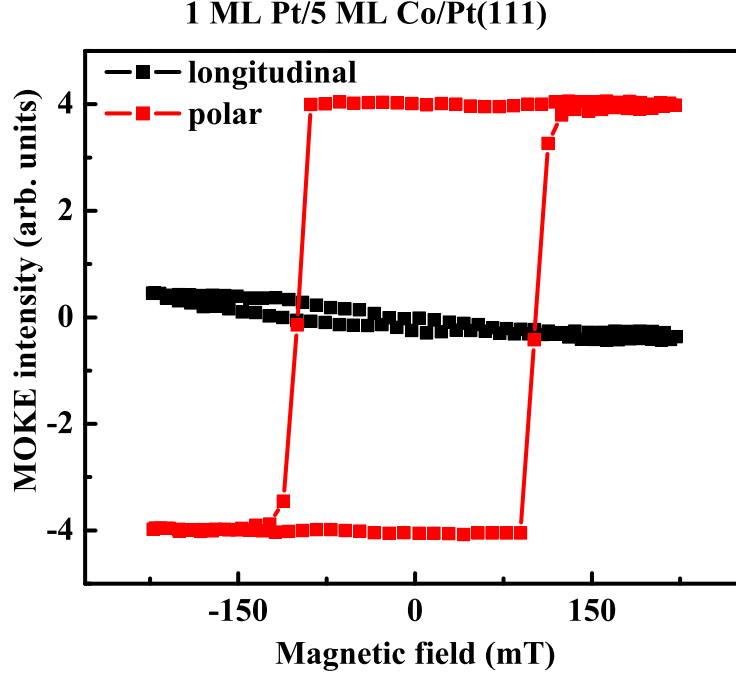


Figure 5.14: Longitudinal (black) and polar (red) MOKE hysteresis loops after capping of 1 ML Pt on top of 5 ML Co/Pt(111), measured at 300 K.

platinum substrate. Our stress measurements at 300 K suggest some intermixing at the Co-Pt interface [153], which gets more pronounced with increasing temperature. The MOKE measurements of Co deposited at 370 K indicates an out-of-plane easy axis even up to 5 ML. This result leads us to speculate that inter-diffusion of Co at the interface favors an out-of-plane easy magnetization direction. This result offers new insight into the role of intermixing at the interface for the peculiar magnetic properties of Co monolayers on Pt(111). Our results propose that an intermixed Co-Pt interface favors out-of-plane magnetization.

It is revealing in this context that the deposition of one monolayer of Pt on top of the 5 ML Co film induces an SRT from in-plane to out-of-plane. This indicates that we can tune the direction of the easy axis of magnetization by changing the Co/vacuum interface. The in-plane and out-of-plane magnetization loops of 1 ML Pt/5 ML Co/Pt(111) are shown in Figure 5.14. No obvious structural changes are observed from our LEED measurements upon deposition of one ML Pt. The measured interlayer distances from LEED I(V) kinematic analysis are $d_{Pt(111),substrate} = 2.26 \pm 0.02 \text{ \AA}$ (bulk Pt(111)=2.26Å), 5 ML Co $d_{Co(111),film} = 2.03 \pm 0.02 \text{ \AA}$ (bulk Co(111)=2.05Å), and for 1 ML Pt on 5 ML Co/Pt(111) $d = 2.03 \pm 0.02 \text{ \AA}$. Thus, the vertical layer spacing remains unaffected by the deposition of a Pt ML. Also, no significant stress was induced upon deposition of Pt on top of 5 ML Co/Pt(111). The interlayer distance of 5 ML Co/Pt(111) is 0.8 % less than the bulk Co. This reconfirms our in-plane extracted strain from LEED patterns. In the literature the effect of capping was reported for Ag on

5 ML Co/Pt(111) [149] and CO adsorption on 4 ML Co/Pt(111) [154], both lead to an SRT of the easy direction of magnetization from parallel to perpendicular to the film plane. Several mechanisms have been proposed, including the strain due to the large lattice mismatch and the hybridization of electron states at the Ag/Co interface. Here, for Pt/Co/Pt(111), we can rule out a structural change and strain-induced stress due to the cap layer Pt. It can be stated that the magnetic anisotropy of the Co film is very sensitive to the local environment. As the Co-vacuum interface favors an in-plane magnetization, any interruption to this interface leads to a drastic change in magnetic anisotropy, favoring an out-of-plane magnetization direction.

Chapter 6

Conclusions and outlook

In this thesis, two transition metal oxides NiO and CoO were successfully grown on Ag(001) and characterized. Fe monolayers were epitaxially grown on top of the oxides and investigated by stress, low energy electron diffraction (LEED), magneto optic Kerr effect (MOKE), and magnetoelastic stress measurements. The film stress during pseudomorphic growth is ascribed to the misfit induced stress, it relaxes as the thickness increases. In the last part of this work Co and Ag on Pt(111) are investigated by stress during deposition and LEED. A spin reorientation transition (SRT) is found in the Co film with increasing thickness by MOKE. The structure of this surface was elucidated by LEED.

The data on NiO on Ag(001) reveal the correlation between stress and structural transitions at surfaces and in atomic layers. Our data suggest that the stress-strain relation in films thicker than 1.5 ML can be well described by linear elasticity. At the interface or below 1.5 ML, stress is different from the expected value based on lattice mismatch. At the NiO-Ag interface, approximately 30 % of a ML of NiO is embedded in the surface, and the corresponding fraction of Ag atoms is expelled, as an SXRD structural analysis proposes [88]. The interface formation is characterized by a tensile surface stress change, which can qualitatively be ascribed to the interaction between Ag and O. Our experimental results indicate pseudomorphic growth of NiO monolayers on Ag(001) from 1.5 to 5 ML. Our combined stress and LEED measurements, identify the formation of misfit dislocations when the NiO film stress relaxes above 5 ML. The CoO-induced stress on Ag(001) is significantly smaller than the calculated misfit stress, however, no structural transition is seen in LEED. In this system, other contributions are responsible for the reduced stress, possibly surface stress changes and film morphology.

The magnetic hysteresis of Fe monolayers on NiO reveals an enlarged coercivity at room temperature, which is ascribed to an exchange coupling between the ferromagnetic Fe film and the AFM NiO layer underneath. The coercivity increases with increasing the thickness of the NiO film, and it decreases with increasing the temperature. For Fe/CoO/Ag(001), the coercivity enhancement appears below room temperature. In both systems, the Fe film has an in-plane easy axis of magnetization. Temperature dependent measurements suggest that

the large coercivity of Fe is due to the antiferromagnetic order of the oxides. In case of Fe/CoO/Ag(001) the coercivity enlargement is maximum already at 10 ML of CoO, whereas, on Fe/NiO/Ag(001) it reaches a maximum at 20 ML. These results suggest that the exchange coupling across the interface is stronger for Fe-CoO as compared to Fe-NiO.

The results presented in this thesis provide new and first insight into the magnetoelastic coupling of Fe films on an antiferromagnetic oxide layer where the role of ferromagnetic/antiferromagnetic interface is critical. A significantly enhanced ME coupling is found which amounts to $B_2 = -19.6 \text{ MJ/m}^3$, almost factors -3 and -10 larger as compared to the bulk value and Fe/Ag(001), respectively. The exact mechanism which drives this difference from the bulk Fe and also from that of Fe films on Ag(001) is still unresolved. From the experiments, it is found that the previously proposed strain and ferromagnetic thickness dependent corrections to B_i are not sufficient to explain B_2 of Fe on NiO/Ag(001). Temperature dependent magnetoelastic coupling measurements for Fe/NiO/Ag(001) are required to further confirm the role of AFM order for the significantly different B_2 . However, this is quite a challenge for the experiment in view of anticipated thermal drift. Successful experiments in this directions have yet to be performed. An alternative approach might be to reduce the NiO film thickness to possibly imitate the T-dependence, at constant temperature measurements at 300 K. The unexpected drastic modification of the magnetoelastic coupling B_2 of Fe when deposited on NiO/Ag(001) as compared to deposition on Ag(001) opens a new effect to modify magnetoelastic effects in addition to lattice strain, which has been discussed in previous work [21] and dissertation [26]. The experiment should be performed also on a differently cut Ag(001) to measure B_1 of Fe/NiO/Ag(001) and for comparison Fe/Ag(001). First experiment at the end of the thesis, point a possibility to modify B_2 making it similar to the value of Fe/Ag(001) by inserting a buffer layer of Ag, for example Fe/Ag/NiO/Ag(001). The role of the Fe-NiO interface, its AFM order in NiO, and T-dependence of B_2 identify further experimentally challenging tasks for future work.

Our stress measurements indicate intermixing at the Co/Pt(111) interface. The intermixed Co-Pt interface has important implications on the magnetic properties of Co deposited on Pt(111). Our *in-situ* MOKE measurements of Co monolayers on Pt(111) reveal that the critical thickness for a re-orientation of the easy magnetization direction of Co from out-of-plane to in-plane is around 3.5 ML at 300 K, and it varies with the Co growth temperature. Co deposition at 370 K shifts this transition to 5 ML. We infer from our MOKE study in connection with the stress analysis that an intermixed Co-Pt interface prefers an out-of-plane easy axis of magnetization. This result offers new insight into the role of intermixing for the peculiar magnetic properties of Co monolayers on Pt. Furthermore, it is found that deposition of 1 ML Pt on top of 5 ML Co/Pt(111) drives a spin reorientation transition back to out-of-plane. This indicates that the Co-vacuum interface favors an in-plane easy axis of magnetization. Any kind of modification of this interface induces an SRT to out-of-plane.

We have seen from our experiments that the stress induced by Ag on Pt(111) can be described by lattice mismatch. The average stress of the film decreases with the temperature at above 580 K, below this temperature it is almost constant. However, no sign of intermixing at the interface is observable from our stress measurements, even the film deposition at higher temperature.

Bibliography

- [1] D. Li, M. Freitag, J. Pearson, Z. Q. Qiu, and S. D. Bader, *Phys. Rev. Lett.* **72**, 3112–3115 (1994).
- [2] O. Heckmann, H. Magnan, P. le Fevre, D. Chandesris, and J. J. Rehr, *Surf. Sci.* **312**, 62–72 (1994).
- [3] S. Müller, B. Schulz, G. Kostka, M. Farle, K. Heinz, and K. Baberschke, *Surf. Sci.* **364**, 235–241 (1996).
- [4] D. Sander, W. Pan, S. Ouazi, J. Kirschner, W. Meyer, M. Krause, S. Müller, L. Hammer, and K. Heinz, *Phys. Rev. Lett.* **93**, 247203 (2004).
- [5] P. Grünberg, *Phys. Today* **54**, 31 (2001).
- [6] J. A. C. Bland and B. Heinrich, Springer, Berlin, 1994.
- [7] W. H. Meiklejohn and C. P. Bean, *Phys. Rev.* **102**, 1413–1414 (1956).
- [8] J. Nogués and I. K. Schuller, *J. Magn. Magn. Mater.* **192**, 203–232 (1999).
- [9] A. Scholl, M. Liberati, E. Arenholz, H. Ohldag, and J. Stöhr, *Phys. Rev. Lett.* **92**, 247201 (2004).
- [10] J. Nogués, C. Leighton, and I. K. Schuller, *Phys. Rev. B* **61**, 1315–1317 (2000).
- [11] J. Nogués, J. Sort, V. Langlais, V. Skumryev, S. Suriñach, J. S. Muñoz, and M. D. Baró, *Phys. Rep.* **422**, 65–117 (2005).
- [12] F. Radu, M. Etzkorn, R. Siebrecht, T. Schmitte, K. Westerholt, and H. Zabel, *Phys. Rev. B* **67**, 134409 (2003).
- [13] M. Finazzi, L. Duò, and F. Ciccacci, *Surf. Sci. Rep.* **64**, 139–167 (2009).
- [14] J. Wu, J. S. Park, W. Kim, E. Arenholz, M. Liberati, A. Scholl, Y. Z. Wu, C. Hwang, and Z. Q. Qiu, *Phys. Rev. Lett.* **104**, 217204 (2010).

-
- [15] W. Kim, E. Jin, J. Wu, J. Park, E. Arenholz, A. Scholl, C. Hwang, and Z. Q. Qiu, *Phys. Rev. B* **81**, 174416 (2010).
- [16] T. C. Schulthess and W. H. Butler, *Phys. Rev. Lett.* **81**, 4516–4519 (1998).
- [17] K. Takano, R. H. Kodama, A. E. Berkowitz, W. Cao, and G. Thomas, *Phys. Rev. Lett.* **79**, 1130–1133 (1997).
- [18] C. Kittel, *Rev. Mod. Phys.* **21**, 541–583 (1949).
- [19] G. Wedler, J. Walz, A. Greuer, and R. Koch, *Phys. Rev. B* **60**, R11313–R11316 (1999).
- [20] G. Wedler, B. Wassermann, and R. Koch, *Phys. Rev. B* **66**, 064415 (2002).
- [21] Z. Tian, D. Sander, and J. Kirschner, *Phys. Rev. B* **79**, 024432 (2009).
- [22] M. Fähnle and M. Komelj, *J. Magn. Magn. Mater.* **220**, 13–17 (2000).
- [23] D. Sander, A. Enders, and J. Kirschner, *J. Magn. Magn. Mater.* **198-199**, 519–521 (1999).
- [24] D. Sander and J. Kirschner, *physica status solidi (b)* **248**, 2389–2397 (2011).
- [25] B. Schulz and K. Baberschke, *Phys. Rev. B* **50**, 13467–13471 (1994).
- [26] Z. Tian, PhD thesis, Martin-Luther-Universität Halle-Wittenberg, 2008.
- [27] M. Farle, *Rep. Prog. Phys.* **61**, 755 (1998).
- [28] D. Sander, *Rep. Prog. Phys.* **62**, 809 (1999).
- [29] D. Sander, *J. Phys. Condens. Matter* **16**, R603 (2004).
- [30] H. Ibach, *Surf. Sci. Rep.* **29**, 193–263 (1997).
- [31] R. C. Cammarata, *Prog. Surf. Sci.* **46**, 1–38 (1994).
- [32] D. Sander and H. Ibach, in *Landolt-Börnstein: Numerical Data and Functional Relationships in Science and Technology*, edited by H. P. Bonzel, volume 42 of *New Series III*, pages 1–49, Springer, Berlin, 2001.
- [33] R. C. Cammarata, K. Sieradzki, and F. Spaepen, *J. Appl. Phys.* **87**, 1227 (2000).

- [34] D. Sander, A. Enders, and J. Kirschner, *Rev. Sci. Instr.* **66**, 4734 (1995).
- [35] D. Sander and H. Ibach, *Phys. Rev. B* **43**, 4263–4267 (1991).
- [36] C. E. Bach, M. Giesen, H. Ibach, and T. L. Einstein, *Phys. Rev. Lett.* **78**, 4225–4228 (1997).
- [37] R. M. Tromp, A. W. Denier van der Gon, and M. C. Reuter, *Phys. Rev. Lett.* **68**, 2313–2316 (1992).
- [38] J. Fritz, M. K. Baller, H. P. Lang, T. Strunz, E. Meyer, H. J. Güntherodt, E. Delamarche, C. Gerber, and J. K. Gimzewski, *Langmuir* **16**, 9694–9696 (2000).
- [39] R. D. Meade and D. Vanderbilt, *Phys. Rev. Lett.* **63**, 1404–1407 (1989).
- [40] R. J. Needs, *Phys. Rev. Lett.* **58**, 53–56 (1987).
- [41] P. J. Feibelman, *Phys. Rev. B* **56**, 2175–2182 (1997).
- [42] D. Vanderbilt, *Phys. Rev. Lett.* **59**, 1456–1459 (1987).
- [43] R. Popescu, H. L. Meyerheim, D. Sander, J. Kirschner, P. Steadman, O. Robach, and S. Ferrer, *Phys. Rev. B* **68**, 155421 (2003).
- [44] J. W. Matthews and A. E. Blakeslee, *Journal of Crystal Growth* **27**, 118–125 (1974).
- [45] J. H. van der Merwe, E. Bauer, D. L. Tönsing, and P. M. Stoop, *Phys. Rev. B* **49**, 2127–2136 (1994).
- [46] J. Wollschläger, D. Erdös, and K. M. Schröder, *Surf. Sci.* **402-404**, 272–276 (1998).
- [47] J. Wollschläger, D. Erdös, H. Goldbach, R. Höpken, and K. M. Schröder, *Thin Solid Films* **400**, 1–8 (2001).
- [48] M. B. Stearns, in *Landolt-Börnstein: Numerical Data and Functional Relationships in Science and Technology*, volume 19a of *Group III*, Springer, Berlin, 1986.
- [49] B. Heinrich, Z. Celinski, J. F. Cochran, A. S. Arrott, and K. Myrtle, *J. Appl. Phys.* **70**, 5769 (1991).
- [50] R. Skomski, *J. Phys. Condens. Matter* **15**, R841 (2003).
- [51] S. D. Bader, *Surf. Sci.* **500**, 172–188 (2002).

-
- [52] R. Wu, L. Chen, and A. J. Freeman, *J. Appl. Phys.* **81**, 4417–4418 (1997).
- [53] M. Fähnle, M. Komelj, R. Q. Wu, and G. Y. Guo, *Phys. Rev. B* **65**, 144436 (2002).
- [54] T. Burkert, O. Eriksson, P. James, S. I. Simak, B. Johansson, and L. Nordström, *Phys. Rev. B* **69**, 104426 (2004).
- [55] D. Sander, H. L. Meyerheim, S. Ferrer, and J. Kirschner, *Advances in Solid State Physics*; Springer-Verlag, Berlin, Germany **43**, 547–561 (2003).
- [56] D. Sander and J. Kirschner, *Appl. Phys. A* **87**, 419–425 (2007).
- [57] T. Gutjahr-Löser, D. Sander, and J. Kirschner, *J. Appl. Phys.* **87**, 5920 (2000).
- [58] T. Gutjahr-Löser, D. Sander, and J. Kirschner, *J. Magn. Magn. Mater.* **220**, 1–7 (2000).
- [59] W. Wulfhekel, T. Gutjahr-Löser, F. Zavaliche, D. Sander, and J. Kirschner, *Phys. Rev. B* **64**, 144422 (2001).
- [60] A. P. Malozemoff, *J. Appl. Phys.* **63**, 3874–3879 (1988).
- [61] D. Mauri, H. C. Siegmann, P. S. Bagus, and E. Kay, *J. Appl. Phys.* **62**, 3047 (1987).
- [62] N. C. Koon, *Phys. Rev. Lett.* **78**, 4865–4868 (1997).
- [63] T. C. Schulthess and W. H. Butler, *J. Appl. Phys.* **85**, 5510 (1999).
- [64] A. Enders, PhD thesis, Martin-Luther-Universität Halle-Wittenberg, 1999.
- [65] C. Davisson and L. H. Germer, *Phys. Rev.* **30**, 705–740 (1927).
- [66] C. Kittel, John Wiley & Sons, Inc, 8th edition, 2005.
- [67] J. D. H. Donnay and H. M. Ondik, National Bureau of Standards, Gaithersburg, MD, 1973.
- [68] *SPECS Surface Nano Analysis GmbH*, Voltastrasse 5, Berlin, Germany.
- [69] M. Zharnikov, A. Dittschar, W. Kuch, C. M. Schneider, and J. Kirschner, *J. Magn. Magn. Mater.* **174**, 40–56 (1997).

- [70] K. Heinz, Rep. Prog. Phys. **58**, 637 (1995).
- [71] OMICRON NANO TECHNOLOGY GMBH., D-6204 Taunusstein 4, Germany, *OMICRON NANO TECHNOLOGY GMBH, D-6204 Taunusstein 4, Germany*, 1990.
- [72] R. E. Martinez, W. M. Augustyniak, and J. A. Golovchenko, Phys. Rev. Lett. **64**, 1035–1038 (1990).
- [73] R. Mahesh, D. Sander, S. M. Zharkov, and J. Kirschner, Phys. Rev. B **68**, 045416 (2003).
- [74] W. Pan, PhD thesis, National Taiwan University, 2003.
- [75] D. Sander, S. Ouazi, A. Enders, T. Gutjahr-Löser, V. S. Stepanyuk, D. I. Bazhanov, and J. Kirschner, J. Phys. Condens. Matter **14**, 4165 (2002).
- [76] K. Dahmen, H. Ibach, and D. Sander, J. Magn. Magn. Mater. **231**, 74–84 (2001).
- [77] G. G. Stoney, Proc. R. Soc. London, Ser. A **82**, 172 (1909).
- [78] J. F. Nye, Oxford University Press, 1985.
- [79] Z. Q. Qiu and S. D. Bader, J. Magn. Magn. Mater. **200**, 664–678 (1999).
- [80] Z. Q. Qiu and S. D. Bader, Rev. Sci. Inst. **71**, 1243 (2000).
- [81] E. R. Moog, C. Liu, S. D. Bader, and J. Zak, Phys. Rev. B **39**, 6949–6956 (1989).
- [82] P. N. Argyres, Phys. Rev. **97**, 334–345 (1955).
- [83] D. Sander, R. Skomski, A. Enders, C. Schmidthals, D. Reuter, and J. Kirschner, J. Phys. D Appl. Phys. **31**, 663 (1998).
- [84] Schäfter + Kirchoff GmbH., Kieler Strasse 212 D-22525 Hamburg, Germany, *Schäfter + Kirchoff GmbH - Optics, Metrology and Photonics*.
- [85] K. Marre and H. Neddermeyer, Surf. Sci. **287-288**, 995–999 (1993).
- [86] Z. Tian, D. Sander, N. N. Negulyaev, V. S. Stepanyuk, and J. Kirschner, Phys. Rev. B **81**, 113407 (2010).
- [87] I. Sebastian, T. Bertrams, K. Meinel, and H. Neddermeyer, Faraday Discuss **114**, 129–140 (1999).

- [88] A. Dhaka, D. Sander, H. L. Meyerheim, K. Mohseni, E. Soyka, J. Kirschner, W. A. Adeagbo, G. Fischer, A. Ernst, and W. Hergert, Stress and structure at the NiO/Ag(001) interface, *Phys. Rev. B* **84**, 195441 (Nov 2011).
- [89] W. L. Roth, *Phys. Rev.* **110**, 1333–1341 (1958).
- [90] D. Sander, Z. Tian, and J. Kirschner, *Sensors* **8**(7), 4466–4486 (2008).
- [91] R. Koch, M. Weber, K. Thürmer, and K. H. Rieder, *J. Magn. Magn. Mater.* **159**, L11–L16 (1996).
- [92] D. Sander, Z. Tian, A. Dhaka, S. Ouazi, and H. Brune, in *Max-Planck-Institut für Mikrostrukturphysik Halle: Annual Report*, pages 14–15, 2009.
- [93] A. Grossmann, W. Erley, J. B. Hannon, and H. Ibach, *Phys. Rev. Lett.* **77**, 127–130 (1996).
- [94] A. Grossmann, W. Erley, J. B. Hannon, and H. Ibach, *Phys. Rev. Lett.* **78**, 3587 (1997).
- [95] in *Landolt-Börnstein, Numerical Data, New series*, volume 11 of *Group III*, page 28.
- [96] R. Bechmann, R. F. S. Hearmon, and S. K. Kurtz, in *Landolt-Börnstein: Numerical Data and Functional Relationships in Science and Technology*, volume 2 of *Group III*, page 36, Springer, Berlin, 1969.
- [97] M. Caffio, B. Cortigiani, G. Roviola, A. Atrei, C. Giovanardi, A. di Bona, and S. Valeri, *Surf. Sci.* **531**, 368–374 (2003).
- [98] T. Bertrams and H. Neddermeyer, *J. Vac. Sci. Technol. B* **14**, 1141–1144 (1996).
- [99] S. Großer, C. Hagendorf, H. Neddermeyer, and W. Widdra, *Surface and Interface Analysis* **40**, 1741–1746 (2008).
- [100] D. Sander, Z. Tian, and J. Kirschner, *J. Phys. Condens. Matter* **21**, 134015 (2009).
- [101] M. J. Harrison, D. P. Woodruff, J. Robinson, D. Sander, W. Pan, and J. Kirschner, *Phys. Rev. B* **74**, 165402 (2006).
- [102] C. Lamberti, E. Groppo, C. Prestipino, S. Casassa, A. M. Ferrari, C. Pisani, C. Giovanardi, P. Luches, S. Valeri, and F. Boscherini, *Phys. Rev. Lett.* **91**, 046101 (2003).

-
- [103] E. Groppo, C. Prestipino, C. Lamberti, P. Luches, C. Giovanardi, and F. Boscherini, *J. Phys. Chem.* **107**, 4597 (2003).
- [104] M. Dynna, J. L. Vassent, A. Marty, and B. Gilles, *J. Appl. Phys.* **80**, 2650–2657 (1996).
- [105] R. Shantyr, PhD thesis, Martin-Luther-Universität Halle-Wittenberg, 2004.
- [106] A. Stierle, I. Costina, S. Kumaragurubaran, and H. Dosch, *The Journal of Physical Chemistry C* **111**, 10998–11002 (2007).
- [107] I. Costina, M. Schmid, H. Schiechl, M. Gajdoš, A. Stierle, S. Kumaragurubaran, J. Hafner, H. Dosch, and P. Varga, *Surf. Sci.* **600**, 617–624 (2006).
- [108] I. Sebastian and H. Neddermeyer, *Surf. Sci.* **454**, 771–777 (2000).
- [109] D. Sander, U. Linke, and H. Ibach, *Surf. Sci.* **272**, 318–325 (1992).
- [110] K. M. Schindler, J. Wang, A. Chassé, H. Neddermeyer, and W. Widdra, *Surf. Sci.* **603**, 2658–2663 (2009).
- [111] P. Luches, S. Benedetti, A. di Bona, and S. Valeri, *Phys. Rev. B* **81**, 054431 (2010).
- [112] T. Yamada, *Journal of the Physical Society of Japan* **21**, 664–671 (1966).
- [113] D. Spanke, V. Solinus, D. Knabben, F. U. Hillebrecht, F. Ciccacci, L. Gregoratti, and M. Marsi, *Phys. Rev. B* **58**, 5201–5204 (1998).
- [114] S. I. Csiszar, M. W. Haverkort, Z. Hu, A. Tanaka, H. H. Hsieh, H. J. Lin, C. T. Chen, T. Hibma, and L. H. Tjeng, *Phys. Rev. Lett.* **95**, 187205 (2005).
- [115] H. Ohldag, A. Scholl, F. Nolting, S. Anders, F. U. Hillebrecht, and J. Stöhr, *Phys. Rev. Lett.* **86**, 2878–2881 (2001).
- [116] M. Stampanoni, A. Vaterlaus, M. Aeschlimann, and F. Meier, *Phys. Rev. Lett.* **59**, 2483–2485 (1987).
- [117] X. G. Zheng, C. N. Xu, K. Nishikubo, K. Nishiyama, W. Higemoto, W. J. Moon, E. Tanaka, and E. S. Otabe, *Phys. Rev. B* **72**, 014464 (2005).
- [118] D. Alders, L. H. Tjeng, F. C. Voogt, T. Hibma, G. A. Sawatzky, C. T. Chen, J. Vogel, M. Sacchi, and S. Iacobucci, *Phys. Rev. B* **57**, 11623–11631 (1998).

- [119] D. Sander, R. Skomski, C. Schmidhals, A. Enders, and J. Kirschner, *Phys. Rev. Lett.* **77**, 2566–2569 (1996).
- [120] F. Offi, W. Kuch, and J. Kirschner, *Phys. Rev. B* **66**, 064419 (2002).
- [121] K. Lenz, S. Zander, and W. Kuch, *Phys. Rev. Lett.* **98**, 237201 (2007).
- [122] R. C. O’Handley, JOHN WILEY & SONS, INC., New York,, 2000.
- [123] R. Skomski and J. M. D. Coey, *Phys. Rev. B* **48**, 15812–15816 (1993).
- [124] W. H. Meiklejohn and C. P. Bean, *Phys. Rev.* **105**, 904–913 (1957).
- [125] H. Ohldag, A. Scholl, F. Nolting, E. Arenholz, S. Maat, A. T. Young, M. Carey, and J. Stöhr, *Phys. Rev. Lett.* **91**, 017203 (2003).
- [126] H. Ohldag, H. Shi, E. Arenholz, J. Stöhr, and D. Lederman, *Phys. Rev. Lett.* **96**, 027203 (2006).
- [127] S. Roy, M. R. Fitzsimmons, S. Park, M. Dorn, O. Petravic, I. V. Roshchin, Z.-P. Li, X. Battle, R. Morales, A. Misra, X. Zhang, K. Chesnel, J. B. Kortright, S. K. Sinha, and I. K. Schuller, *Phys. Rev. Lett.* **95**, 047201 (2005).
- [128] F. Radu, A. Nefedov, J. Grabis, G. Nowak, A. Bergmann, and H. Zabel, *J. Magn. Magn. Mater.* **300**, 206–210 (2006).
- [129] R. Abrudan, J. Miguel, M. Bernien, C. Tieg, M. Piantek, J. Kirschner, and W. Kuch, *Phys. Rev. B* **77**, 014411 (2008).
- [130] D.-H. Han, J.-G. Zhu, J. H. Judy, and J. M. Sivertsen, *J. Appl. Phys* **81**, 4519–4521 (1997).
- [131] M. Weber, R. Koch, and K. H. Rieder, *Phys. Rev. Lett.* **73**, 1166–1169 (1994).
- [132] S. W. Sun and R. C. O’Handley, *Phys. Rev. Lett.* **66**, 2798–2801 (1991).
- [133] L. Z. Mezey and J. Giber, *Japanese Journal of Applied Physics* **21**, 1569–1571 (1982).
- [134] S. H. Overbury, P. A. Bertrand, and G. A. Somorjai, *Chemical Reviews* **75**, 547–560 (1975).
- [135] O. Song, C. A. Ballentine, and R. C. O’Handley, *Appl. Phys. Lett.* **64**, 2593 (1994).

- [136] G. Bochi, O. Song, and R. C. O’Handley, *Phys. Rev. B* **50**, 2043–2046 (1994).
- [137] Y. K. Kim and T. J. Silva, *Appl. Phys. Lett.* **68**, 2885 (1996).
- [138] P. Grütter and U. T. Dürig, *Phys. Rev. B* **49**, 2021–2029 (1994).
- [139] E. Lundgren, B. Stanka, M. Schmid, and P. Varga, *Phys. Rev. B* **62**, 2843–2851 (2000).
- [140] A. S. Bhalla, W. R. Cook, R. F. S. Hearmon, J. Jerphagon, S. K. Kurtz, S. T. Liu, D. F. Nelson, and J. L. Oudar, in *Landolt-Börnstein: Numerical Data and Functional Relationships in Science and Technology*, volume 18 of *Group III*, page 140, Springer, Tokyo, 1984.
- [141] W. A. Brantley, *J. Appl. Phys.* **44**, 534–535 (1973).
- [142] D. Sander, A. Enders, and J. Kirschner, *Europhys. Lett.* **45**, 208–214 (1999).
- [143] J. S. Tsay and C. S. Shern, *J. Appl. Phys.* **80**, 3777 (1996).
- [144] E. Lundgren, G. Leonardelli, M. Schmid, and P. Varga, *Surf. Sci.* **498**, 257–265 (2002).
- [145] S. Ferrer, J. Alvarez, E. Lundgren, X. Torrelles, P. Fajardo, and F. Boscherini, *Phys. Rev. B* **56**, 9848–9857 (1997).
- [146] S. Narasimhan, *Phys. Rev. B* **69**, 045425 (2004).
- [147] H. Röder, R. Schuster, H. Brune, and K. Kern, *Phys. Rev. Lett.* **71**, 2086–2089 (1993).
- [148] H. Brune, K. Bromann, H. Röder, K. Kern, J. Jacobsen, P. Stoltze, K. Jacobsen, and J. No/rskov, *Phys. Rev. B* **52**, R14380–R14383 (1995).
- [149] F. C. Chen, Y. E. Wu, C. W. Su, and C. S. Shern, *Phys. Rev. B* **66**, 184417 (2002).
- [150] C. Quirós, S. M. Valvidares, O. Robach, and S. Ferrer, *J. Phys. Condens. Matter* **17**, 5551 (2005).
- [151] P. Gambardella, S. Rusponi, M. Veronese, S. S. Dhesi, C. Grazioli, A. Dallmeyer, I. Cabria, R. Zeller, P. H. Dederichs, K. Kern, C. Carbone, and H. Brune, *Science* **300**, 1130–1133 (2003).

-
- [152] G. Moulas, A. Lehnert, S. Rusponi, J. Zabloudil, C. Etz, S. Ouazi, M. Etzkorn, P. Bencok, P. Gambardella, P. Weinberger, and H. Brune, *Phys. Rev. B* **78**, 214424 (2008).
- [153] C. Boeglin, B. Carrière, J. P. Deville, F. Scheurer, C. Guillot, and N. Barrett, *Phys. Rev. B* **45**, 3834–3837 (1992).
- [154] O. Robach, C. Quiros, P. Steadman, K. F. Peters, E. Lundgren, J. Alvarez, H. Isern, and S. Ferrer, *Phys. Rev. B* **65**, 054423 (2002).

Acknowledgement

First, I would like to acknowledge Prof. Dr. Jürgen Kirschner for giving me the opportunity to pursue my Ph. D. in his department at the Max Planck Institute of Microstructure Physics. His stimulating scientific discussions and constant advice considerably contributed to the completion of this work.

I would like to acknowledge PD Dr. Dirk Sander who has provided me guidance almost on a daily basis. I am immensely thankful to him for all the fruitful discussions, encouragement and intellectual support throughout this course, and being such a wonderful and friendly person. His smiley face always create a positive atmosphere in the lab, and made my mind to step ahead in every difficult situation.

I am thankful to Prof. Dr. Wolf Widdra and his student Mr. Sebastian Polzin for the helpful discussions on preparation of oxides and showing their laboratory. I thank PD Dr. Holger Meyerheim, PD Dr. Arthur Ernst, Dr. W. A. Adeagbo and Dr. K. Mohseni for the helpful discussions.

I would like to thank Dr. Zhen Tian and Dr. Safia Ouazi for teaching me to handle the system and bothering my stupid questions. I would like to thank Mr. Jörg Premper and Dr. Sebastien Wedekind for helping to resolve computer related problems whenever I had encountered during this work. I am thankful of Ms. Nicole Kurowsky and Mr. Benjamin Bergmann for technical assistance. I also enjoyed chit-chatting with them. In addition, I would like to thank our visitor Asst. Prof. Wei Pan from Taiwan for experimental support during writing of my thesis and inspiring discussions.

I specially thank to Ms. Heike Menge, for producing very thin substrates and helping to provide chemically cleaned crucibles.

I would like to thank the staff of the Mechanical and Electronic workshops for their technical support and the administrative staff for their help and cooperation (especially Mr. Bernd Rau, Mr. Michael Oppelt, Ms. Karin Pohlink and Ms. Birgit Frankenstein).

I would like to acknowledge the financial support by Sonderforschungsbereich (SFB) 762 for my doctoral work.

Last but not least, I acknowledge my family back home in India for their love and support. My heartiest thank goes to my husband Rajendra for his immense love and patience. In fact, it is because of his constant encouragement, moral support and confidence in me that I am able to accomplish this work.

Erklärung an Eides statt

Hiermit erkläre ich, dass ich die vorliegende Arbeit selbstständig und ohne fremde Hilfe verfasst, andere als die von mir angegebenen Quellen und Hilfsmittel nicht benutzt und die den benutzten Werken wörtlich oder inhaltlich entnommenen Stellen als solche kenntlich gemacht habe.

Eine Anmeldung der Promotionsabsicht habe ich an keiner anderen Fakultät einer Universität oder Hochschule beantragt.

Anita Dhaka
Halle (Saale), Sept. 2011

Curriculum Vitae

Personal details:

Name : Anita Dhaka
Date of Birth : 1st January 1985
Sex : Female
Place of Birth : Balwantpura, Rajasthan, India.
Nationality : Indian
Marital Status : Married
Present Address : Ernst-Grube-Str. 32, D-06120 Halle (Saale), Germany.
emai ID : dhaka@mpi-halle.mpg.de,dhaka.anita@gmail.com

Education:

Oct. 2008 - present : Doctoral Fellow at Max Planck Institute of Microstructure Physics,
& Martin Luther University, Weinberg 2, D-06120, Halle, Germany.

2007 - 2008 : Project student at UGC-DAE Consortium for Scientific Research,
University Campus, Khandwa Road, Indore, Madhya Pradesh, India.

2006 - 2007 : Bachelors of Education (two semester program),
Department of Education,
Devi Ahilya Vishwavidyalaya, Indore, Madhya Pradesh, India.

2004 - 2006 : Masters of Science in Physics (four semester program),
Department of Physics,
Devi Ahilya Vishwavidyalaya, Indore, Madhya Pradesh, India.

2001 - 2004 : Bachelors of Science (Physics, Mathematics, and Chemistry),
Vikarm University, Ujjain, Madhya Pradesh, India.

Publication:

1. A. Dhaka, D. Sander, H. L. Meyerheim, K. Mohseni, E. Soyka, J. Kirschner, W. A. Adeagbo, G. Fischer, A. Ernst, and W. Hergert, "Stress and structure at the NiO/Ag(001) interface", Phys. Rev. B **84**, 195441 (2011).

Conference & Workshop Presentations:

1. NiO thickness and temperature dependent coercivity of Fe layers grown on NiO/Ag(100)

Anita Dhaka, Dirk Sander and Jürgen Kirschner

Verhandlungen der Sektion Kondensierte Materie der Deutschen Physikalischen Gesellschaft, Dresden, Germany

March 13-18, 2011, Talk

2. Stress induced by NiO monolayers on Ag (100)

Anita Dhaka, Dirk Sander and Jürgen Kirschner

Verhandlungen der Sektion Kondensierte Materie der Deutschen Physikalischen Gesellschaft, Dresden, Germany

March 13-18, 2011, Talk

3. Correlations between stress and magnetism of Co/Pt(111)

Anita Dhaka, Safia Ouazi, Zhen Tian, Dirk Sander and Jürgen Kirschner

Seeheim Conference on Magnetism, Frankfurt, Germany

March 28th-April 1st 2010, Talk

4. Correlation between stress, intermixing and magnetic anisotropy of Pt/Co/Pt(111) monolayers

Anita Dhaka, Safia Ouazi, Zhen Tian, Dirk Sander and Jürgen Kirschner

Frühjahrstagung der Sektion Kondensierte Materie der Deutschen Physikalischen Gesellschaft, Regensburg, Germany

March 21-26, 2010, Talk

5. Correlation between stress and magnetism on Co/Pt(111)

Anita Dhaka, Safia Ouazi, Zhen Tian, Dirk Sander and Jürgen Kirschner

SFB 762 International Workshop "Functionality of Oxide Interfaces and Multiferroic Materials", Irsee, Germany

March 1-5, 2010, Poster

6. Misfit stress and magnetism in Co monolayers on Pt(111)

Anita Dhaka, Safia Ouazi, Zhen Tian, Dirk Sander and Jürgen Kirschner

2nd PhD Workshop of SFB 762 Magnetic properties of oxidic and multiferroic systems, Leucorea, Lutherstadt Wittenberg, Germany

September 10-11, 2009, Poster